DISSERTATION

OPTIMIZING THE ENERGY MEASUREMENT OF THE ATLAS ELECTROMAGNETIC CALORIMETER

ausgeführt zum Zwecke der Erlangung des akademischen Grades eines Doktors der technischen Wissenschaften unter Leitung von

Ao. Univ. Prof. Dr. Dipl. Ing. Christian Fabjan

E141
Atominstitut der österreichischen Universitäten

eingereicht an der Technischen Universität Wien
Fakultät für Physik

von

Dipl. Ing. Walter Lampl
Matrikelnummer 9425217
250, rue Massonnex
F-01710 Thoiry

Wien, am 20. Dezember 2005

Kurzfassung

Die Europäsche Organisation für Teilchenphysik (CERN) in Genf baut momentan einen neuen Hadron-Speicherring, den LHC. LHC ist wesentlich leistungsfähiger als alle bisher gebauten Beschleuniger und ermöglicht es dadurch Physikprozesse zu untersuchen, die bisher experimentell nicht zugänglich waren. Eines der Experimente, das die Möglichkeiten, die LHC bietet, ausschöpfen wird, ist ATLAS. Ein wesentlicher Bestandteil eines Universal-Detektors wie ATLAS ist das elektromagnetische Kalorimeter, das die Energie von Elektronen und Photonen misst. Für ATLAS wurde ein 'Sampling'-Kalorimeter mit Blei-Absorbern und flüssigem Argon als aktives Material gewählt. Eine Besonderheit des ATLAS EM Kalorimeters ist die Akkordeon-Geometrie der Absorber.

Im Sommer 2004 hat die ATLAS Kollaboration ein ausführliches Testprogramm in einem Teilchenstrahl am CERN durchgeführt, um die Leistungsfähigkeit der einzelnen Subdetektoren sowie des Gesamtsystems zu testen. Bei diesem Strahl-Test wurden Detektormodule mit einem Teilchenstrahl bekannter Energie beschossen. Beim Strahl-Test 2004 wurden zum ersten Mal Module aller ATLAS-Subdetektoren gemeinsam betrieben. Vor diesem Test haben viele entscheidende Software-Komponenten, die zum gemeinsamen Betrieb notwendig sind, gefehlt. Im Rahmen der vorliegenden Doktorarbeit wurde an der Vorbereitung der Rekonstruktions-Software für das EM-Kalorimeter gearbeitet. Die hinzugefügten Komponenten sind jetzt Teil der ATLAS Rekonstruktions-Software und werden auch im regulären Betrieb des ATLAS Detektors eingesetzt werden.

Der Hauptteil dieser Arbeit befasst sich mit der Optimierung der Elektronenenergiemessung mit dem ATLAS EM Kalorimeter. Nachdem die vorgeschlagene Methode der Energierekonstruktion auf Monte-Carlo Simulationen basiert, war es notwendig, die Simulation anhand der Daten zu validieren. Es wird gezeigt, daß Simulation und Daten auf etwa 1% übereinstimmen.

Mit Hilfe der Simulation wurden intensive Studien der Schauerentwicklung im aktiven und inaktiven Material des Kalorimeters durchgeführt. Es wurde eine Methode entwickelt, um den Energieverlust im inaktiven Material vor dem Kalorimeter zu kompensieren. Diese Methode erreicht eine sehr gute Linearität von 0.5% zwischen 20 GeV und 250 GeV und gleichzeitig eine exzellente Auflösung ('Sampling Term' $\sim 11\%/\sqrt{E}$) auch mit zusätzlichem inaktiven Material vor dem Kalorimeter. Dies ist besonders wichtig, weil sich in ATLAS eine beträchtliche Menge Material vor dem Kalorimeter befindet (Kryostat, Solenoidspule).

Um die diskutierte Methode zu entwickeln und zu testen, wurden Daten verwendet, die

während der Strahl-Tests im Sommer 2002 und 2004 genommen wurden. Dabei wurde die Energie des Teilchenstrahls systematisch variiert. Im Sommer 2004 wurden zusätzlich auch noch Aluminiumplatten verschiedener Dicke vor dem Kalorimeter positioniert.

Es wurde gezeigt, dass das ATLAS EM Kalorimeter mit der vorgeschlagene Methode der Energierekonstruktion die gestellten Anforderungen erfüllen wird, auch wenn sich Material äquivalent zu drei Strahlungslängen vor dem Kalorimeter befindet.

Abstract

At the European Organization for Particle Physics (CERN) in Geneva a new hadron collider, the LHC, is currently under construction. This collider is designed to probe fundamental physics at an energy scale well beyond the limits of current research facilities. One of the experiments that is built to exploit the opportunities offered by LHC is ATLAS. An essential element of a general-purpose detector like ATLAS is the electromagnetic calorimeter that will measure the energy of photons and electrons with very high precision. A sampling calorimeter with lead absorbers and liquid argon as active medium was chosen. The absorbers have an accordion-geometry.

During summer 2004, the ATLAS collaboration carried out an extensive beam test program at one of CERN's beam lines to verify the performance of the individual subdetectors as well as of the combined system. During such a beam test, modules of a detector are exposed to a beam of particles with known energy. This was the first time that modules of all sub-systems of ATLAS were operated together. Before the beam test, many essential software components needed for a combined operation were missing. It was part of the work for this PhD-Thesis to get the EM Calorimeter reconstruction software to the operational level, ready for in the combined beam test. The components that have been added are now part of the reconstruction framework and will be used also for the regular operation of the ATLAS detector.

The main part of this thesis deals with the optimization of the electron energy measurement with the ATLAS EM calorimeter. Since Monte-Carlo studies were the basis of the presented calibration method, it was important to validate the simulation by comparing it to beam test data. It has been shown that the data-simulation agreement is at the level of about 1%.

Using Monte-Carlo simulations, extensive studies of the development of the electromagnetic shower in the active and passive zones of the calorimeter have been performed, which lead to a method to correct for energy losses in inactive material. This method achieves a very good linearity of 0.5% between 20 GeV and 250 GeV and at the same time an excellent resolution (sampling term $\sim 11\%/\sqrt{E}$) even in the presence of inactive material in front of the calorimeter. This is important since in ATLAS there is a significant amount of matter (cryostat, solenoid coil) in front of the calorimeter.

To develop and test the method, data from a linearity-scan taken during the 2002 EM-Calorimeter standalone beam test was used as well as data from a material scan that was

carried out during the 2004 combined beam test. During the material-scan not only the beam energy was varied systematically, but also aluminum blocks of various thicknesses were put into the beam in front of the calorimeter to simulated different upstream material at different impact points.

It has been demostrated that using this proposed method of energy reconstruction the ATLAS EM calorimeter will perform according to the requirements with ATLAS-like upstream material of $\sim$3 radiation lengths.

Acknowledgments

To carry out this thesis, I spent the last two and a half years at CERN in Geneva. The company of many nice and interesting people made this time very fruitful and enjoyable for me. First of all I have to thank Prof. Chris Fabjan for the great opportunity to work at CERN and the continuous support during my stay.

Special thanks go to Martin Aleksa who introduced me to the complexity of calorimetry in general and the ATLAS electromagnetic calorimeter in particular. He supported my work literally on a day-by-day basis. Although he has a very tight schedule, he always found the time to have a coffee together and talk about many things, work-related as well as others.

A partner for many fruitful discussions was Tancredi Carli. Without him I would have achieved only a small fraction of what I have. Especially towards the end of my work when I tried to get this thesis into a decent shape his comments were more than useful!

For proof-reading this thesis, I would like to thank Martin, Tancredi and Karina.

An important part of my thesis was the work on the combined beam test. Under the guidance of Martin and Isabelle a rather small group of people kept the liquid argon beam test setup running. Despite the stress and the night-shifts, it was a pleasure to work with you: Sandrine, Remi, Marco, Marcello, Henric, Damien!

Many people deserve recongition for their help with Atlas software, in particular during the first months of my thesis work when I was an absolute beginner in this field. Srini, Hong, Rob, Peter, thanks a lot!

For their help with the beam test simulation, I have to thank Manuel, Guillaume and Stathes. Nicolas did a lot of work to understand the exact beam energy in the beam test. This was very useful for me, thanks a lot!

At the CERN restaurant as well as on the ski-slopes and in the pubs of Geneva, I enjoyed nice company of many other young Austrians (and a few non-Austrians).

Heart felt thanks must go to my neighbors Veronique and Pascal, the expert for everything concerning Geneva and the Pays-de-Gex. Living in a foreign country, it was very helpful to have somebody how knows how to deal with local authorities, insurance companies, etc...

An important role in my life plays of course my girlfriend Daniela. I know that it was a difficult decision to give up her job in Vienna to join me here in Geneva. I am deeply grateful for this.

Last but not least I would like to thank my parents for far more than I could possible describe here.

Contents

Chapter 1

The Large Hadron Collider

The European Organization for Particle Physics, CERN [1], is currently constructing a new collider, called the Large Hadron Collider (LHC). It will accelerate two counter-rotating beams of protons with an energy of 7 TeV and will bring them to collision with a center-of-mass energy of 14 TeV. The design luminosity is as high as $10^{34}\mathrm{cm}^{-2}\mathrm{s}^{-1}$. Both, the energy and the luminosity of the LHC will be higher than for any existing hadron collider. The high center-of-mass energy gives access to possible new heavy particles while the high luminosity allows to study weak interactions.

The LHC is installed in a 27 km circumference tunnel, situated between Lake Geneva and the Jura mountains, that was originally constructed to house the LEP[1]-collider. LEP was dismantled during 2001 to be replaced by the LHC.

LHC is an unprecedented challenge from the physical, technological and managerial points of view.

1.1 Layout of the LHC

The LHC ring (sketched out in figure 1.1 (a)) consists of eight so-called sectors. The central region of each sector is equipped with bending magnets to keep the beam in orbit. The collision energy of a circulating particle accelerator is determined by its radius and the magnetic bending field. The radius of the LHC machine is given by the already existing tunnel. In order to achieve the extraordinary high center-of-mass energy of 14 TeV a magnetic field of 8.4 T in the dipole bending magnets is necessary. The only practical way to produce such a high field are superconducting magnets. A total of 1300 superconducting bending dipoles will be installed for the LHC. They will be cooled down to $\sim$1.9 K using superfluid helium. In its superfluid state, helium has a much higher heat transmission capacity and much lower viscosity than in its normal liquid state. Thus, it is possible to work with a lower helium flow. The two beam pipes for the two counter-rotating beams are contained in the same cryostat. The cross-section through the cold mass of a LHC

[1] Large Electron Positron Collider, a e^+e^- collider with a center-of-mass energy of up to 200 GeV.

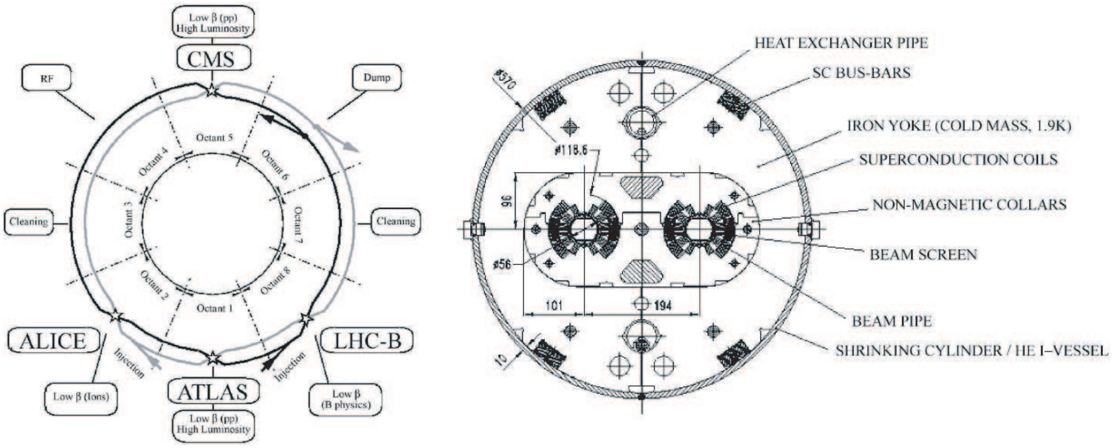

(a) (b)

Figure 1.1: Layout of the LHC machine (a) and cross section of a LHC dipole (b)

dipole is shown in figure 1.1 (b).

Between the bending magnets there are straight sections (so-called insertions) that comprise elements of the accelerator other than bending magnets. These are focusing and defocusing quadrupole magnets that keep the particles on track using the alternating-gradient principle as well as the accelerating RF cavities, the beam dump and the beam cleaning.

At the center of each sector, the beams can intersect. Four of these points are used to carry out experiments. Two of them are high-luminosity intersections where the beam is focused to a small spot.

Apart from protons, the LHC will be able to accelerate Pb-ions, with a center-of-mass energy in the PeV range.

1.2 Physical motivation

The Standard Model of particle physics is a quantum field theory that describes the elementary particles of matter and their interactions. It includes three of the four fundamental interactions: The strong interaction, the weak interaction and the electromagnetic interactions. The gravitational interaction is not described by the Standard Model.

Experiments carried out at LEP and other accelerators found an agreement of the Standard Model with the data up to a precision of 10^{-3} to 10^{-4}. But one important part of the Standard Model lacks still experimental verification: The Higgs mechanism, that explains how the point-like particles of the Standard Model acquire their masses. One experimentally observable consequence of the Higgs mechanism is the existence of a particle with unknown mass called the Higgs boson. Its lower mass limit set by direct searches at LEP is 114.4 GeV. An upper limit of about 1 TeV comes from theory (the Standard Model cannot be consistently formulated with a higher Higgs mass). In order to either discover the Higgs particle or falsify the theory an accelerator covering this energy range is needed. This was the most important motivation to build the Large Hadron Collider.

Although the Standard Model proved to be very successful, it seems to be incomplete. It relies on various input parameters whose values are not explained, neither is there a theoretical justification why there are exactly three generations of quarks and leptons. Furthermore, there are experimental indications that neutrinos do have mass. This has not been accomodated in the Standard Model. Theoretical considerations suggest that it is only a low-energy approximation of a more general theory that includes also gravity. Data obtained by the LHC might give a hint how this theory has to look like.

A high-energy and high-luminosity machine like the LHC provides also the possibility to measure the properties of already known particles with a better accuracy. Many particles (W-boson, b-qark, top-qark ...) will be produced at high rates and thus can be measured accuratly.

Finally, there is the possibility that LHC experiments will find completely unexpected physics, not predicted by any theory.

1.3 Experimental challenges

The particles accelerated by the LHC, protons, are not elementary, but have a substructure. (In contrast of lepton machines like LEP). One can distinguish two types of interactions: collisions at large distances where protons interact via strong long-distance interactions and hard short-distance scattering among the point-like constituents of the protons. Soft proton collisions have a very high cross-section and are called **minimum bias event**. The momentum transfer is small, the final state particles have large longitudinal and small transverse momenta. This kind of events is not very interesting but they are the large majority of all events. Only in the case of hard scattering a large momentum transfer takes place and particles at high transverse energy are produced. These events are interesting for current physics research but relativley rare. At an LHC interaction point, about 10^9 interactions per second take place. At each collision on average 25 minimum-bias events are produced.

Detectors at LHC must have a fast response to avoid so-called **pile-up** due to the high bunch-crossing frequency of LHC (40.08 MHz). Pile-up means that detector channels are occupied by events from previous bunch-crossings that overlap with interesting physics events. The effect of pile-up can be decreased by high detector granularity to reduce the probability that pile-up particles end up in the same readout channel as particles coming from an interesting process. Pile-up particles have in general a small transverse momentum and can be suppressed by a cut on p_T.

The large number of particles produced in each event is also challenging in terms of radiation resistance. In the forward region of an LHC detector up to 10^{17} neutrons per cm^2 and a total absorbed dose of 10^7 Gy is expected during 10 years of LHC operation.

Another problem is the high rate of hard scatterings produces by strong interaction (QCD-background). Since the strong coupling is much bigger than the weak one, these events are a serious background for most of the studied event topologies. This poses stringent requirements on the event selection (trigger) and the data analysis.

1.4 Experiments at the LHC

Four large scale experiments at the LHC are currently under construction: ATLAS, ALICE, CMS and LHCb. ATLAS and CMS are general-purpose detectors while ALICE and LHCb are optimized for heavy ion collisions and to study the properties of the B-meson respectively. This section will deal with ALICE, CMS and LHCb, while ATLAS is described in more detail in the next chapter.

1.4.1 The ALICE experiment

As already mentioned, LHC can also accelerate and collide lead ions producing an extreme energy density at the collision point. It is expected, that for a short period of time the ions will transform into a state of matter that is called quark-gluon plasma. The ALICE (A Large Ion Colliding Experiment) experiment aims to investigate the properties of the quark-gluon plasma by studying the nature of the outgoing particles. On of the big challenges is the high number of particles (about 50 000) that have to be identified and tracked on each event.

The ALICE detector is located at point 2 of the LHC, in the cavern formerly used by the LEP-experiment L3 and re-uses its magnet. The Inner Tracker System of ALICE uses Pixel and Silicon Drift Chambers for vertex reconstruction. The Inner Tracker is surrounded by a Time Projection Chamber with a drift volume of 100 m^3. In fact, it is the largest gaseous TPC ever built. It is able to identify low-energy particles by measuring their energy loss. More energetic particles are detected by a time-of-flight measurement. The sensor for the arrival are Multi-gap Resistive Plate Chambers. Particles with even higher energy are measured with a ring-imaging Cerenkov (RICH) detector. A dedicated photon spectrometer using the same $PbWO_4$ crystals as the CMS calorimeter measures the energy of photons and thus the temperature at the collision point. To measure muons emerging from J/Ψ decays the muon arm of ALICE is used.

1.4.2 The CMS Experiment

The abbreviation CMS stands for 'Compact Muon Solenoid'. Despite its name, CMS is a rather large detector designed as general-purpose experiment. It is built around a large high-field solenoid that provides a field of 4 T. It has a free bore of 6 m that holds the tracker and the calorimeters. The barrel part of the magnet yoke is made of iron and consists of five slices. The central slice holds the coil. The end-caps are made of three slices. The chambers of the muon spectrometer sit inside the return yoke, interleaved with the iron plates. In the barrel region, drift chambers are used while the end-caps are equipped with cathode-strip chambers to deal with the higher particle flux.

The CMS tracker uses two technologies: Silicon Pixel detectors in the high-occupancy region and silicon microstrip detectors in regions with lower occupancy.

The electromagnetic calorimeter of CMS detector is a homogeneous scintillating crystal calorimeter. It uses very dense $PbWO_4$ crystals ($\rho = 8.3$ g/cm^3) that have been developed for this purpose in an extensive R&D program. The scintillating light produced in the crystals is collected by avalanche photodiodes. The hadronic calorimeter of CMS is a sampling calorimeter made of brass absorbers and plastic scintillators. Light from the scintillators is collected by wavelength shifting fibers and is then read out by Hybrid Photodiodes. Both calorimeters are subdivided into a cylindrical barrel section and two end-caps.

1.4.3 The LHCb Experiment

LHCb is designed to exploit the b-physics potential of LHC and to study rare decays. It aims to precisely measure the CP violation in the decays of B-mesons which will be produced at high rate at LHC. Since B-mesons will be preferentially produced in the beam direction the LHCb detector is arranged as a single arm detector.

The LHCb detector system put a lot of emphasis on a high performance trigger system to filter out the small fraction of proton-proton collision that actually produce B mesons. The detector element closest to the interaction point is the so-called Vertex-Locator based on silicon pixel technology. It is followed by the first of two Ring-Imaging Cerenkov detectors. The RICH system is needed to suppress background events and for B flavor tagging. A specially designed dipole magnet with a warm aluminum conductor producing a field of 4 T is placed after the first RICH detector.

The tracker consists of 11 stations, some of them are placed inside of the magnet. The inner stations use silicon microstrip detectors, the outer one uses straw-tube drift chambers. The second RICH elements is placed behind the tracker.

The calorimetry of LHCb consists of an electromagnetic part made of lead absorbers sandwiched between scintillators and a hadronic part with iron absorbers and plastic scintillators. The outermost part of the LHCb arm is the muon system. It consists of five stations. The outer chambers are Resistive Plate Chambers whilst the central region is equipped with Multiple Wire Proportional Chambers.

Chapter 2

The ATLAS Detector

ATLAS is a large-scale general-purpose experiment that aims to cover the largest possible range of physics expected from LHC. The detector is constructed with rotation-symmetry around the beam axis. It consists of a barrel part and two end-caps. It is almost perfectly hermetic, leaving only minimal cracks e.g. between the barrel and the end-caps and the hole of the beam line in the very forward region. The overall size of the detector is 44 m length and 22 m diameter. It has a total weight of 7000 tons.

As shown in figure 2.1, ATLAS consists of several subdetector-systems arranged like the onion-skins. The innermost shell is the Inner Detector followed by the Calorimeters and the Muon Spectrometer.

2.1 The Inner Detector

The task of the Inner Detector of ATLAS is to reconstruct tracks and vertices with high efficiency. It measures the momenta of tracks and the decay vertices of short lived particles and it contributes, together with the calorimeters and the muon system, to the electron, photon and muon recognition. Its acceptance covers the pseudo-rapidity[1] range of -2.5 to 2.5.

Figure 2.2 shows an overview of the Inner Detector. It combines high-resolution detectors at inner radii with continuous tracking elements at outer radii, all contained in a solenoidal magnet with a central field of 2 T.

The highest granularity around the vertex region is achieved using semiconductor detectors: A pixel detector around the interaction point followed by a Semiconductor Tracker (SCT). At least four SCT layers and three pixel layers are crossed by each track. Outside the SCT, a Straw Tube Tracker (TRT) provides continuous track-following. The TRT has a much lower density than the high precision silicon trackers, keeping the total amount of

[1] The direction of a particle coming form the interaction point is usually given by a azimuthal angle ϕ and the pseudo-rapidity η that is defined as $\eta = -\log\tan(\theta/2)$ where θ is the angle between the beam axis and the particle trajectory. The coordinate system of a particle detector is defined in the same way.

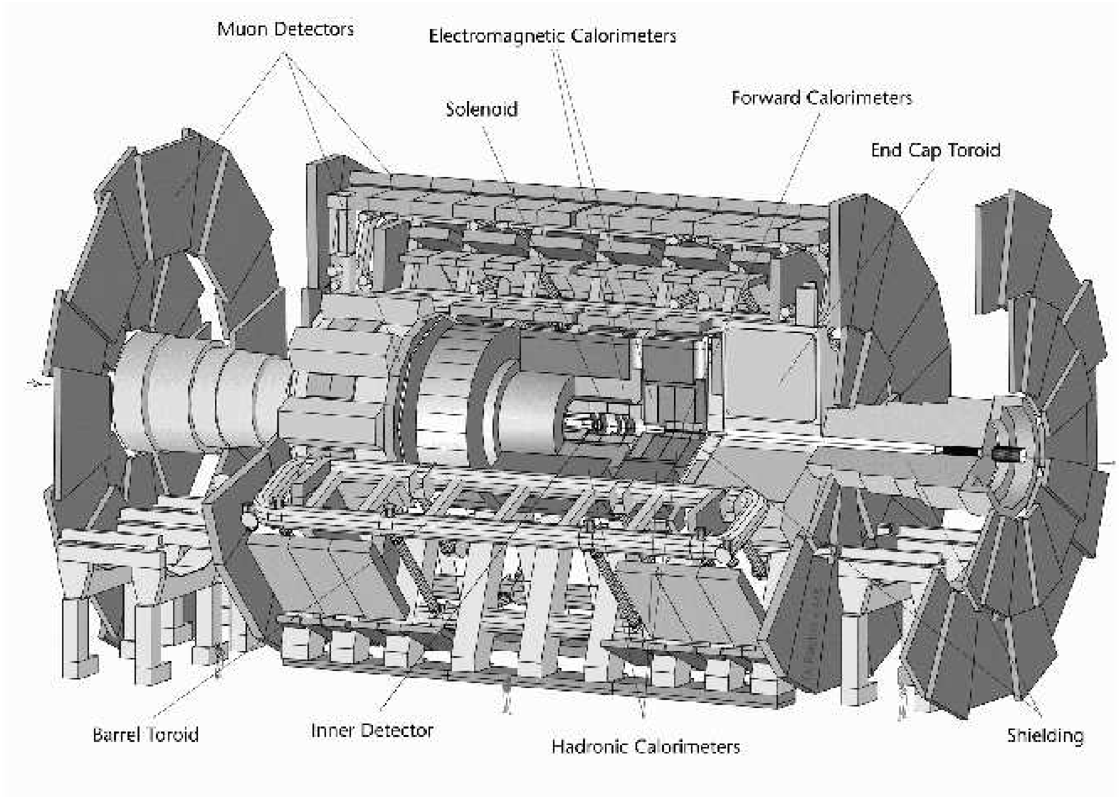

Figure 2.1: Subsystems of the ATLAS Experiment

material upstream of the calorimeters small.

The outer radius of the tracker cavity is 115 cm and has a total length of 7 m. The precision tracking elements are contained in a radius of 56 cm. Mechanically, the inner detector is subdivided into a barrel part and two identical end-caps.

2.2 Calorimetry

The calorimeters in ATLAS are designed to measure the energy and position of electrons, positrons, photons and jets, to give an accurate estimation of the missing transverse momentum and to contribute to the particle identification [3].

The ATLAS Calorimetry system is subdivided into an Electromagnetic Calorimeter and a Hadronic Calorimeter. Both subsystems consist of a barrel and two end-caps. The forward regions are equipped with a dedicated Forward-Calorimeter. Figure 2.3 shows how the calorimeters are arranged inside the detector.

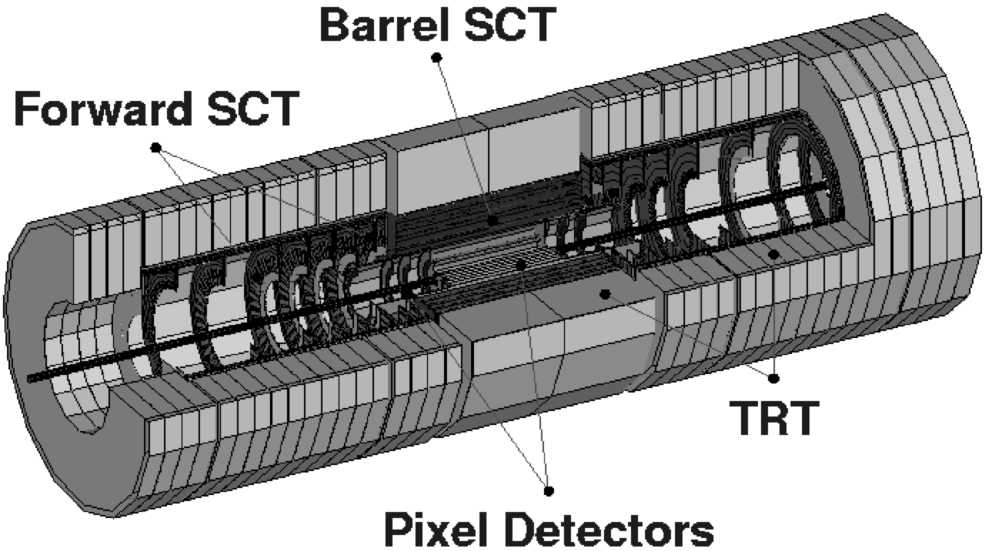

Figure 2.2: 3-D cutaway view of the Inner Detector of ATLAS

2.2.1 Calorimetry Requirements

The design of the ATLAS calorimeters was driven by physics performance requirements as well as technical and financial considerations.

Electromagnetic Calorimetry Requirements

The electromagnetic calorimeter shall be capable to reconstruct electrons from as low as 1 GeV up to 5 TeV. The lower limit is set by the requirements for b-tagging. Though, b-tagging is mainly done by the Inner Detector, a calorimetric identification of low-energy electrons increases the b-tagging efficiency by about 10%. The upper energy limit is set by the possibility to produce new heavy gauge bosons (Z'-boson and W'-boson) that appear in many theories that extend the Standard Model.

Since the energy deposition in a single cell can be as large as 3 TeV, a large dynamic range is required.

In order to achieve a mass resolution of 1% for the Higgs particle in the decay channels $H \rightarrow \gamma\gamma$ and $H \rightarrow 4e$ an excellent energy resolution and linearity in the range of 10 to 300 GeV is needed. The sampling term should be around $\sim 10\%/\sqrt{E(GeV)}$ and the constant term should not exceed 1%. The linearity in this energy range should be better than 0.5%.

Another important parameter is the rapidity coverage that determines the quality of the measurement of missing energy. For technical reasons, the electromagnetic calorimeter is limited to $\mid \eta \mid < 2.5$, the region until $\eta < 5$ is covered by a dedicated forward calorimeter.

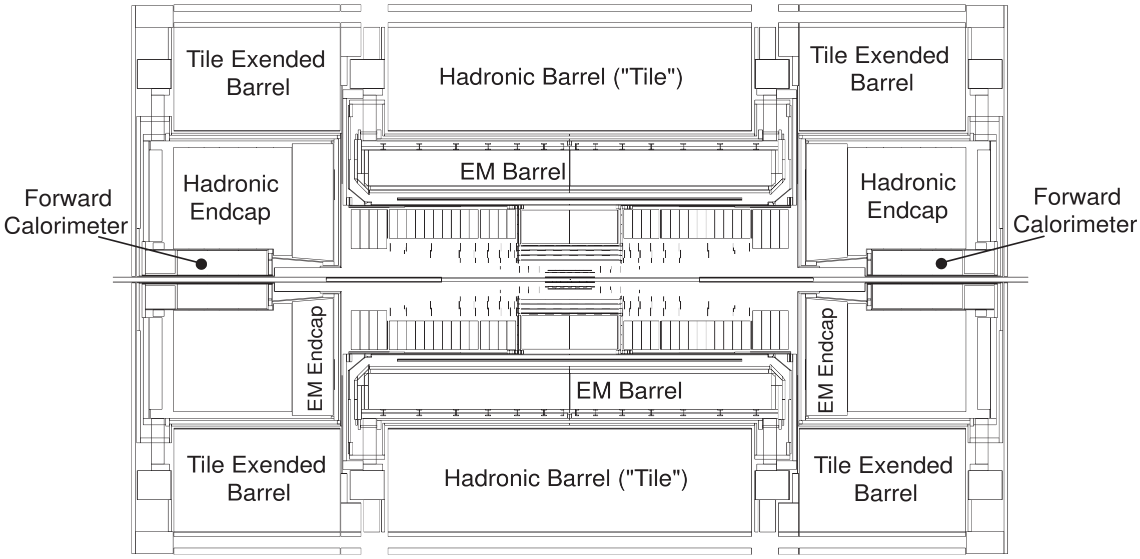

Figure 2.3: 2D view of the calorimeters in the ATLAS detector

Furthermore, the calorimeters have to cope with the effect of pile-up as well as the high radiation dose due to the unprecedented luminosity of the LHC.

Hadronic calorimetry requirements

The required jet-energy resolution depends on the rapidity region. Below η=3, a resolution of $50\%/\sqrt{E(GeV)}$ and a constant term of 3% is necessary. For higher rapidity, $100\%/\sqrt{E(GeV)}$ and a constant term of 10% is sufficient.

2.2.2 Construction

All calorimeters used in ATLAS are sampling calorimeters. The main properties of the different sub-systems are:

Electromagnetic Calorimeter The electromagnetic barrel covers the rapidity region up to 1.475, the EM end-caps go from 1.375 to 3.2 on both sides. It is constructed from lead absorbers interleaved with liquid argon as active material. An extensive description of this technology is given in chapter 3.

Hadronic Barrel Calorimeter The Hadronic Barrel Calorimeter has large steel absorber equipped with scintillating tiles for readout. Therefore this calorimeter is also called Tile-Calorimeter. Each scintillator is connected by wavelength shifting fibers to two photomultiplier. There is a central barrel part covering the rapidity region up to 1.0 and an extended barrel on each side that covers up to a rapidity of

1.7 . The gap between the central and the extended barrel is necessary to guide the cables from the Inner Detector and the electromagnetic calorimeter to the outside. Scintillators placed in the gap will allow a good estimate of the energy lost in this region.

Hadronic End-Cap Calorimeter The Hadronic end-cap uses also the liquid argon technology, but with different geometry. The absorbers are flat parallel copper plates. It is placed behind the EM end-cap in the same cryostat. It covers the rapidity range from 1.5 to 3.2.

Forward Calorimeter The forward calorimeter provides electromagnetic as well as hadronic calorimetry in the very forward region (η between 3.2 and 4.9). It is located in the inner bore of the hadronic calorimeter, around the beam pipe. The first of three forward-calorimeter modules uses copper as absorber, the other two are made of tungsten. To cope with the higher counting rate, the active gaps are much thinner compared to the other liquid argon based calorimeters.

2.3 Muon Spectrometer

In terms of volume, the Muon Spectrometer is the largest part of ATLAS. It consists of a large air-core toroidal magnet system instrumented with Monitored Drift Tube (MDT) chambers to measure the muon trajectory with very high precision in the bending direction and Resistive Plate Chambers (RPC) for triggering. In the End-cap region, Thin Gap Chambers (TGC) are deployed as trigger chambers. The very forward region is instrumented with Cathode Strip Chambers (CSC) instead of MDTs to accommodate the higher counting rates.

The magnet system provides a field of 0.5 T. Three layers of precision chambers allow to measure three points of the bent trajectory. The performance benchmark is to measure the momentum of a 1 TeV muon with a resolution of 10%. Given the magnetic field and the available space, this requires a position resolution of 50 μm.

2.4 Higgs-Hunting with ATLAS

Among many physics goals of the ATLAS experiment, the search for the Higgs boson is the most prominent one. The Higgs discovery potential was one of the benchmarks for the detector design. Depending on the mass of the Higgs particle, different decay channels become available for experimental observation. Some decay channels are very difficult or even impossible to use because of the overwhelming QCD background. The versatility of ATLAS allows to cover the full possible mass range of the Higgs particle. Figure 2.4 summarizes the sensitivity of ATLAS for the discovery of a Standard Model Higgs boson.

In the mass range up to 150 GeV, the channel H$\rightarrow \gamma\gamma$ is the most promising for Higgs searches. Although it has a low branching ratio, the background is rather low. It places

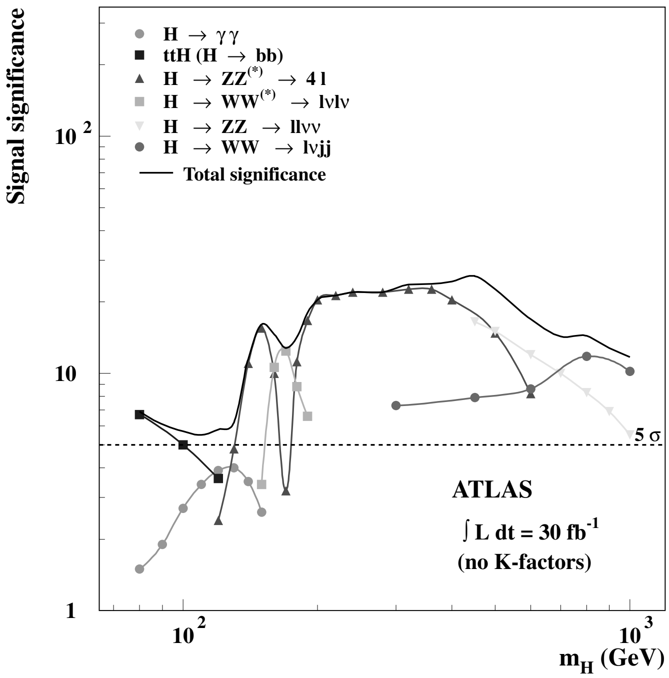

Figure 2.4: ATLAS sensitivity for the discovery of the Higgs Boson after 1 year of running at nominal luminosity.

stringent requirements on the performance of the electromagnetic calorimetry. Excellent energy and angular resolution are needed to discover the narrow mass peak over a $\gamma\gamma$ continuum. The dominant decay channel in this mass region would be H $\rightarrow b\bar{b}$ with a branching ratio of about 90%. But it is very difficult to trigger and extract it as a signal above the QCD background.

The channel H $\rightarrow$ ZZ* $\rightarrow$ 4l provides a rather clean signature in the mass range between $\sim$ 120 GeV and 2 m$_Z$. Above this energy, the gold-plated channel H $\rightarrow$ ZZ $\rightarrow$ 4l opens. The branching ratio is larger than for the $\gamma\gamma$ channel and increases towards higher Higgs mass. Given the design performance of the tracker, the muon system and the electromagnetic calorimeter a mass resolution of 1.42 to 1.81 GeV can be achieved for a Higgs mass of 130 GeV. For a Higgs mass close to 170 GeV the decay mode H $\rightarrow$ WW* $\rightarrow$ lνlν opens up and leads to a dip in the signal significance of the H $\rightarrow$ ZZ* $\rightarrow$ 4l channel.

For a Higgs mass bigger than 700 GeV one needs to detect decay channels containing neutrinos. An excellent missing-energy measurement and an accurate reconstruction of jets in W/Z $\rightarrow$ jj are needed.

Chapter 3

The ATLAS Electromagnetic Calorimeter

The electromagnetic calorimeter of the ATLAS detector is a sampling calorimeter with liquid argon as active material and Lead absorbers [2]. It consists of a barrel part covering the pseudo-rapidity range from -1.475 to 1.475 and two end-caps covering the range from 1.375 to 3.2 at both ends.

Liquid argon is a radiation hard material that allows fast and linear readout at an affordable price. The lead absorbers make the average density high enough to absorb high-energy electrons and photons.

3.1 Principle of operation

When a high-energy electron or positron passes through matter it irradiates bremsstrahlung. The bremsstrahlung photon gives rise to electron-positron pair production. Thus, a cascade of many particles with lower and lower energy builds up until the energy of the particles falls below the threshold for pair production. The remaining energy is dissipated by excitation and ionization.

3.1.1 Processes in the electromagnetic shower

Figure 3.1 shows the energy loss processes of photons and electrons as function of their energy.

Bremsstrahlung

The principal source of energy loss of high-energy electrons or positrons passing through matter is bremsstrahlung resulting from coulomb interactions with the electric field of atomic nuclei. The energy spectrum of the irradiated photons behaves like 1/E. In the limit of very hard bremsstrahlung the entire energy of an electron can be emitted as a photon but this is very rare. In general, the bremsstrahlung photons carry only a small fraction of the energy of the charged particle. The direction of the initial particle changes slightly during such a process. The energy loss of an electron by bremsstrahlung is approximately proportional to the electron energy.

Pair production

Photons with an energy of at least twice the electron rest mass can produce an electron-positron pair in the Coulomb field of an atomic nucleus or an electron. The cross-section for this process rises with energy and reaches an asymptotic value at very high energies (> 1 GeV). For energies above some MeV (depending on the absorber material), pair production becomes the dominant photon interaction process.

Radiation length

The appropriate scale length to describe the development of an electromagnetic shower is the **radiation length** X_0. One radiation length is the mean distance over which an electron looses all but 1/e of its energy by bremsstrahlung. The mean free path for pair-production of a high-energy photon is 7/9 radiation lengths. The radiation length is therefore a characteristic distance for the two processes that shape the electromagnetic cascade.

The radiation length in a material is usually measured in g cm^{-2}. It can be approximated by [8]:

$$X_0 = \frac{A\,716.4\ \mathrm{g\ cm}^{-2}}{Z(Z+1)\ \ln(287/\sqrt{Z})} \tag{3.1}$$

where A is the atomic mass and Z the atomic number of the material.

To measure the energy of the incoming particle accurately, the calorimeter must be thick enough in terms of radiation lengths to contain the electromagnetic shower. To achieve this, a material with high Z and high density is chosen. Lead fulfills this requirement. The ATLAS EM calorimeter is at least 22 radiation lengths thick.

The dominant processes for photons with energies below the limit for pair-production are Compton and Rayleigh scattering as well as the photoelectric effect.

Compton and Rayleigh scattering

Rayleigh scattering is a coherent process; the photon changes its direction by interacting with an atomic electron but does not loose energy. In contrast, a photon that undergoes Compton scattering does transfer part of its energy and momentum to an atomic electron that is put into an unbound state. The process will result in a free electron and a scattered

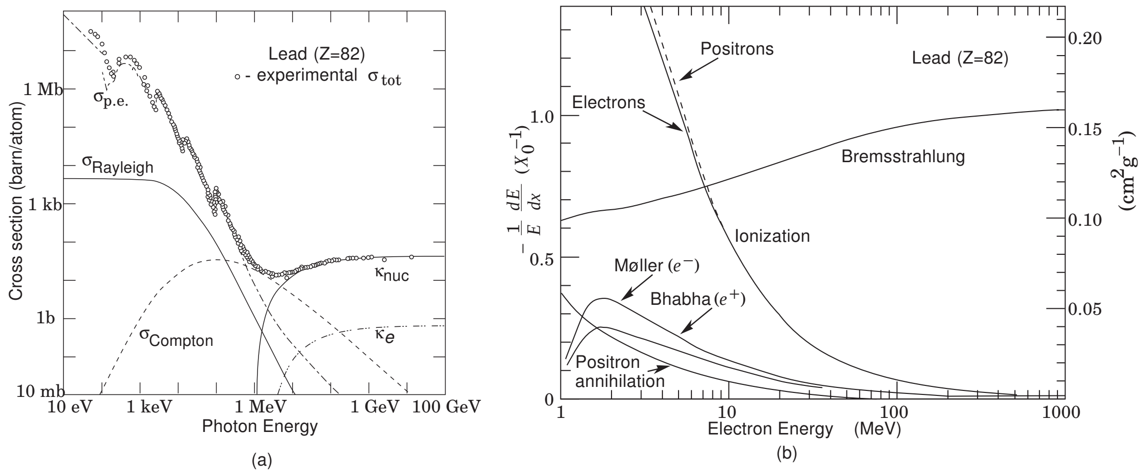

Figure 3.1: (a) Photon cross section as function of the energy in lead showing the contributions of the different processes. (b) Fractional energy loss of electrons per radiation length as function of the energy. Both figures have been taken form [8].

photon. For most absorber materials, Compton scattering is by far the most likely process for photons with energies between a few hundred keV and a few MeV.

Photoelectric effect

At even lower energies, the most likely process is the photoelectric effect, where a photon is absorbed by an atom that in turn emits an electron. The atom is put into an excited state by this process and will return into its ground state by emission of Auger electrons or X-rays. The cross section for the photoelectric effect depends strongly on the electron density and thus on the Z of the absorber material. It scales like Z^n where n is between 4 and 5.

3.1.2 Energy deposit

Charged particles in the shower loose energy permanently by ionizing the material they traverse. For high-energy particles, the ionization loss rate rises approximately logarithmically with the energy.

Electron-Ion pairs created in the liquid argon (active region) are separated by an electric field and drift towards the electrodes inducing an electrical signal that is proportional to the number of electron/ion pairs and thus to the energy deposited in the liquid argon gap.

In a sampling calorimeter like the ATLAS electromagnetic calorimeter, only a fraction of the total energy is deposited in the active part. The ratio of total energy deposit and energy deposit in the active region is called the **sampling fraction**:

$$SF = \frac{E_{Active}}{E_{Passive} + E_{Active}} \tag{3.2}$$

The energy measured in a sampling calorimeter has to be multiplied with the inverse of the sampling fraction to obtain the total energy deposit.

It is important to keep in mind that there are only a few tracks that traverse many active and passive layers and thus deposit a certain fraction of their energy in the active region. The vast majority of particles in an electromagnetic shower has very little energy and a very short range, typically much smaller than the thickness of the layers[17]. A sampling calorimeter samples a certain fraction of the shower energy; a picture of many electron tracks passing many layers would be misleading. In contrast, a muon will indeed pass many layers of the calorimeter, loosing a (small) fraction of it's energy by ionization and induce only a few secondary particles.

Fluctuations

The number of electrons and positrons in a shower produced by a particle with a given energy fluctuates statistically. Since the total ionization signal is proportional to the number of charged particles the reconstruction energy fluctuates in the same way. The relative width of the distribution is equal to $\sqrt{n}/n = 1/\sqrt{n}$ where n is the number of charged particles. Therefore the relative precision of the energy measurement with a calorimeter can be expressed as

$$\frac{\sigma_E}{E} = \frac{a}{\sqrt{E}} \tag{3.3}$$

One can see from this formula that the relative energy resolution of a calorimeter improves with the energy. Therefore calorimeters are very attractive instruments for high-energy particle physics experiments.

Usually, the energy resolution of a calorimeter is expressed in terms of a with the Energy given in GeV. In practice, formula 3.3 has to be extended by a noise term $\frac{b}{E}$ and a constant term c to account for instrumentation effects independent from the shower development like non-uniform absorber thickness. This leads to:

$$\frac{\sigma_E}{E} = \frac{a}{\sqrt{E}} \oplus \frac{b}{E} \oplus c \tag{3.4}$$

For very high energies, the stochastic (sampling) term becomes small and the resolution of the calorimeter is determined by instrumental effects.

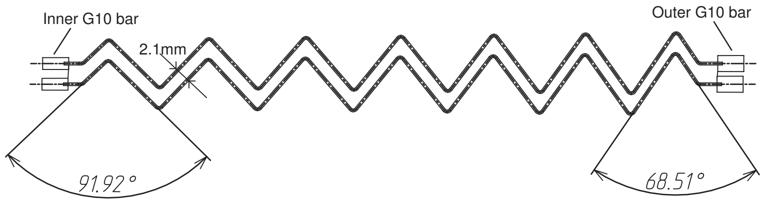

Figure 3.2: Accordion-shaped absorber with constant gap-size

3.2 Construction

3.2.1 Barrel calorimeter

The construction of the ATLAS EM Barrel calorimeter has been finished recently and summarized in [18].

Sampling calorimeters like the ATLAS EM Barrel calorimeter are built in a way that the shower produced by the incoming particle stretches over many layers of active and passive material. In the case of the ATLAS EM calorimeter, this is achieved by bending the absorbers and electrodes into an accordion-shape with the folds approximately perpendicular to the incoming particle track. The absorbers are interleaved with electrodes and stacked up, leaving liquid argon filled gap.

As one can see in figure 3.2, the accordion folds become bigger and their angle smaller towards bigger radii. This accordion structure allows to build a full wheel with constant gap sizes and hermetically uniform azimuthal coverage. Signal and high-voltage cables are routed at the front and back face of the detector, there are no cables inside the detector volume.

The detailed composition of the sandwich is shown in figure 3.3. The read-out electrodes are placed in the center of the gap between two absorbers.

The absorber is made of steel-coated lead and serves as ground electrode. It is 2.16 mm thick, the lead fraction is 1.5 mm thick for pseudo-rapidities smaller than 0.8 and 1.1 mm for bigger pseudo-rapidities. The prepreg layers that glue the Steel coats on the lead sheets compensate for the varying thickness.

The read-out electrodes consist of three copper layers separated by Kapton layers. The two outer layers carry the high-voltage, the inner one is used as signal layer. It collects the current induced by electrons drifting in the liquid argon gap by capacitive coupling. The liquid argon gap is 2.12 mm wide on each side of the read-out electrode. The two half gaps are supplied by different high-voltage channels to minimize the impact of a high-voltage trip or a short.

Some important quantities of the materials used (radiation lengths, dE/dx for minimum-ionizing particles, etc.) are listed in appendix C. Using these values one can calculate the

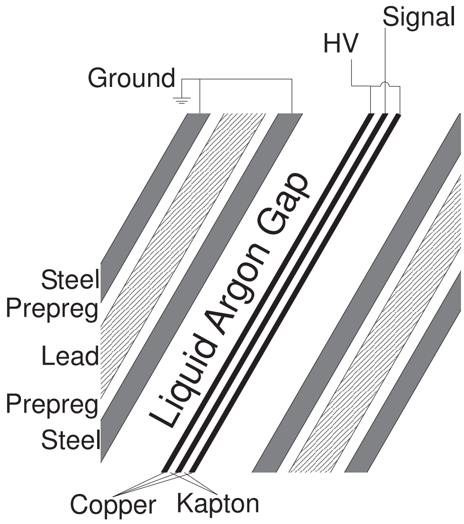

Figure 3.3: Layers of the electromagnetic calorimeter (not to scale).

energy deposit in the active and inactive parts of the accordion and thus the sampling fraction for minimum-ionizing particles. For the low-eta range, a MIP deposits 2.55 MeV in the passive materials (absorber and readout electrode) and 0.89 MeV in the two liquid argon gaps. This yields a sampling fraction of 25%. For the high-eta region, the energy deposit in the active region is only 2.25 MeV due to the lower lead fraction in the absorber. The sampling fraction is therefore 28%. All these numbers are only valid for minimum-ionizing particles. As already pointed out in the previous section, electron showers show a more complex behavior. The sampling fraction for a shower as obtained from a Monte-Carlo simulation is smaller than the numbers obtained by the simple calculation. See section 8.2 for more details about the sampling fraction of the accordion calorimeter.

The choice of thickness of absorbers and active material is a trade-off between sampling fraction (thus the resolution) and total thickness of the calorimeter. For higher pseudo-rapidity, the total thickness of the calorimeter seen by a particle coming from the interaction point increases (see also figure 3.4). This is the reason why a thinner absorber is used for higher pseudo-rapidities.

To ease the construction, the barrel calorimeter is subdivided into two identical half-barrels each consisting of 16 modules. Each half barrel is 3.2 m long and contains 1024 absorbers. The inner and outer diameters of the barrel are 2.8 m and 4 m respectively. Mechanically, the distance between the absorbers is determined by precisely machined bars made of G10 fiberglass-epoxy composite. These bars run along the outer and inner edges of each absorber (see also figure 3.2). The electrodes are held in the middle of the gap by strips of honeycomb spacers laid in the straight section of the accordion. The G10 bars are screwed to six outer and inner support rings made of stainless steel that give the necessary rigidity

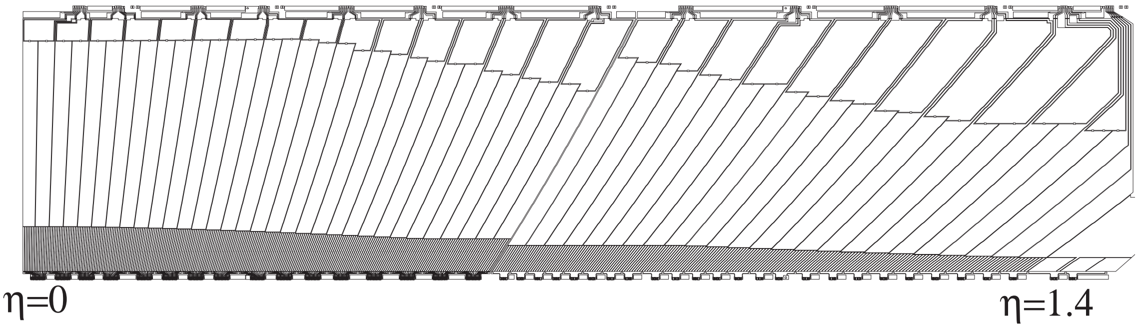

Figure 3.4: Signal layer of the barrel electrode.

Compartment	$\Delta\eta$	$\Delta\phi$ (# of electrodes)	Depth in X_0
Front	0.025/8	$2\pi/64$ (16)	2.5 - 4.5
Middle	0.025	$2\pi/256$ (4)	16.5 - 19
Back	0.05	$2\pi/256$ (4)	1.4 - 7

Table 3.1: Granularity of the different layers of the EM barrel calorimeter.

to the whole structure. G10 has the same thermal expansion coefficient as the stainless steel of the support rings.

Granularity

The electromagnetic barrel calorimeter is subdivided into 150 000 individual cells. The number of cells is a trade-off between achievable position resolution and complexity of the readout system. Also noise plays a role, since larger cells pick up more noise.

In phi, cells are realized by connecting neighboring readout-electrodes together. The segmentation in eta and in depth is done by etching the copper of the signal-layer of the electrode like a printed-circuit board. The layout of one electrode is shown in figure 3.4. The cells have 'pointing' orientation. This means the border lines point to the interaction point.

The accordion part is subdivided into three compartments (also called 'samplings') in depth. The first one has a fine granularity in eta (therefore sometimes called 'strips'-compartment) but is coarse in phi. It is between 2.5 and 4.5 radiation lengths thick. The middle compartment is the thickest one; the bulk of the energy is deposited here. Each middle cell covers 8 front cells in eta but only 1/4 of a front cell in phi. The back compartment is even coarser, it serves mostly to catch the end of an electromagnetic shower and to estimate longitudinal leakage. The granularity of the different compartments is summarized in table 3.1.

3.2.2 Barrel presampler

The presampler is a thin (11 mm) active layer of liquid argon in front of the sampling calorimeter. It should allow to correct for energy loss upstream of the calorimeter. The presampler is subdivided into 32 identical azimuthal sectors (each spanning $\pi/32$ in ϕ) per half-barrel. Each sector consists of eight modules, each covering a region of 0.2 in η. Consequently, the modules have unequal length. Figure 3.5 shows a photograph of a presampler module.

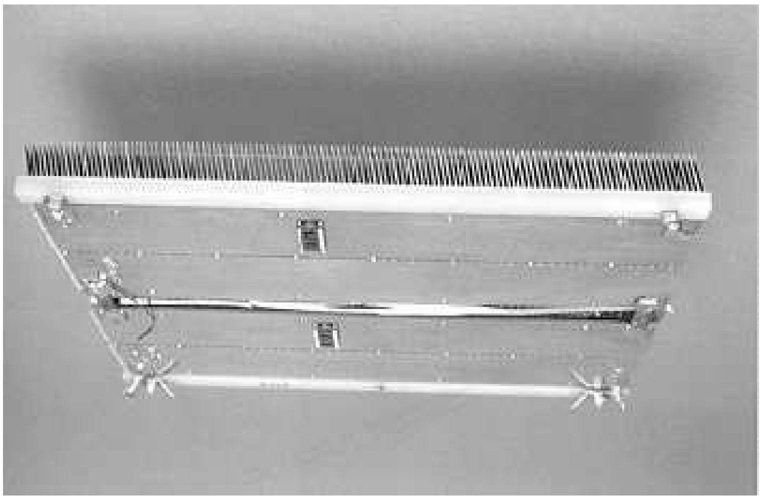

Figure 3.5: Photograph of a presampler module

Each sector is enclosed by a 0.4 mm thin glass-epoxy shell. The electrodes lie in the (r,ϕ) plane, so the electrical field is perpendicular to the one in the barrel calorimeter. The gap between two electrodes varies from 1.96 mm to 2.0 mm. The operating voltage is 2 kV. At low η, the electrodes are slanted with respect to the normal axis to avoid particles going only through the electrode. The presampler has a granularity of $\Delta\eta = 0.025$, $\Delta\phi = 0.1$. This is done by etching the electrode in two ϕ compartments and connecting an appropriate number of electrodes in η.

The electrodes are realized as multi-layer circuits. The cathode is double sided, the anode has three layers. Similar to the signal electrode in the barrel calorimeter, the two outer layers carry the high voltage while the inner one is used to read out the ionization signal via capacitive coupling.

3.3 Electronic signal processing in the EM calorimeter

3.3.1 Electronic installations in the cryostat and feedthroughs

The connections from the cells pad to the edge of the electrode are done by etched lines on the copper of the electrode. The front compartment is read out on the inner radius, middle and back compartment on the outer radius. So-called summing boards are soldered directly on the signal electrodes. They interconnect electrodes belonging to the same read-out cell according to the desired ϕ-granularity (see table 3.1).

The so-called Motherboards are placed on top of the summing boards and provide readout for cells of a region of $\Delta\eta \times \Delta\phi = 0.2 \times 0.2$. They distribute also the calibration pulses to the cells using precision resistors (see section 3.4).

The signal from the motherboards is guided through mini-coaxial cables to patch panels (located at the outer ends of the two half barrels) and to the signal feedthroughs. According to the cable length and capacitance of the detector cells two different cable impedances have been chosen: 25 Ω for the middle and the back section and 50 Ω for presampler and front cells.

The feedthroughs provide the electrical connections through the cryostat walls with minimal heat loss. They consist mainly of a cold and a warm flange connected by flexible bellows to allow the movement due to thermal contraction of the inner cryostat vessel. For better insulation, the space between the two flanges is pumped down to $\sim 10^{-3}$ mbar. Flat polyamide strip-line cables connect the warm and the cold flange. Their impedance is 33 Ω, a compromise between the 25 Ω and the 50 Ω cables used inside of the cryostat. There is one feedthrough per module each equipped for 1920 signal lines as as well as calibration and monitoring cables.

3.3.2 Front-End electronics

The Front-End electronics is housed in so-called Front-End crates that sit directly at the feedthroughs, as close as possible to the cryostat. One Front-end crate covers two feedthroughs. The signal cables end at the backplane of the Front-End crate where the Front-End boards (FEB) are plugged in. To equip one feedthrough, fourteen Front-End Boards plus one Monitoring board, one Controller board, one Calibration board and one Tower-builder board are needed.

The elements on a Front-End board are schematically shown in figure 3.6. On the Front-End boards, the signal is amplified, shaped, sampled and digitized. Each FEB can process the signals of up to 128 cells. There are a few FEBs where not all channels are actually connected to calorimeter cells.

The first element of the read-out electronics chain is the preamplifier. This is a current-sensitive low-noise amplifier. Depending on the kind of cell (presampler, front, middle or back) a different preamplifier is used to account for the different ionization current and

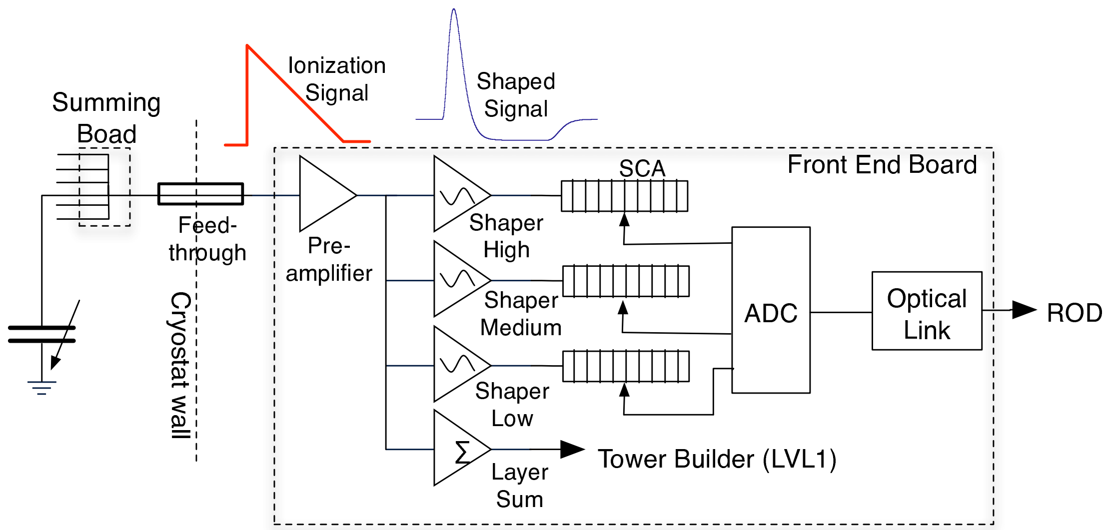

Figure 3.6: The most essential elements of the Liquid Argon Calorimeter readout electronics from the calorimeter cell until the digitization.

cell-capacitance. Each FEB serves only channels of one kind so they are equipped with the same type of preamplifier. One has to distinguish different flavors of FEB depending on their preamplifier-type.

The purpose of the shaping amplifier that is located right after the preamplifier is to optimize the signal-to-noise ratio. The chosen architecture consists of one differentiator to shorten the tail of the ionization signal followed by two integrators to limit the bandwidth and thus the electronic noise. The triangular signal is transformed into a short peak and a long undershoot (see figure 3.7). This peak amplitude is still strictly proportional to the energy deposit in the cell. In case of pile-up (energy deposit in the same cell in subsequent events) the peak of the second signal is superimposed with the undershoot of the preceding pulse. For each calorimeter cell, there are three shapers with different gains. The gain ratio is approximately 1:10:100. This makes a better use of the dynamic range of the ADC.

The shaped signal is sampled at 40.08MHz (this is the bunch-crossing frequency of the LHC) and the values are stored in an analog pipeline (Switched Capacitor Array, SCA) where they wait for the decision from the first level of the trigger system (LVL1). There are three SCAs per cell for the three gains of the shaper. The sampling phase is adjusted in a way that one sample is close to the signal peak. The SCA can hold 144 samples. Given the sampling frequency, the depth of the SCA is largely sufficient to cover the maximal latency of the first level trigger (max. 2.4 μs). The actual latency of a LVL1-accept is a configuration parameter of the Front-End boards that determines which of the 144 stored samples are to be digitized.

Only if an event is accepted by the first level of the trigger system (LVL1), the digitization

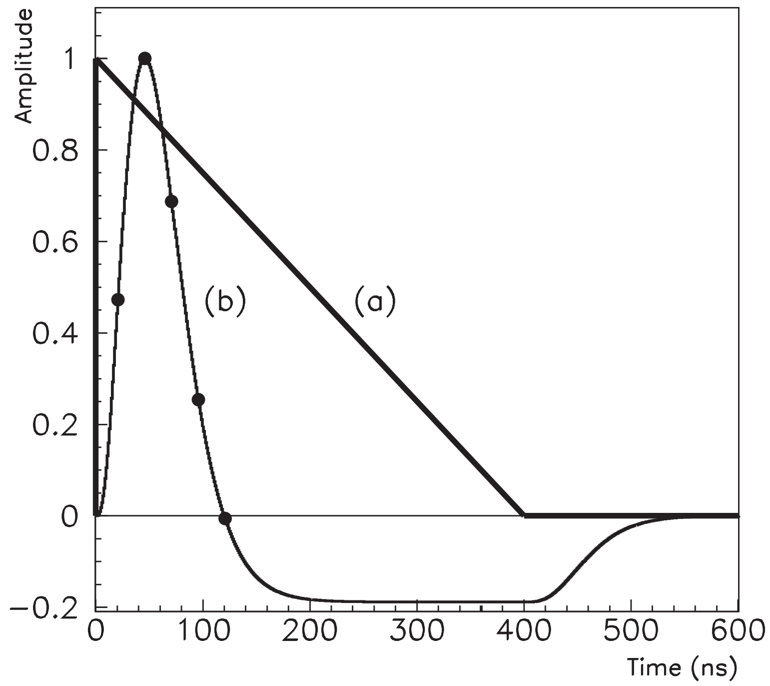

Figure 3.7: Form of the ionization signal (a) and the shaped ionization signal (b). The five points where the signal is sampled are also indicated.

takes place. Liquid Argon Calorimeter electronics can cope with a LVL1 trigger frequency of 75kHz. In normal mode, it is planned to read five consecutive samples, arranged in a way that the maximum is at the second sample. The hardware allows to record up to 32 samples. In automatic gain mode, the gain selection logic uses the second ADC sample to decide which of the three gains is the appropriate one. The lower limit for medium gain is approximately 1300 ADC counts, the upper one is approximately 2500. This ensures that no element of the electronics chain saturates. Alternatively, the FEBs can be configured to run in fixed gain mode.

The digitized samples of all channels of a FEB are sent over an optical link (GLINK) to the Read-out driver (ROD). The RODs are located in the counting room, away from the detector.

A FEB accommodates a quite large number of electronics elements that dissipate a significant amount of heat. To keep the temperature of the electronics and the surrounding detectors at an acceptable level, water cooling is required. This is done by a 'leak-less' underpressure water circuit.

3.4 Calibration system

The stability and uniformity of the ionization signal in Liquid argon can easily deteriorate by imperfections of the readout electronics. To avoid this, a precise calibration system was developed that allows to measure the response of the electronics chain in-situ. This is done by injecting a pulse with a known amplitude and a shape similar to the one of the ionization pulse close to the point where the ionization current is picked up. The components of the calibration system are schematically drawn in figure 3.8.

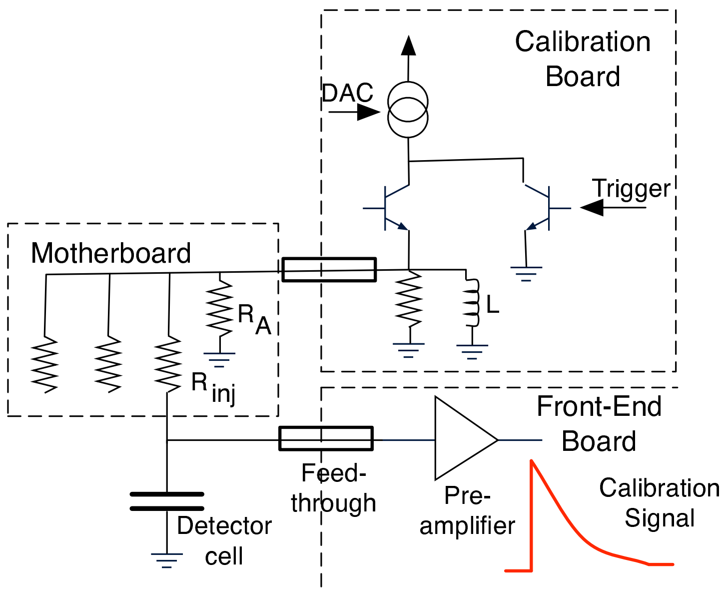

Figure 3.8: The electronic calibration system. A calibration pulse is generated by switching the inductance L that is fed by a precision current source. The same pulse is split among several calorimeter cells via a resistive network on the motherboard.

The calibration signal is produced by interrupting a current through an inductance. This leads to a signal with a short rise time and an exponential decay instead of a linear decay like the ionization signal. The current is set via a digital to analog converter (DAC). The DAC value determines the amplitude of the calibration signal. The pulsers are located on a calibration board in a warm environment but as close as possible to the detector. This boards are installed in the same Front-End crates as the FEBs. Only the resistive network to distribute the signal to many calorimeter cells is located inside the cryostat, more exactly on the motherboards. The set of cells that is connected to the same calibration line is chosen in a way that cross-talk studies can be carried out, e.g. direct neighbors are not pulsed by the same line. One calibration line pulses 16 presampler cells or 32 front cells or eight middle or back cells. In this way, a full barrel module can be calibrated with the 64 pulsers of a single calibration board.

The calibration resistors on the motherboard have a tolerance of 0.1% at 90K. Their value varies depending on the dynamic range of the cells. The calibration resistor for the front cells has 3 kΩ, the one for the back compartment and the middle compartment at $\eta < 0.8$ has 1 $k\Omega$. The middle cells with higher η are equipped with 500 Ω resistors.

An additional feature of the calibration board is a programmable delay chip on the trigger line that allows to delay the pulse in steps of 1 ns. The parameters of the calibration board include the DAC setting (determines the injected current), the delay setting, and pattern of pulsers to be used.

3.5 Off-Detector electronics

The first element of off-detector electronics is the Liquid Argon Calorimeter Read-out Driver (ROD). It receives the ADC samples sent by the FEBs over the optical link. Each ROD reads the data from eight FEBs. The most essential components of a ROD are the input FPGA[1] that re-arranges the samples, a Digital Signal Processor (DSP) and a output FPGA that concatenates the data from two FEBs. Each ROD has four optical outputs sending data to the Read-out system which is the next step on the ATLAS data acquisition chain.

There is one DSP per FEB, in total they have a significant computing power and are very flexible. It is planned to do the first reconstruction step, the calculation of the cell energy out of the raw ADC samples, already at this stage. In this case ('physics mode'), the output contains a roughly calibrated cell energy in MeV. This is mandatory to allow the second level trigger a fast evaluation of the energy deposit in the calorimeter. The DSP can also forward the raw data unchanged to the output. This mode ('transparent mode') is used e.g. for beam tests.

3.5.1 Data encoding

The raw data acquired by the Liquid Argon Calorimeter and the other ATLAS subdetectors are written to byte stream files and stored on the CERN tape archives. This byte stream is compiled jointly by the Read-out Drivers that differ from subdetector to subdetector and the common ATLAS Data Acquisition system.

The byte stream format consists of a hierarchical system of fragments that reflect the read-out chain of ATLAS [10]. Each fragment contains a header and a several sub-fragments. The uppermost one is the so-called Full-Event Fragment that contains various sub-detector fragments. The lowest level in the fragment hierarchy are the ROD-Fragments (produced by the Read-out drivers) that contain the raw data from the detector.

The encoding of the data inside the ROD-fragment is up to the sub-detector communities

[1] The abbreviation FPGA stands for Field Programmable Logic Gate Array. This devices contain a number of boolean elements, Flip-Flops, etc. that can be interconnected in a flexible, programmable way.

while the overall structure of the byte stream is under the responsibility of the ATLAS TDAQ group. At the time of writing, the format of the Liquid Argon Calorimeter ROD fragment as well as the fragment hierarchy are being revised in the light of the experienced collected during the combined beam test.

Chapter 4

Software overview

4.1 The Athena reconstruction software framework

Athena [7] is the name for the ATLAS reconstruction software framework. It's a flexible object-orientated C++ based framework that is currently developed by the ATLAS collaboration. It incorporates various other frameworks like ROOT[1]. The framework provides basic services like I/O-services, histogramming, an event loop manager and allows to hook in user algorithms in a flexible way. An Athena job is configured by so-called job option files that are written in the python scripting language. These job option files define what modules like services, algorithms, etc, are to be executed and allows to pass parameters (called *properties*) to these modules. The necessary shared objects are loaded dynamically before the event loop actually starts.

Athena will be also used in the ATLAS trigger system. Dedicated multi-threaded versions of Athena are running Second Level Trigger (LVL2) and the Event Filter (EF) to provide fast reconstruction and monitoring.

4.1.1 Main components of Athena

Data objects Data objects in Athena are objects in the sense of object oriented programming, they are instances of C++ classes. Their purpose is to hold a certain type of (event) data e.g. a particle track. In general, data objects have no algorithmic capabilities.

Algorithms Algorithms are typically used to process event data. They have an *initialize* and a *finalize* method that are executed at the beginning and the end of a job and an *execute* method that is executed for each event.

AlgTools are used for code that is shared between different algorithms. Like algorithms they have *initialize* and *finalize* methods but no *execute* method. Any user method

[1]ROOT is an object-oriented data analysis framework that has been developed at CERN.

has to be called by a top-level algorithm.

Converters Converters convert data between a transient and a persistent representation. For instance, the raw data is read in by the byte stream converter and histograms are written by the histogram converter.

Stores In Athena, data objects are kept in Stores. This concept allows to decouple algorithms, tools, etc, from each other. Data objects can be recorded to a store by one algorithm and retrieved by another one that does not know anything about the first algorithm. There are two Stores in Athena. The *Transient Store* keeps event data, it is cleared at the end of each event. The *Detector Store* is made for data object with longer validity like the detector geometry or conditions data.

4.2 EM calorimeter reconstruction software

Figure 4.1 gives a graphical overview of the algorithms and data objects involved in the energy reconstruction for the Liquid Argon Calorimeter. The steps that are necessary to get from raw data to physics analysis objects and how they are implemented in the Athena framework will be explained in the following sections and chapters. The algorithm structure reflects the overall calibration strategy for the calorimeters in ATLAS as sketched out in [11]. The aim of the calibration strategy is to provide the best possible energy measurement for offline physics analysis as well as for the trigger system. Therefore a raw calibration is already performed online at the RODs, the input for the Level 2 are already roughly calibrated cell energies. This calibration (in more detail explain is section 6) is linear and can be un-done in order to apply a more refined calibration.

4.2.1 Event data objects

This section lists the data objects that participate in the energy reconstruction process. Usually there is one object per readout channel. The objects are collected in containers similar to vectors known in the C++ Standard Template Library. These containers are recorded in the transient data store where they can be accessed by any algorithm. Data objects important for the Trigger are stored in special 'identifiable' containers that allow fast access to specific regions of the calorimeter.

Identifier

There are two kinds of identifiers to specify a certain calorimeter cell. The *Online identifier* describes the location of the cell in the readout system, like Feedthrough number, Front-End Board number and channel number on the board. The *Offline identifier* describes the geometrical position of the cell in terms of eta, phi and layer. Both identifiers are actually bit maps stored as integer numbers. Dedicated helper classes allow decoding and encoding

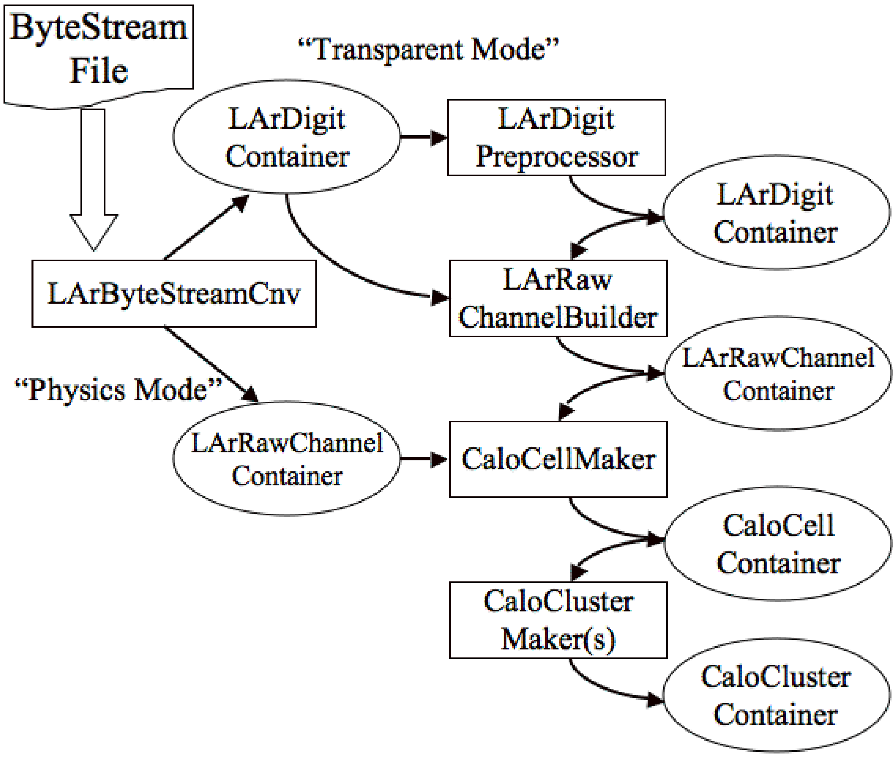

Figure 4.1: Data objects and algorithms used for the calorimeter energy reconstruction. Data objects are drawn as ovals, algorithms as rectangles.

the information. The so called cabling service allows to convert an offline identifier into an online identifier and vice-versa.

LArDigit contains the raw ADC samples as they are recorded by the front end board together with the gain and an online-identifier.

LArRawChannel contains the roughly calibrated energy of a cell in MeV together with the peak time of the signal and a quality factor. See chapter 6 for more details about these quantities. The online-identifier and the gain are also part of this class.

LArCell contains very similar quantities as the LArRawChannels. But the energy is supposed to have a refined calibration and the identifier is the offline-style. LArCells derive from CaloCell that is the common base for cells from the Tile calorimeter and the Liquid Argon Calorimeter. LArCells hold also a pointer to the Detector Description Elements. This is a collection of mainly geometry based information for each cell.

CaloCluster contains the energy, size and position of a cluster as well es pointers to the cells the cluster consists of. These cells may belong to the Liquid Argon Calorimeter or to the Tile Calorimeter, since a cluster can span over sub-detector boundaries.

The calorimeter clusters are input to downstream analysis packages like the jet reconstruction or e/γ reconstruction that use information from several subdetectors.

4.2.2 Byte stream conversion

The converter to read-in raw data of the Liquid Argon Calorimeters resides in the package LArByteStream. It makes use the general byte stream conversion service that reads in the raw data file and breaks down the fragment structure into ROD fragment that are subsequently decoded by the LAr byte stream converter.

The exact content of the ROD fragment depends on the code running in the DSP that in turn depends on the kind of run (i.e. physics, calibration, testing). A block-type and a version word in the ROD header allows the decoding routine to distinguish different encoding schemes and versions.

Depending on the data block type, the byte stream converter can produce either LArDigits, LArRawChannels or LArCells. The latter is intended for the Trigger. In this case the intermediate step of LArRawChannels is omitted and the converter directly calls the recalibration tools typically used during the cell making process. LArDigits reflect the raw data if the DSP was running in transparent mode, LArRawChannels correspond to the output of the DSP physics mode.

The byte stream converter is not only used to read in raw data, but is also able to write out data as if they would come from the detector. This is very useful to encode data obtained by Monte-Carlo simulation in a way that it can be used for tests of the trigger system. During the preparation of the combined beam test we used this feature also to convert data files from previous beam tests into the new format in order to debug the analysis and monitoring software before the beam test actually started.

Implementation

Converters in Athena are generally only called if the corresponding data objects are requested. If a algorithm tries to retrieve a certain data object from the transient store that is not present but a converter for this kind of object is registered, then the converter gets triggered.

There is one converter class for each data object that can be converted, but these classes used common tools for this task. The encoding and decoding depends of course on the block type. There is a dedicated class block type and version. These classes derive from a common base class that defines the interface that is used by decoder and encoder tools. The handling of the different block types and versions is completely transparent to the user.

4.2.3 Preprocessing

The cell energy reconstruction algorithm expects one single LArDigitsContainer that in general contains raw data taken in free gain mode. In previous beam tests raw data were sometimes taken in fixed gain mode, where the data from all channels were recorded in high and medium gain. In this case, two containers are created with keys according to the gain. The LArDigitPreprocessor algorithm is able to merge these two containers into one. It picks the right gain using job-option defined thresholds. It is also able to strip off leading or trailing ADC samples. In the case of the 2004 end-cap beam test, it is also used to correct for a systematic bias on the ADC samples.

For reconstruction of 2004 combined beam test runs, this algorithm is not necessary.

4.2.4 Cell energy reconstruction

The cell energy reconstruction is done in two steps. The first step includes the calculation of the peak of the ionization signal and a rough calibration as described in section 6. In terms of data objects, this step produces LArRawChannels out of LArDigits. As already mentioned, it is planned to perform this calculation online by the Digital Signal Processor on the Read-out Board.

The calibration applied in this step is purely linear: there is one μA to MeV factor per cell and gain. This calibration can be easily un-done offline.

There is an Athena algorithm called LArRawChannelBuilder that emulates the functionality of the DSP for data taken in transparent mode. More details about the implementation of this algorithm can be found in section 6.

The second steps involves a refined calibration taking into account slight non-linearities of the electronics and all other cell-dependent corrections. This includes for example correction for high-voltage failures. At this point cells from the Liquid Argon Calorimeter and from the Tile calorimeter are merged into a common container.

The cell correction are implemented as AlgTools, there is one tool per correction. The top level algorithm CaloCellMaker loops over all cells and calls all registered correction tools for each cell. This avoids iterating the multiple times over the same container.

4.2.5 Clustering

The next step after reconstructing individual cells is to form a cluster of cells around the impact point. Various methods and cluster sizes are used in parallel.

Topological clustering The topological clustering algorithm builds a variable size energy blob around a seed cell. It uses the measured noise in every individual cell to determine if it has to be included in the cluster or not. For hadronic clusters this is the most suitable clustering algorithm.

Sliding Window Sliding window cluster are mostly used for electromagnetic clusters. They have a fixed size (3×3, 5×5, 5×7) and are placed in such way that they contain most of the cluster energy.

Testbeam cluster This type of clusters is mainly used for detector studies in a beam test environment. It builds a 3×3 cluster around the hottest middle cell. It works only in the electromagnetic calorimeters while the other clustering algorithms work across subdetector boundaries.

4.3 Reconstruction output

Depending on the configuration, the result of a reconstruction job can be very different. In final ATLAS and in simulation today the output has the form of ESD or AOD files that are the input to actual physics analysis.

ESD stands for Event Summary Data, it contains reconstructed and calibrated detector data. For example in the case of the calorimeters it is planned to store cells (in a compact representation) and clusters in the ESD. ESD files are much smaller (less than 500 kByte per event) than raw data files. Only for a fundamental re-calibration of detector data it is necessary to go back to raw data files. Everything else can be done on ESD files.

The acronym AOD stands for Analysis Object Data. AOD files contain a reduced event representation, derived from ESD. It is meant as input for physics analysis.

In case of beam test data, the most common form of output are ROOT ntuples that can be used for analysis on the detector level and for visualization of results. Since this output ntuple is produced jointly by different algorithms it is called Combined Ntuple or CBNT. Depending on the configuration a CBNT may contain real raw data (ADC counts) but in this case the output file quickly becomes very large. The standard CBNT for calorimetry contains the energy of each cell, the cluster variables as well as the summed up energy in each compartment.

4.4 Geant4 in Athena

One important ingredient to understand the characteristics of the energy deposit in a calorimeter is the Monte Carlo simulation. The ATLAS collaboration has chosen to use Geant4 [9] as the main simulation tool. It was shown that Geant4 describes electromagnetic interactions with a good accuracy. Geant4 is incorporated in the ATLAS software framework. It is configured by python-based job options like any other part of Athena. The geometrical description of the ATLAS detector as well as all the variants of the combined beam test setup are readily available.

The output of the detector simulation are so-called *Hits*, an energy deposit in a certain active volume of the detector. In case of the calorimeter, this volume corresponds to a cell.

At this point, the effect of the varying electric field in the accordion folds is simulated as well. The hits can be stored in POOL files for further processing or written to a ntuple for visualization with ROOT. During the digitization step the simulated hits are converted to a raw-data like format. This involves introducing effects of the readout chain like electronic noise and cross-talk. This is in general done applying correction factors not by a detailed simulation of the detector readout. The file obtained at the digitization can be fed into a reconstruction job that is almost identical to the reconstruction of real data and produces the same combined ntuple.

An important feature of the ATLAS simulation software are the so-called *Calibration Hits*. This allows to access the energy deposited in all regions of the detector, including inactive regions like the absorbers of the calorimeter or 'dead' regions like the cryostat subdivided into electromagnetic and hadronic interactions as well as invisible energy and escaped energy. Calibration hits labeled as 'active' give the true energy deposit the active part of a certain cell. The normal hits in contrast give the energy deposit corrected by the electric field effects in the accordion folds.

To get even more detailed information from a simulation job one can invoke a user defined stepping action. This is a piece of code that is executed on each Monte Carlo step and can be used for example to produce user-defined histograms.

Chapter 5

The ATLAS 2004 combined beam test

In summer 2004, the ATLAS Collaboration carried out an extensive beam test program in the H8 beam line at CERN's Superproton-Synchrotron (SPS). Many beam tests of ATLAS detector elements took place in previous years but this was the first time that all sub-detectors of the barrel part of the ATLAS experiment were tested together. Since the detector construction phase is coming to its end (the ATLAS EM Barrel Calorimeter was installed in the experimental area in fall 2004) as no further beam tests are planned the 2004 combined run offers a unique opportunity to study in detail the single detector performance and also the combined performance of all ATLAS subsystems.

5.1 The H8 SPS beamline

The beam in the H8 beam line is produced by protons extracted for the SPS at energies up to 450GeV. The typical intensity of the primary beam is about 10^{12} protons per burst. The proton beam from the SPS is guided to the T4 target, where a shower of secondary particles is produced.

As target, a 30 mm Beryllium plate is used. In standard conditions, the secondary beam in the H8 beam line can be adjusted between 10 GeV and 400 GeV for negative polarity or up to 180 GeV for positive polarity. A secondary filter target can be used to achieve a higher electron or pion fraction in the beam. As target, one can choose either 8 mm lead, 18 mm lead or 1 m of Polyethylene. From the resulting momentum spectrum of particles, a certain energy is selected by a vertical magnetic spectrometer.

In addition, the H8 beamline offers the possibility of very low energy beams. To achieve this, the beam is directed on an additional target further downstream (T48) and a dedicated magnetic spectrometer.

5.2 Setup of the combined beam test

One of the most important goals of the 2004 beam test was to test the different sub-detectors in a configuration as close as possible to the ATLAS geometry. The sub-detector modules in the beam line mimic a slice of the ATLAS barrel [12].

The beam test started in June with a combined calorimeter run (only EM and Hadronic Calorimeter). The other sub-detectors were added gradually until a full combined setup was reached by the end of August.

Since the H8 Beam Line already set the stage for previous (non-combined) ATLAS beam tests many elements could stay as they have been. Others had to be changed in order to get closer to the ATLAS geometry. The most important (and mechanically complicated) modification was the setup of the combined calorimeter table. The already existing Tile Calorimeter table was extended to accommodate also the liquid argon cryostat.

One EM Barrel Calorimeter module is placed inside the liquid argon cryostat. It is a prototype module (called M0) that has been re-built for this beam test and is now identical to a production module. Since the cryostat is significantly bigger than the module an Argon-Excluder was installed in front of the module. Otherwise the liquid argon (which is a rather dense material) would constitute a large quantity of inactive upstream material. The Argon-Excluder is a block of *Rohacell*, a rigid-foam with very low density.

Behind the cryostat there are three Tile Calorimeter Modules stacked. Two of these are actually production modules. Meanwhile they have been moved to the ATLAS experimental area to complete the Tile Calorimeter Barrel.

The calorimeter modules are placed orthogonal to the beam line. The weight of the two calorimeters amounts to 82 tons.

The table (a photograph is shown in figure 5.1) can be rotated around the vertical axis and shifted orthogonally to the beam. A combination of these two movements allows to simulate different impact points in η. Since the table cannot be inclined, different impact points in ϕ can only be simulated by deflecting the beam with a magnetic field.

Upstream of the calorimeters, two huge magnets where situated: the so-called Morpurgo magnet and the MBPSID magnet that provided the magnetic field for the inner detector. The SCT and Pixel modules have been placed inside of this magnet. Six pixel modules have been used, with an active area of 60.8×16.4 mm^2. The SCT setup used in the beam test consists of two layers with two modules per layer, covering an area of 120×120 mm^2. The TRT modules, consisting of barrel wedges, were placed between the calorimeter table and the Inner Detector magnet.

Downstream of the calorimeter table a massive concrete block was placed to stop all particles except for muons. Behind this beam dump, several stations of muon chambers have been placed.

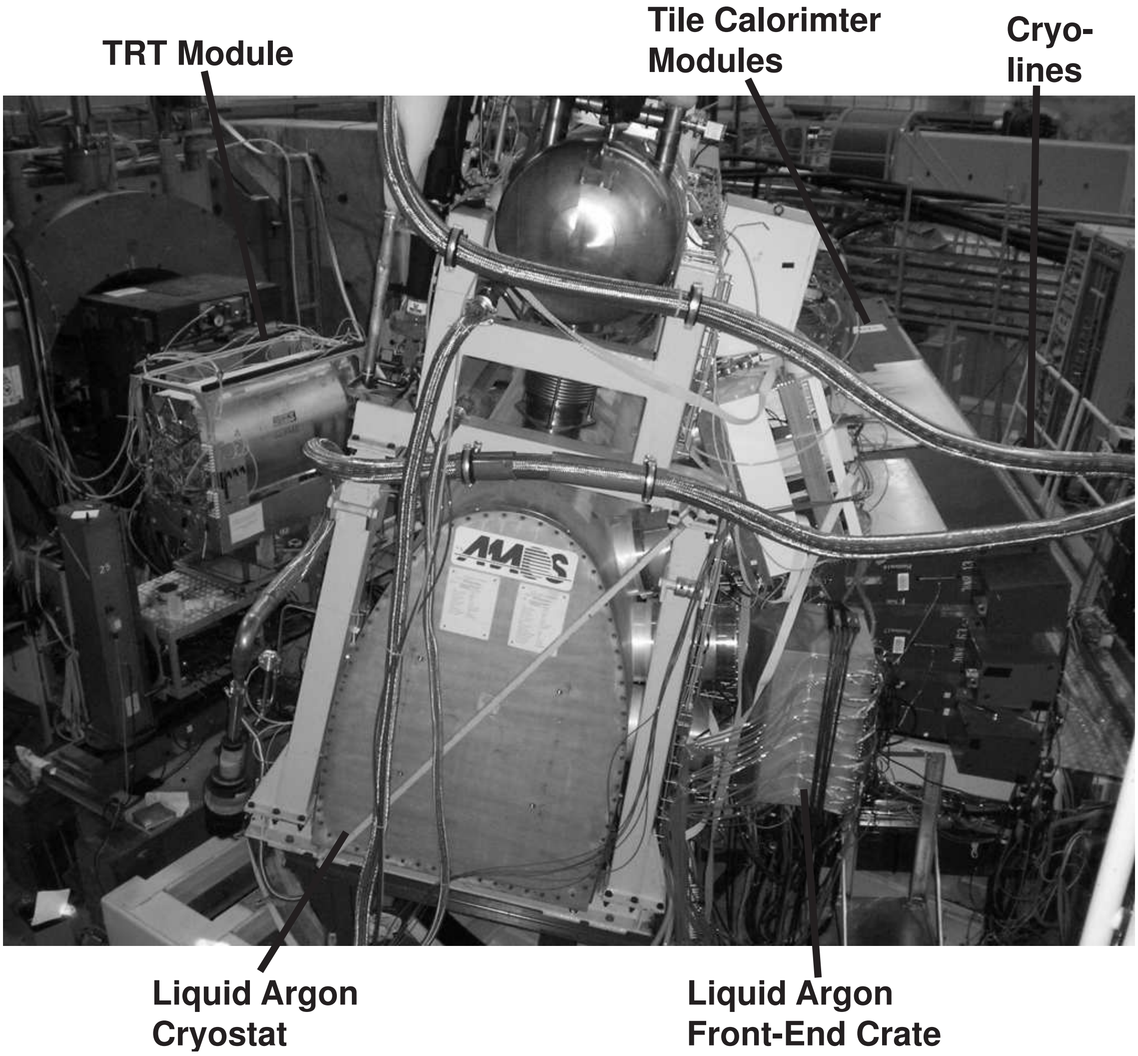

Figure 5.1: Calorimeter setup at the beam test 2004.

5.2.1 Beam test coordinate system

The origin of the beam test coordinate system is where the beam axis crosses the plane defined by the upstream face of the MBPSID magnet, close to the Morpurgo magnet. The x-axis goes along the beam line, the y-axis goes vertically upwards and the z-axis is horizontal pointing away from the Jura mountains.

5.2.2 Setup for specific studies

Extended barrel of the Tile Calorimeter

During the first month of data-taking, three modules of the Extended Barrel of the Tile Calorimeter have been placed on a separate table close to high-η side of the calorimeter table. This setup allowed us to study the Extended Barrel and the crack region between the central and the extended barrels.

Material studies

During two periods in August and in October, additional inactive material (aluminum plates) have been placed in front of the liquid argon cryostat. Thus, the effect of upstream material can be studied. Chapters 8 and 9 of this thesis are devoted to this material study.

Electrode geometry studies

Towards the end of the beam test period, a MDT chamber of the type BIS was mounted on the support structure of the liquid argon Cryostat. MDT Chambers are used in the ATLAS muon spectrometer. They are high-precision tracking devices that allow to measure the position of a traversing ionizing particle with about $50\mu m$ resolution. In our case, the MDT Chamber is used as a reference for the impact position measured by the calorimeter. In order not to compromise the precision of the muon chamber by the rather poor accuracy of the table movement the chamber has to move with the table.

Photon run

In order to investigate the performance of the calorimeter for photons a dedicated measurement was carried out. In this setup, a conversion foil of 0.2 mm lead was placed in the beam line followed by two magnets that deflect the electrons horizontally and vertically and thus displace them from the photons generated by bremsstrahlung in the conversion foil. A displacement of about 6 cm at the calorimeter was achieved. As trigger, a very small scintillator in the electron beam line was used. A second scintillator in the photon beam allows to tag converted photons.

5.3 Beam instrumentation

In addition to the detector modules, various beam instruments have been placed in the H8 beam line. The data from this elements have been recorded together with the event data to allow offline data quality control. Some of the scintillators were also used to trigger the readout. The layout of the beam instruments is shown in figure 5.2. The exact setup of the beam instruments was adapted regularly according to the needs of specific studies.

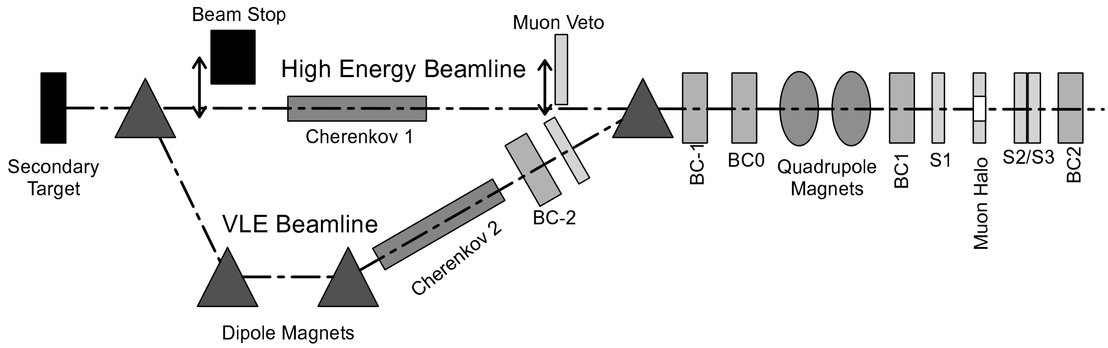

Figure 5.2: Layout of the Beam Instruments during the combined beam test. The acronyms are explained in the text.

5.3.1 List of beam instruments

Cherenkov counters

Cherenkov counters are used to distinguish pions and electrons at low energy. Three 1 m long Cherenkov detectors were installed in the H8 beam line. The first one was located far upstream (at x=-11424 mm), the two others were just before the last bending magnet. One was in the High Energy beam line, the other one in the Very Low Energy (VLE) line.

Beam chambers

Beam Chambers are used to verify the beam profile. Five delay wire chambers have been used for this purpose, called BC-2 to BC2. BC-2 was located in the VLE beamline. The two last beam chambers (placed after the last quadrupole magnet) would allow to fit a particle track but at the time of writing, this was not done.

Delay Wire Chambers are a specialization of Multi Wire Proportional Chambers [13]. They measure the impact point of a single particle using a tapped delay line connected to the cathode wires. Time-to-digital converters are connected to both sides of the delay line to measure the arrival time of the signal with respect to the anode signal. The particle position is proportional to the difference between these two TDC measurements.

The signal delay is a measure for the impact point. Each chamber consists of two such devices, orthogonal to each other to measure the position in x and y. Hence, four TDC channels are needed to read-out a beam chamber.

Scintillators

Several scintillators have been installed in the beam line. Some of them were used for trigger purposes. The signal amplitudes of the scintillators were digitized and written out together with the detector data. For some of the scintillators the signal phase with respect to the readout clock was measured as well.

Muon veto This scintillator was located in the high energy beam line and used to veto muon passing through the high energy beam stop during low energy runs.

S1 This was a big (10×10 cm) scintillator located after the last quadrupole magnet. The amplitude as well as the phase of the signal of this scintillator were measured.

Muon Halo This is also a big scintillator with a small hole in the center. It was used to veto muon outside of the beam axis.

S2 and S3 These were two small scintillators (3×3 cm) used for the trigger. They were read out by two photomultipliers. The signal phase was measured for both photomultipliers, the amplitude only for one.

Cryostat Scintillators Two large scintillators located between the liquid argon cryostat and the Tile Calorimeter.

Muon Wall This was a set of 12 scintillators behind the Tile Calorimeter.

Muon Tag This scintillator was placed behind the beam dump in order to identify muons.

Trigger and particle phase measurement

Most of the time, the main trigger was formed as coincidence of S1 and S2 and S3 vetoed by the Muon veto or Muon Halo. This trigger signal emulated the Level 1 accept that would initiate the readout of one event in ATLAS. The exact time of the readout was determined by the 40.08 MHz clock that emulates the LHC bunch crossing clock. At least for the reconstruction of Liquid-Argon-Calorimeter data, it is important to know the phase between the particle arrival and the readout clock. This phase was measured by a TDC that was started by the trigger signal and stopped by the clock.

5.3.2 Beam instrument readout

To merge the data of the beam instruments in the ATLAS byte stream, a special VME crate has been set up to emulate an ATLAS ROD crate. This beam instruments crate has been integrated with the readout of the Tile Calorimeter. This VME crate was equipped with two ADC modules, three TDC modules and a single-board computer that encodes the data into a ATLAS style ROD fragment.

The ADC modules have 8 Channels and 12 bit resolution (LeCroy 1182). One of the TDC modules was a CEAN V775 with 12 bit resolution (35 ps per step) used for the scintillators and the particle phase measurement. The beam chambers were read out by 16 bit TDC modules with 1 ns (LeCroy 1176).

The muon-wall and the cryostat scintillators were not read out via the beam instruments crate but via the so-called Tile Laser crate that is normally used for calibration runs of the Tile calorimeter.

5.3.3 Offline software for the beam instruments

On the offline side, there is a dedicated byte-stream converter to read-in the data from beam instruments, data objects representing the raw data and algorithms to treat the raw data and to fill it into the combined ntuple. This software is used for the H8 beam test as well as for the beam test that took place at the same time on the H6 beam line involving the ATLAS end-cap calorimeters and is therefore it contains functionality that is not used in H8.

The raw data objects correspond to the digitization device: There is a raw ADC and a raw TDC class. Objects of this kind are identified by names (strings) and collected in containers.

Scintillators and Cherenkov counters

Reconstruction of scintillators essentially means subtracting a pedestal and multiplying with a calibration constant to transform ADC counts into deposited energy in MeV. The phase information (if present) and the amplitude is put together in a reconstructed ADC object, labeled by a name and stored in container. The reconstruction functionality is not used in the case of H8. The signal remains as raw ADC counts.

Cherenkov counters are treated in the very same way.

Beam chambers

The Beam Profile Chamber reconstruction algorithm calculates the x and the y position on the chamber from the four TDC measurements. The necessary calibration constants are a factor that converts the time-difference between the two TDC values into a position and an offset. They are obtained using the calibration procedure described in [13] and provided to the reconstruction algorithm as job options.

5.4 Contributions of this thesis to the beam test

An important aspect of the work for this thesis was the preparation of hardware and software for the combined beam test.

In previous years, a series of liquid argon stand-alone beam tests has been performed with its own software and hardware infrastructure. Most of this infrastructure could not be used in a combined environment. The combined beam test 2004 was intended to operate with the ATLAS online and offline software framework. A lot of work was needed to add the missing elements to allow monitoring and reconstruction within the Athena framework. This code will be used for commissioning and eventually for ATLAS operation.

In particular, the following elements have been added or adapted:

- The Athena Byte Stream converter to read (and write) beam test data for physics and calibration runs as well as digitized simulated datasets. A detailed documentation about this package can be found in appendix A.
- The Athena infrastructure for beam instruments. This includes again Byte Stream converters, data objects reconstruction algorithms and ntuple creation.
- The package LArROD that does the cell energy reconstruction. Chapter 6 deals with this issue.
- The software infrastructure for electronic calibration. This includes data objects for calibration quantities as well as reconstruction and ntuple-creation algorithms.
- Software for monitoring during data taking. Monitoring was mainly done by a dedicated Athena job that run the first steps of the reconstruction chain and produced histograms.

The monitoring infrastructure was operational from the first day of data taking and was constantly adaped following the evolution of the beam test setup to provide up-to-date monitoring capabilities. Monitoring is an essential tool to assess the data quality and to give rapid feedback in case of problems. Without this monitoring system successful data-taking would not have been possible.

The entire chapters 7, 8 and 9 of this thesis are devoted to the analysis of data obtained during the material scan.

Chapter 6

Energy reconstruction of a single cell

6.1 Principle of energy reconstruction

The ADC samples of the shaped ionization signal are sent from the Front-End Board (located on the detector, outside of the cryostat) to the Read-Out Driver (located in the counting room) via an optical link. These ADC samples are the basis for the energy calculation together with calibration data acquired during dedicated calibration runs.

The ADC has a pedestal of roughly 1000 counts to accommodate the undershoot of the shaper. This pedestal has to be subtracted from the samples. The next step is to compute the peak of the ionization signal (the signal shape is shown in figure 3.7). The standard method adopted by the Liquid Argon Community is the method of optimal filtering (described in section 6.2.1). Alternatively the peak can be found by fitting second or third order polynomials to the samples. Once the amplitude of the signal is known, one has to apply the ADC to energy conversion factor. This incorporates the electronic gain, the current to energy conversion factor as well as the sampling fraction of the calorimeter. The electronic gain can also be a higher order polynomial to take small non-linearities into account.

Eventually, this first step of the energy reconstruction will be done by the Digital Signal Processors located on the Read-Out Drivers. Only under special circumstances like during commissioning, for special triggers or for cross-checks the raw ADC samples will be written out. By default, only the energy of each cell is sent to the byte stream. This is necessary in order to allow the trigger system to evaluate the energy of a region of the calorimeter in the given time budget. For further physics analysis, a more refined offline-calibration is foreseen.

During the 2004 beam test the ROD were always working in "transparent mode" (except of a very few test runs). That means they simply copied the data sent by the FEB to the byte stream. The energy reconstruction was done by the offline analysis software.

6.1.1 Offline software implementation

The Athena algorithms to calculate the energy of a single cell are located in the package `LArROD`. This name was chosen because they emulate the functionality of the hardware Read-Out Driver. These algorithms take a `LArDigitContainer` (usually read from the byte stream file) and produce a `LArRawChannelContainer` using various kinds of calibration data that come from the conditions database.

There are two algorithms available to do the step from raw ADC counts to energies. The `LArRawChannelBuilder` uses the method of Optimal Filtering. Alternatively, there is the `LArRawChannelSimpleBuilder` that is more robust and less dependent on calibration data. It is mainly intended for monitoring in a beam test environment, when no complete calibration is available.

6.2 Ionization signal reconstruction

6.2.1 The Optimal Filtering method

The method of Optimal Filtering (OF) [14] is an elegant way to compute the peak of a shaped ionization signal and at the same time minimizing the noise contribution.

The amplitude A and the time offset τ of such a signal can be computed by the formulas

$$A = \sum a_i s_i \tag{6.1}$$

$$A\tau = \sum b_i s_i \tag{6.2}$$

where a_i and b_i are the Optimal Filtering coefficients and s_i are the pedestal-subtracted ADC samples.

The time can only be calculated if the ionization signal is sufficiently above noise. The `LArRawChannelBuilder` produces this values only if the ADC peak is above a certain threshold (set by job options).

The Optimal Filtering coefficients are derived using the following ansatz for the signal

$$S(t) = A \cdot (g(t) - \tau g'(t) + n(t)) \tag{6.3}$$

where $g(t)$ is the normalized shape of the ionization signal and $g'(t)$ is it's first derivative; $n(t)$ is the noise component, taken into account by the noise autocorrelation matrix. These quantities have to be known. Since they differ from cell to cell one set of OF coefficients per cell and per shaper gain is needed.

In addition to amplitude and time offset a quality factor can be estimated by comparing the measured pulse shape with the reference shape:

$$Q = \sqrt{\sum_{i=0}^{n} \left(s_i - A \cdot (g_i - g_i'\tau)\right)^2} \tag{6.4}$$

Similar to the time offset, this value makes only sense if there is enough signal above noise.

Thanks to their simple mathematical form, equations 6.1 and 6.2 can be applied by the Digital Signal Processors of the ROD which have only limited numerical capabilities.

6.2.2 The timing problem

Equation 6.3 implies that the ionization signal and the reference signal shape used to calculate the OF coefficients are in phase up to a small deviation τ, that can be estimated by formula 6.2; if the timing is off by more than 2-3 nanoseconds the resulting amplitude will be wrong.

In ATLAS, where the bunch crossings and the readout clock are synchronous the pulses get always sampled at the same position and one set of OF coefficients is sufficient. In the test beam environment, this is not the case since the beam was asynchronous to the readout clock. Depending on the phase shift between the clock and the particle arrival, a different fraction of the pulse is sampled. To cope with this situation, multiple sets of OF coefficients have been calculated that span the region between two ADC samples in bins of approximately 1 ns. The right set of coefficients is selected using the value of the TDC that measures the phase between the master trigger and the readout clock. The current software implementation allows also a higher number of OF coefficients, if necessary.

The exact time when the ionization signal is sampled depends also on cabling delays on the signal line and trigger latencies. In the beam test setup, these values changed from time to time because of modifications to the trigger setup. To cope with this situation, time correction constants have been introduced. These constants are stored in the conditions database and have a certain interval of validity. The total time shift used to pick a set of OF-coefficients is the sum of the TDC time and the following three corrections:

Global Time Offset This number changes when the latency between the readout and the master trigger has changed.

FEB to FEB Time Offset There is one number per Front-End Board. For example, we have a significant timing difference between the two Feedthroughs (approximately 5-6 ns) due to different cable lengths.

Cell to Cell Time Offset Remaining fine time corrections between the channels of one Front-End Board.

All this numbers are added, so bigger numbers mean later pulses.

This sub-division of correction was done for practical reasons. Of course, one could introduce only a cell-based offset that incorporates all other corrections. But in this case all these numbers (3000 in the case of the beam test) would have to be changed when the global trigger latency changed.

As already mentioned, all these time offsets are necessary to match the physics signal to the reference signal that was used to calculate the OF coefficients. Hence the timing correction depends also on the way the OF coefficients have been computed.

Choosing the right set of OF coefficients

The sum of the TDC phase and all timing corrections gives a total time offset for each cell. A subset of OF coefficients has to be chosen according to this number. The ingredients to compute the OF bin number are the sampling period (the inverse of the bunch crossing frequency $1/40.08MHz \simeq 24.95ns$) and the number of OF subsets calculated within this time. The sampling period is subdivided in bins of equal width t_{bin}. We assume that the first OF coefficient is calculated at $t = 0$, so the first bin is centered around 0. So the OF coefficients cover the region of $-t_{bin}/2$ to $24.95 - t_{bin}/2$. In case of very late or very early pulses it may happen that the total time shift exceeds one of these limits. (Actually, the trigger latency of the Front-End Boards should be adjusted in a way that this never happens. But in the 2004 H8 beam test this was not always the case.)

Such event can still be reconstructed if more than five ADC samples are available or the available sets of OF Coefficients span a larger range than the sampling period. The second option implies that the fraction of the pulse used for peak reconstruction is not around the peak. The method of Optimal Filtering still allows a peak reconstruction but the signal to noise ratio deteriorates. Therefore it's better to take more ADC samples. In the 2004 H8 Beam Test, usually 6 ADC samples were taken (16 samples in H6).

The current implementation of the `LArRawChannelBuilder` assumes that we have the same number or more ADC samples than OF coefficients. The job option *InitialTime-SampleShift* tells how many leading ADC samples should be skipped. If the total time offset is found to be too large, this number in increased by one and the sampling period subtracted from the total time offset. On the other hand, if the total time offset is to small (negative), this number is decreased by one and the sampling period added to the time sample shift.

The OFC subsets are indexed in a way that a later fraction of the pulse is associated with a higher number. A pulse arriving late means that an earlier fraction of it is sampled. (The read-out clock is fixed, the particle arrival time varies.) Therefore the time shift has to be inverted $t' = 24.95 - t$.

The last step is to round the time shift to the closest integer. The procedure described above ensure that the result is always bigger than or equal to 0 and smaller than the number of OF subsets.

Iterative time-adjustment

Since the time deviation of the physics from reference signal is accessible via the OF-b-coefficients, the exact timing can be found in an iterative procedure, provided there is sufficient signal in the channel. If the ADC samples are dominated by noise, the equation 6.2 does not give a useful result.

The Athena-algorithm `LArTimeTuning` performs such iterations to obtain the corrections mentioned above. Depending on job options it calculates a global shift or time shifts per Front-End Board or for each cell.

6.2.3 Alternative methods to calculate the ADC peak

The algorithm `LArRawChannelSimpleBuilder` implements the following methods to reconstruct the ADC peak. The method can be chosen by job options.

Highest Sample Simply pick the highest ADC sample. This leads to a positive bias since the noise does not cancel out.

Fixed Sample Pick a sample which index is defined by job options.

Cubic Interpolation Interpolate a third order polynomial on 4 samples.

Parabola Fit Interpolate a second order polynomial on the 3 highest samples. For this method a phase-dependent correction can be applied. This method leads to be best results (except of Optimal Filtering).

The cubic interpolation and the parabola fit are only applied if the signal is above a certain threshold (typically 15 to 20 ADC counts). For cells below this threshold, a fixed sample is used.

6.3 Converting the signal peak to energy

The conversion factor from the peak of the ionization signal (measured in ADC counts) to the cell energy in MeV is the product of many sub-factors:

- Electronic gain (also known as *Ramp*)
- Sampling fraction
- Energy-to-current conversion factor
- Charge-Collection correction

6.3.1 Electronic gain

The relation of ADC counts to ionization current is measured on a regular basis by the electronic calibration system. This calibration procedure is described in more detail in section 6.4.3. It's output is a fit of DAC values (corresponding to a current) to ADC values. The fit can be either a straight line or a higher order polynom to take slight nonlinearities of the electronic chain into account. The DAC used has 16 bit resolution and is fed with 5 V. The ratio of DAC setting to injected current is given by

$$\frac{I_{inj}}{DAC} = \frac{5V}{(2^{16}-1)R_{inj}} \tag{6.5}$$

where R_{inj} is the injection resistor. This is a precision resistor with 0.1% accuracy.

The energy calculation in the ROD uses only a ramp obtained by a straight line fit because such a calibration can be easily undone offline to apply a more refined calibration. The `LArRawChannelBuilder` uses a ramp that is a higher-order polynom. Whether the intercept of the fit is used or not depends on the job option settings. Analysis of previous beam tests suggests that using the intercept in medium gain improves the linearity [20].

The `LArRawChannelSimpleBuilder` can use a hard-coded ramp as fall-back solution in case the electronic calibration is not available. There is one such number per gain and per layer of the calorimeter except of the middle compartment where two numbers per gain are necessary to take the changing thickness of the absorber at η 0.8 into account.

6.3.2 Sampling Fraction

The sampling faction is defined as the ratio of the total energy deposit to the energy deposit in the active regions of the calorimeter (see also equation 3.2). The number can be obtained from the Monte Carlo simulation. The beam test simulation yields a sampling fraction of 0.18 for η <0.8 and 0.212 for η >0.8 for the electromagnetic barrel calorimeter. More details about the sampling fraction including plots can be found in section 8.2.

6.3.3 Current to energy conversion factor

In the straight sections of the accordion folds, where the electric field is simple and homogeneous the conversion factor from energy deposit to the induced current can be easily calculated from the drift time and the average energy needed to create a single electron/ion pair. For argon, this corresponds to W=23.6 eV per e^-/ion-pair [2]. An energy deposit of one eV frees electrons with a total charge of e/W and the same amount of ions (e is the elementary charge). The ions drift very slowly inducing a small current that is neglected in the following calculation. The electrons drift quickly and induce a current at the signal electrode. As the electrons get absorbed at the anode, the current decreases. This leads to the triangular shape of the signal.

The peak current is induced by the charge of all the electrons drifting with the velocity v over the distance d. The peak current per deposited charge q is given by:

$$I = \frac{q \cdot v}{d} \tag{6.6}$$

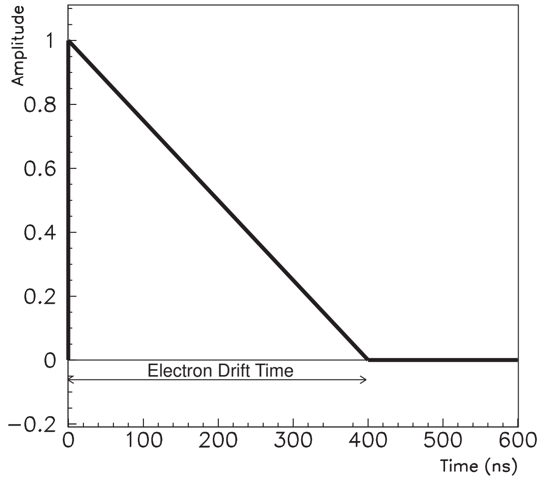

Figure 6.1: Signal induced by the drifting electrodes in the liquid argon gap.

Region	Gap width	v [m/s]	I/E [nA/MeV]
Presampler	2.0 mm	4593	15.6
Accordion	2.12 mm	4508	14.4

Table 6.1: Drift velocity and I/E factor for presampler and accordion

Since the drift time is determined by the gap width and the velocity $t_d = \frac{d}{v}$ and the charge per deposited eV is given by $q/E = e/W$, equation 6.6 can be transformed into

$$\frac{I}{E} = \frac{e}{W \cdot t_d} \tag{6.7}$$

The drift velocity v depends on the electric field and the temperature of the argon. In a very high electric field the velocity is no longer proportional to the field strength. During the design phase of the calorimeter, a detailed measurement of the electron drift velocity in argon in the relevant temperature and electric field range has been performed. The measured data can be described by an empirical formula [15]. Assuming a constant temperature, the drift velocity is roughly proportional to $E^{0.3}$ (see figure 6.2).

Equation 6.7 can be understood intuitively: the area under the triangular ionization signal shown in figure 6.1 corresponds to half of the total charge e/W. The other half is carried by ions that induce also a triangular current signal but with a very long drift time and a very small current. Therefore one can compare this area with the total charge: $\frac{e}{2W} = \frac{I \cdot t_d}{2}$.

The values yielded by the equations given above at nominal temperature (89.3 K), gap-width and high voltage (2 kV) are summarized in table 6.1.

These numbers are only valid for the straight section of the accordion, where the electric field is homogeneous and recombination is neglected.

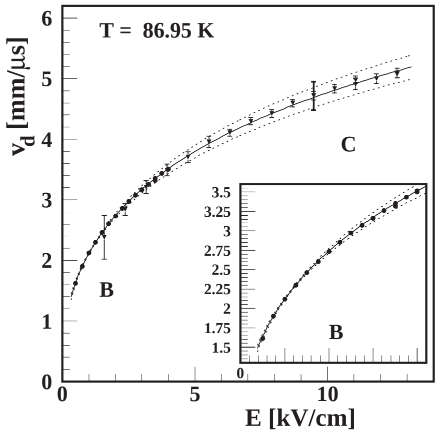

Figure 6.2: Drift velocity of electrons in liquid argon as function of the electrical field strength at a temerpature of 86.95 K. Plot taken from [15].

The Geant4 simulation of the Liquid Argon Calorimeter includes a detailed description of the electrical field and charge-collection in the folds of the accordion. This description is implemented in a way that it gives the ratio between a certain point in the fold region to the nominal value in the straight region. The simulation shows that the average I/E factor is about 7% lower than the one calculated for the straight sections (see also section 8.4).

Alternatively, the I/E factor can be derived by comparing the energy deposit predicted by the Monte-Carlo simulation with the current measured in the beam test, assuming that all other effects are properly described in the simulation. Such a comparison was carried out with beam test data from 2002 (where the beam energy was precisely known) and yielded a value of 16 nA/MeV [24].

There is still some uncertainty about the I/E factor and thus the absolute calibration of the accordion calorimeter. The final verification of this value will be based on physics data, mainly by exploiting the precise knowledge of the mass of the Z^0 boson.

6.3.4 Cross talk

The readout signal of the calorimeter cells is affected by mostly capacitive cross-talk. Detailed measurements have been performed during previous beam tests [22] and a cross talk map (see figure 6.3) has been produced. The biggest cross-talk (about 7%) can be observed between neighbouring strip cells.

Cross-talk has two major effects on the readout signal: first, a fraction of the energy of a cell is spread out to its neighbors and second, the pulse shape is distorted. Since neighboring cells will be most likely contained in the same cluster, the loss of signal to the neighbors does not change the cluster energy significantly. But the situation for calibration runs is

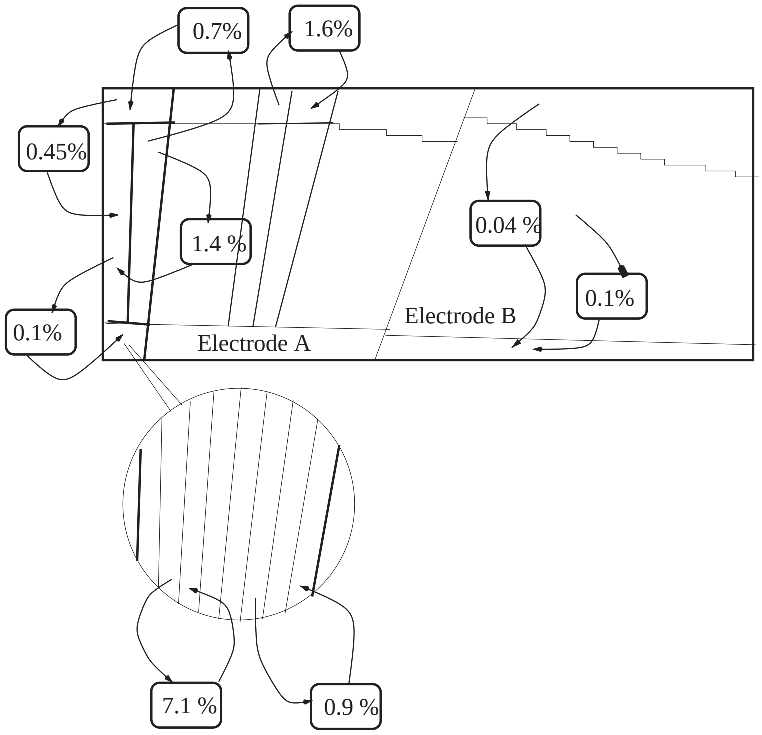

Figure 6.3: Cross talk measured in module M13

much different: Here, every cell is pulsed individually independently from its neighbors so signal gets lost to the neighbors and the reconstructed calibration pulse peak is lower. This effect is relevant in the strips and has to be corrected.

6.4 Electronics calibration procedure

6.4.1 Principle

Some of the calibration constants mentioned above depend on the properties of the electronic readout chain and may vary with time. These constants are obtained by dedicated calibration runs using the electronic calibration system described in section 3.4. In general, the values are different for each cell and each gain and have to be measured individually for each cell and each gain. To avoid the influence of cross-talk, neighboring cells are not pulsed at the same time.

6.4.2 Pedestal

The pedestal is the ADC counts of an idle channel. This corresponds to roughly 1000 ADC counts to accommodate the undershoot of the shaper. The pedestal depends slightly on the temperature of the FEB (1 ADC count per 6°C where observed during the beam test). During data taking, it's planned to measure the pedestal every 8 hours. This was also done during the beam test 2004. One pedestal runs consists of about 2000 events in each gain. The pedestal used in the reconstruction is obtained by averaging over all events and all ADC samples for each channel and each gain. At the same time, the electronic noise and the noise autocorrelation matrix can be calculated. The noise autocorrelation is an input parameter for the Optimal Filtering computation and the noise level is used for clustering.

Alternatively, the pedestal can be computed on random events[1], provided they are available. This was done for some periods of the beam test to avoid problems due to changing FEB temperature.

6.4.3 Electronic gain

The electronic gain relates the ionization current to ADC counts. The calibration system of the calorimeter allows to send well-defined pulses of different amplitudes through the electronics chain. The amplitude of this calibration pulse is given by the input to the Digital-Analog converter (DAC). Thus the current to ADC calibration can be measured in-situ at any time. In so-called Ramp-runs, the cells of the calorimeter are pulsed with increasing DAC values. For each point, about 100 events are recorded. Similar to the pedestal runs such measurements will be carried out every 8 hours. Figure 6.4 shows an example of a ramp in a middle cell. Experience of the beam test shows that the gain changes by about 1% per 4° FEB temperature change.

To analyze a ramp run, one needs to find the pulse peak of the calibration signal. Similar to the physics pulse shape, the easiest but least accurate method is to fit a parabola to the highest samples. It is more accurate to use the knowledge of the calibration pulse shape (that is evaluated by delay runs) and fit the amplitude and the time of the ramp pulse to the delay pulse. The actual ramp is now the correlation between the pulse peak in ADC counts and the input DAC value that corresponds to an electrical current. It can be fitted either as a straight line or as a higher-order polynomial function.

6.4.4 Pulse shape

The most complicated calibration runs are so-called delay runs. Their purpose is to acquire the shape of the signal necessary to calculate the optimal filtering coefficients. This is done by pulsing the channels using the calibration system and delaying the readout in steps of ~ 1 ns. Since the ADC samples spaced in intervals of 25 ns, 25 delay steps are necessary

[1]Random event means that the readout was triggered independent of partices crossing the detector.

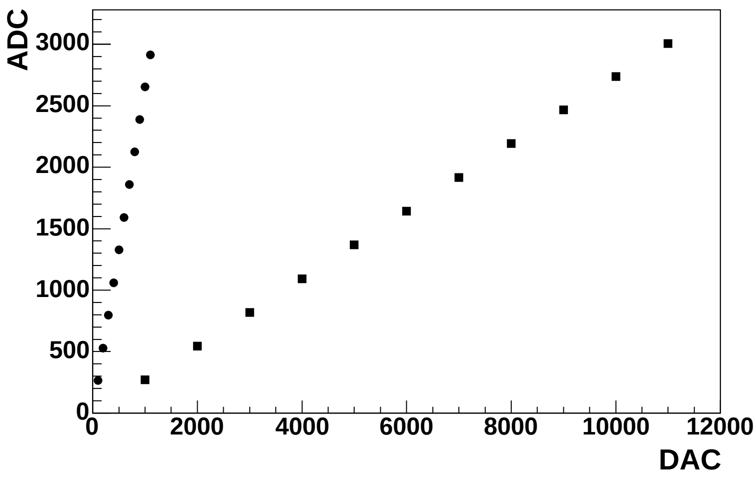

Figure 6.4: Example for ramps in high gain (circles) and medium gain (squares) in a cell of the middle compartment.

to cover the signal shape in steps of 1ns. The number of acquired ADC samples defines the fraction of the shape that is sampled. If only 5 ADC samples are recorded (like for physics data), the first 125 ns are covered. This corresponds to the fraction of the pulse that is used for physics runs. In order to record also the exponential tail of the signal, longer delay runs are necessary. The Front-End electronics allows for runs up to 32 samples (800 ns). During the beam test 2004, only 27 sample delay runs (675 ns) have been taken.

As already mentioned, the calibration pulse shape and the ionization pulse shape are not identical. The ionization pulse is triangular whereas the calibration pulse is the exponential decay current of a inductance. The second difference is that the physics signal and the calibration signal are not injected at the same point. The difference can be corrected mathematically using the electrical properties of the readout line [21], or by fitting a physics pulse profile to a calibration pulse profile. Figure 6.5 shows an example of a calibration signal shape and the corresponding predicted physics pulse shape.

The difference between calibration and physics pulse shape leads also to slightly different peak heights. The factor between physics and calibration pulse height became known as M_{phys}/M_{cal} factor. It is one of the results of the physics pulse prediction procedure. Since the ramp is taken on a calibration pulse, it is systematically wrong by this factor and has to be corrected.

6.4.5 Software implementation

The data acquired during calibration runs is written to ordinary byte-stream files like a physics run. The software to read and analyze calibration runs is also part of the Athena

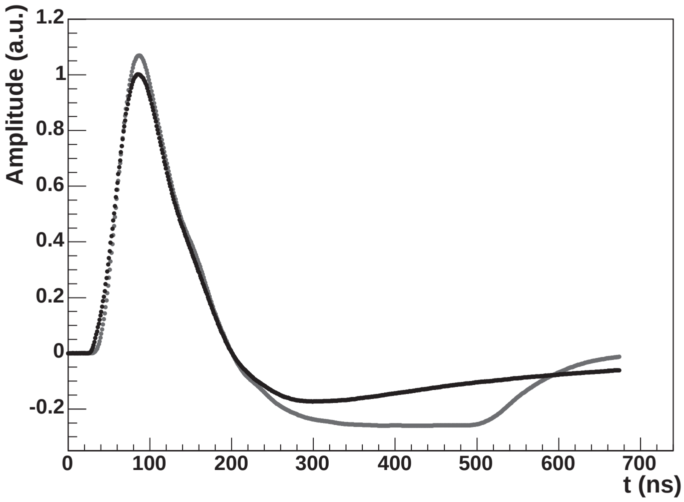

Figure 6.5: Example for a calibration pulse shape (black) and the predicted physics pulse shape (grey) for a middle cell.

framework. There are four packages devoted to electronic calibration of the Liquid Argon Calorimeter: LArElecCalib contains abstract interfaces to the calibration data objects, LArRawConditions holds the data objects itself, LArCalibUtils consists of algorithms for calibration run analysis and LArCalibTools contains algorithms that produces ROOT ntuples of calibration objects and intermediate objects. In general, the result of a calibration run analysis is written to a database from where it can be retrieved for subsequent physics run analysis.

The first step of calibration run analysis is to average over the events with the same DAC and delay settings (usually 100 events). For final ATLAS it is foreseen to do this step at the Digital Signal Processor on the ROD and thus decrease the file size and save offline computing power. Then the data gets organized by channel and gain, that means all points of the ramp or delay profile of a certain cell are gathered. In the finalize-method of the calibration algorithms, after all events of a calibration run have been read in, the actual processing of the individual channels takes place. In case of the delay run analysis, that is a complicated and lengthy process, intermediate results like calibration waveform or waveform parameters are written to the database so that partial reprocessing is possible. In this case, no event data is read in.

Container class for calibration objects

Most of the calibration data as well as intermediate results are valid for a certain cell and gain. In terms of software, there is one calibration data object per cell and gain. An efficient way to store and access these object is needed. Therefore a dedicated container object was designed, the LArConditionContainer. It takes advantage of the read-out structure of the calorimeters: each Front-End board has 128 channels (although some might not be connected) and the identifier of a readout channel can be easily broken down into a FEB identifier and a channel number. Internally the LArConditionContainer stores the data in STL[2] vectors of fixed size 128, one for each FEB. The vectors themselves are stored in a STL map with the FEB identifier as key. The container provides functions for random-access as well as STL-like iterators. This solution is flexible enough for beam test and commissioning where the number of installed Front-End boards can change at almost any time.

Most of the foreseen applications of the LArRawChannelContainer process data FEB-wise. For instance, raw data in the Byte Stream is stored in FEB blocks and read in this way. To further improve the performance of the LArConditionContainer the current FEB is cached and the binary search in the map of FEBs takes place only if a channel of a new FEB is requested. There are also use-cases where an object in a LArConditionContainer has to be accessed by its offline identifier. (Offline identifier encodes the geometrical position of a cell in the detector, online identifier encodes the readout line, see also section 4.2.1). A special function allows efficient access by an offline identifier. It uses a vector containing pointers to the elements and is indexed by the offline identifier hash.

6.5 Summary and contributions of this thesis

The electronics calibration of the Liquid Argon Calorimter is now well understood and the necessary offline software has been implemented as part of this thesis. The reconstruction software is now ready for data analysis, the energy in a cell can be reconstructed with an accuracy of a few MeV.

The software is now also capable of extracting calibration constants from calibration runs (Pedestal, Ramp, Delay-Profile) and write them to a data base for subsequent use on physics runs. This procedure has been exercised during the combined beam test. Since then various modifications and improvements of the code took place. Nonetheless, the reconstruction software was available for beam test reconstrucion at any time. Several large-scale reconstruction campaigns where millions of beam test events have been resonstructed were sucessfully carried out.

The reconstruction and calibration software has been carefully designed to work not only for a small number of channels as in the beam test but also for final ATLAS where we have 200 000 channels. The calibration code is currently used to analyse the first calibration data taken during the commissioning of the barrel calorimeter.

[2]STL stand for Standard Template Library, a C++ library heavily used in ATLAS software.

Chapter 7

Monte-Carlo simulation of the beam test setup

Monte-Carlo simulation is a very important tool to derive the corrections needed to optimize the energy measurement. Most of the results presented in this thesis have been produced with the Geant4 based simulation of electrons in the setup of the combined beam test. The reconstruction of beam test data and simulated beam test events is almost identical. There are only two significant differences. First, the asynchronous particle arrival is not simulated, the particles are always in phase with the readout clock. Therefore only one set of Optimal Filtering Coefficients is needed. Second, the digitized file contains already energy in MeV in contrast to raw ADC samples in case of real data files. The LArRawChannelBuilder algorithm is already invoked at the digitization step.

7.1 Monte-Carlo - Data comparison

7.1.1 Modifications of the beam line description

Comparions of data to simulation carried out with various beam test setups (for example the one of the 2002 Liquid Argon Calorimeter beam test) showed that the Geant4 simulation is in principle able to describe electromagnetic showers with astonishing accuracy. One of the lessons learned from 2002 was that the precise knowledge of the material in the beam upstream of the calorimeter is crucial. To judge if the amount of upstream material is properly described, the energy sharing between the different compartments of the calorimeter in data and simulation has been compared. The right setup should give a correct description for all energies and all material configurations.

The absolute value of the energy deposit is not necessarily comparable, since it includes effects that are not simulated like recombination in the liquid argon. Therefore the relative energy in each compartment E_i/E_{Acc} has been used.

Initially, the simulation of the 2004 beam test showed significantly less energy in the front compartment and more energy in the middle compartment than in the data suggesting more upstream material than simulated. After consulting the log-book and detailed drawings of the beam-line, material equivalent to about 15% of a radiation length could be identified far upstream. It is composed mainly of Mylar windows of vacuum tubes and air between the tubes. This material was not accounted for because the simulation of the beamline starts only 30 m upstream of the calorimeter while the energy-defining spectrometer is in reality about 400 m upstream.

Another 'forgotten' piece of material was identified inside the cryostat. As already mentionned in section 5.2, a block of Rohacell was used to displace liquid argon in the cryostat upstream of the presampler. Figure 7.1 shows a photo of the situation in the cyrostat. It appears now that a small quantity of argon diffuses in the Rohacell. Such a problem has already been seen in the 2002 beam test. Currently, masurements are being done to determine the absorption of liquid argon by Rohacell. At the time of writing, the results of these measurements were not yet available.

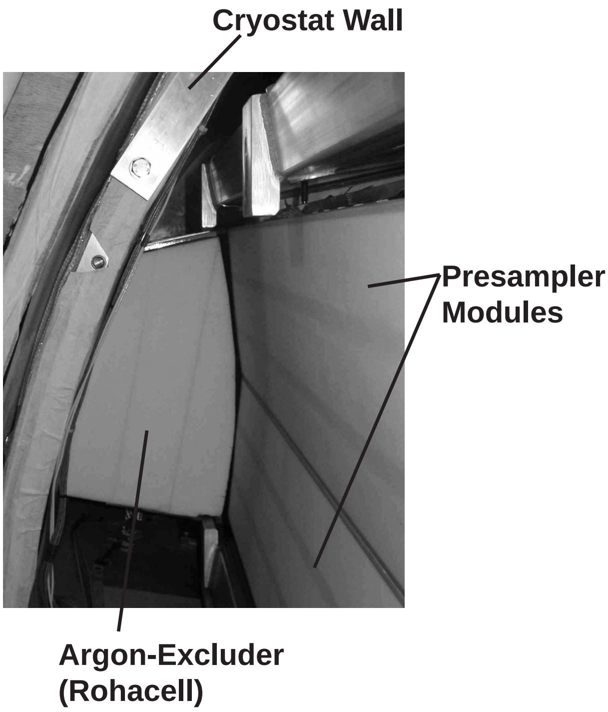

Figure 7.1: Photo of the Argon-Excluder in the beam test cryostat taken just before the cryostat was closed.

For the simulation used for the analysis described in this thesis, these two pieces of missing material have been described by 'equivalent' material: One 13.35 mm thick block of Aluminium at position x=-20 m and one aluminium block of 15 mm thickness just upstream of the cryostat. This block rotates with the cryostat, so the thickness seen by the particle is 16.1 mm or 18% of a radiation length at a pseudorapidity of η=0.4.

7.1.2 Corrections for simulation comparison

To account for the uncertainty of the absolute energy scale, we allow for two adjustable correction factors to scale the accordion energy and the presampler energy to match the simulation. These factors must be identical for all beam energies and all material configurations. For a comparison, the absolute energy scale can be taken out by looking at the energy of each compartment divided by the total accordion energy.

Cross-talk changes the scale of the energy measurement in the strips compartment. The electronic calibration signal is lowered due to signal loss towards the neighbouring cells and thus an overestimation of the physics signal (see section 6.3.4). This effect is not simulated. To account for it, the energy in the strips is scaled down by 7% in the data. The effect of signal being spread out to neigbouring cells by cross-talk is simulated.

The energy deposit in the presampler needs to be rescaled as well. The reason is that the argon-filled gap is 13 mm wide, but the electric field actually covers only 11 mm. In the simulation, the full gap width is regarded as active region. Therefore, the simulated energy deposit in the presampler has to be weighted with a factor 11/13.

Figure 7.2 shows the relative energy distribution of the presampler and each layer of the accordion calorimeter for a 20 GeV electron beam after applying these two corrections, but without any scale factors. As one can see, the agreement for the three compartments of the accordion in terms of relative energy deposits (normalized to the accordion energy deposit) is more than satisfactory. The deviation of the mean value for strips and middle compartment is less than 0.1% and also the tails of the distributions are well described. On the other hand, the simulated energy deposit in the presampler is about 22% too high. A possible explanation for this large discrepancy is that the beam hits a boundary between two presampler modules (at ϕ=0). The small gap between the module is not correctly simulated (stray field).

At the given beam energy, the deposit in the back sampling is very small. The good agreement indicates that the noise is correctly simulated and the pedestal values are accurate.

The absolute values of the energy deposit deviate by about 2%. The best match of data to simulation can be achieved by re-scaling the presampler by a factor 0.8 and the accordion by 0.98. As already mentionned, such factors are justified because of the uncertainty on the absolute energy scale. The ratios of the measured and the simulated energy deposit in the accordion calorimeter are summarized in figure 7.4. The RMS of all points (6 beam energies and 4 material configurations) is 0.75%.

Figure 7.3 shows the ratio of simulated and real energy deposit in each compartment of the calorimeter. The ratios for the front and the middle compartment are within 2% for most of the points. The deviation of the presampler and the back compartment is larger especially for low energy runs. The simulation is expected to improve further as soon as the detailed simulation of beam line is in place and with a better understanding of the argon penetration of the Rohacell block and an improved simulation of the presampler geometry.

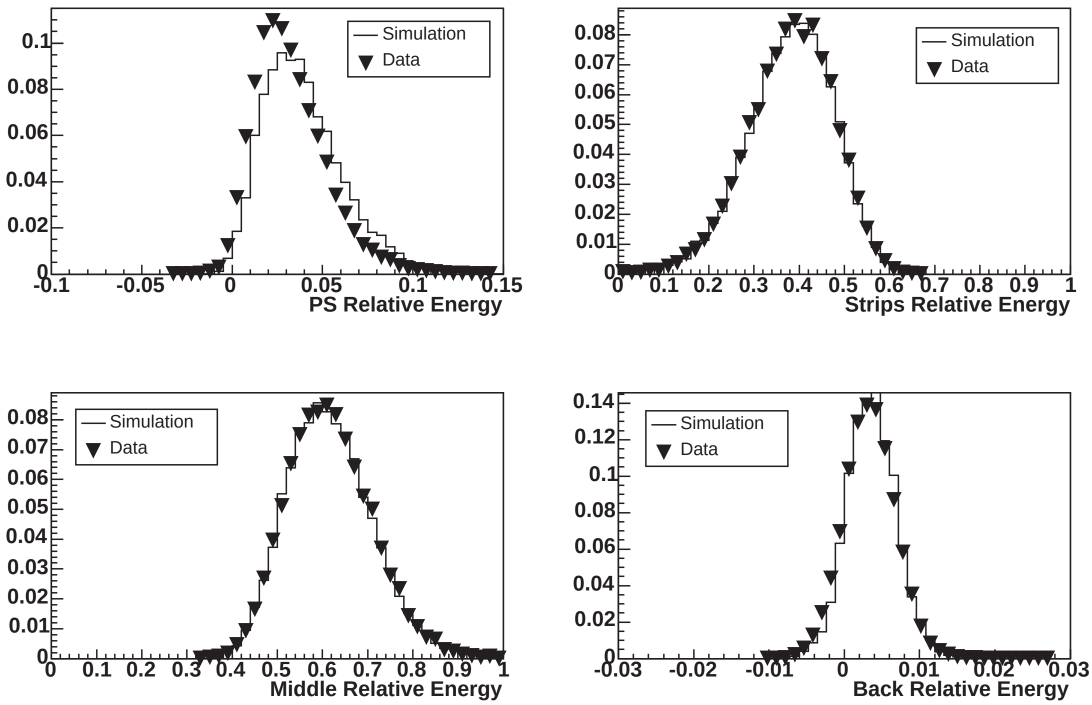

Figure 7.2: Energy deposit in each compartment of the calorimeter for data and simulation for 20 GeV electrons. Shown is the ratio of energy deposit in the compartment to the total energy deposit in the accordion.

It is clearly visible that the agreement of presampler energy deposit is much worse than for the accordion. As said before, one probable explanation is that the beam was impinging at boundary between two presampler module. Figure 7.5 shows the dependence of the measured energy deposits in the presampler and the middle compartment on the impact point for data and simulation without any scale factors. Also in this case one sees that the agreement for the accordion is fine (except at the boundaries) while the presampler shows a significant deviation. In particular the plot of the presampler energy versus ϕ shows that the dip that corresponds to the gap between the two modules is shifted. This comes from a known inaccuracy of the simulation geometry: the presampler modules are shifted by a quarter of a middle cell.

Furthermore, the complicated shape of the electric field in the gap between the two modules is not simulated. Since the exact ϕ impact point is sightly different for each energy point, the fraction of the beam hitting this regions differs as well. Thus the presampler response changes in a way that is not correctly described by the simulation.

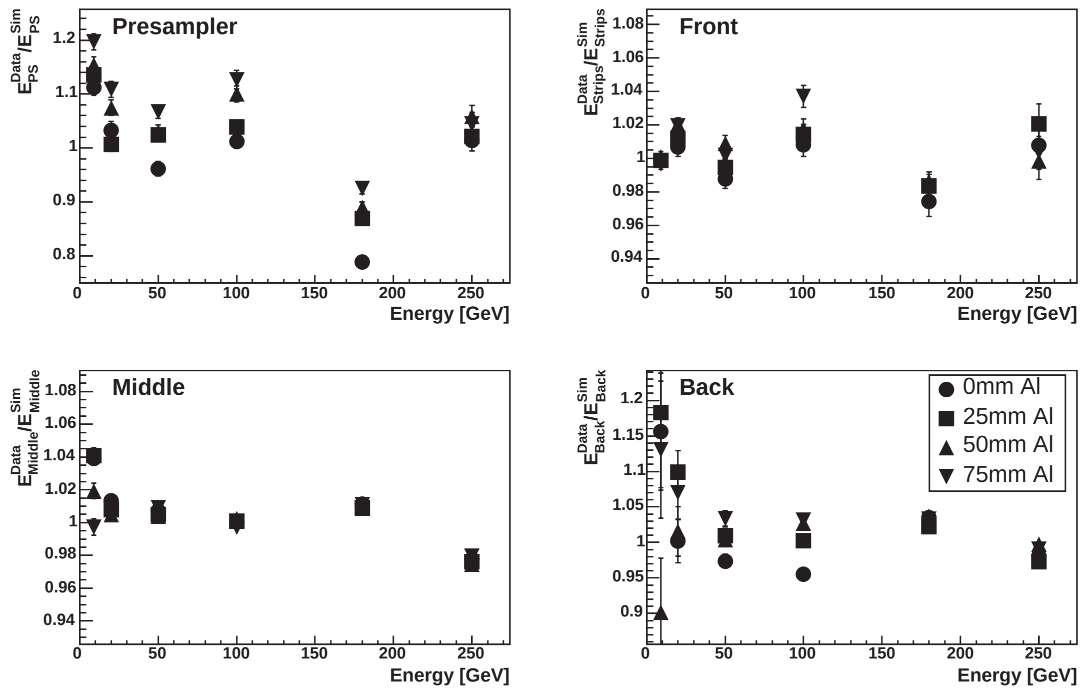

Figure 7.3: Ratios of the mean energy deposit in each compartment of the accordion calorimeter and the presampler measured in the beam test to the mean energy deposit obtained by simulation.

7.2 Summary and contributions from this thesis

The comparison of simulation and data obtained from the 2004 combined beam test which was done for this thesis provided essential feedback to the ATLAS Simulation group which lead eventually to a realistic Monte-Carlo simulation. It turned out that the correct description of the geometry and in particular of the material upstream of the calorimter is essential. By now, the comparison yields a good agreement of data and simulation.

This allows to use the simulation as basis for the optimization of the energy measurement. It is possible to correct effect-by-effect all uncertainties that influence the performance. This will be shown in the next chapter.

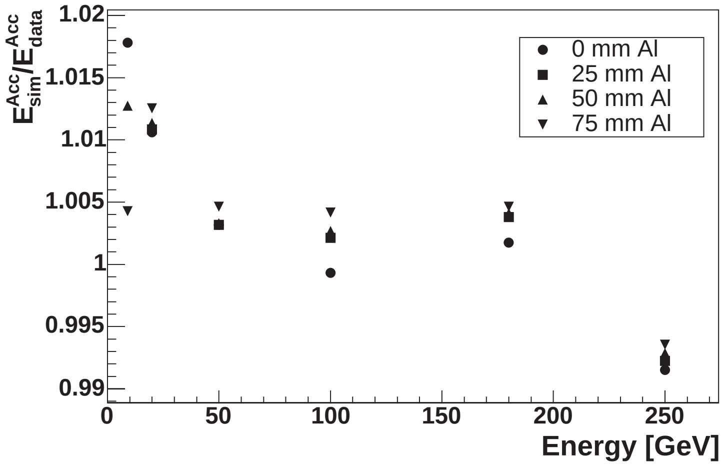

Figure 7.4: Ratio of the mean accordion energy deposit measured in the beam test to the one obtained by simulation. The correction factors explained in the text have been applied.

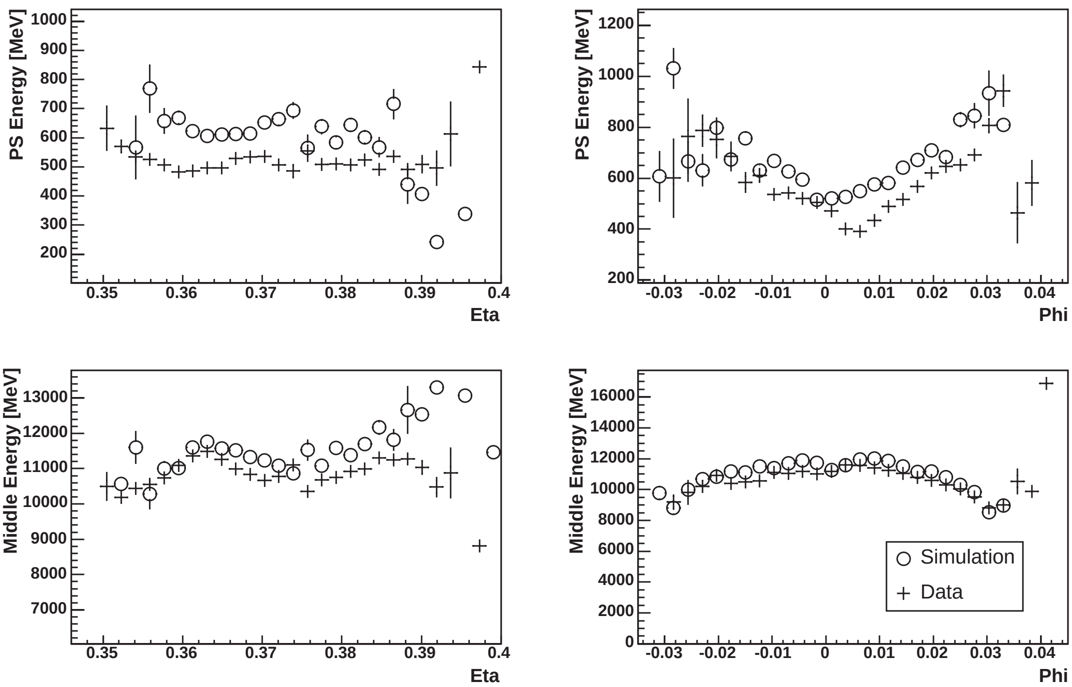

Figure 7.5: Measured energy deposit in the presampler and the middle Compartment versus η and ϕ for 20 GeV electrons.

Chapter 8

Optimizing the energy measurement

8.1 Introduction

The energy sum of all cells in an electromagnetic cluster is the first raw measurement of the particle energy. At this point a resolution of about $14\%/\sqrt{E}$ and a linearity of 15% is achievable. Further corrections, described in the following sections, are necessary to achieve the required performance. But since the particle energy is already roughly known, all further corrections may be energy dependent unless the energy dependence is too strong.

As already mentioned, the absolute energy calibration will be based on reference reactions like the decay of Z^0 into an e^+e^- pair. To be able to calibrate the energy scale with the known Z-mass and to extrapolate to other energies, excellent linearity is required.

Correcting the accordion energy

In order to transform the measured energy in a cluster into the total accordion energy deposit one has to take into account the following effects:

- Sampling fraction (or correction to the sampling fraction)
- Out of cluster correction
- Effect of the non-homogeneous electrical field in the accordion folds

All these corrections have a dependence on the beam energy and on the impact point. The exact sampling fraction and the effect of the electric field in the accordion folds changes with ϕ because of the complex absorber/electrode structure of the accordion calorimeter. The fraction of the energy outside the cluster depends on the distance of the impact point to the center of the seed cell.

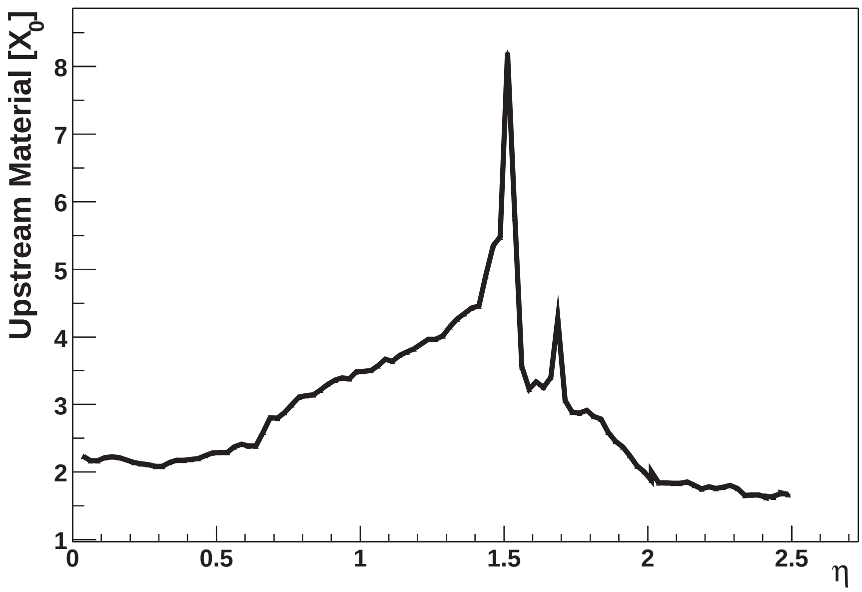

Figure 8.1: Amount of material upstream of the accordion calorimeter measured in radiation length as function of pseudo-rapidity.

The effect of upstream material

In a detector setup like the one in ATLAS, a certain amount of material upstream of the electromagnetic calorimeter is unavoidable. The largest contributor is the double-wall aluminum cryostat that contains the liquid argon with a thickness of about 1.4 X_0 in the barrel region. The thickness seen by the particle increases with rapidity, since it crosses the cryostat at a larger angle. In the crack region between the barrel and the end-cap, the total upstream material increases even more. The beam pipe and the Inner Detector are made of low-density and low-Z materials. In the barrel region they amount to about 0.3 radiation lengths (X_0). Figure 8.1 shows the amount of material upstream of the accordion calorimeter as a function of η for the ATLAS detector. [23].

The ATLAS EM calorimeter is equipped with a presampler (described in section 3.2.2) in order to correct for the energy lost in the upstream material. Between the presampler and the accordion calorimeter is another inactive region that is 6 to 10 cm thick. Its thickness varies since flat presampler modules are mounted on the round inner bore of the barrel accordion calorimeter. This space contains the G10 bars that hold the absorbers as well as the cables, the summing boards and mother boards for the front compartment of the accordion. In terms of radiation length, this region amounts to about 0.5 X_0. Since it is further upstream and the shower is more developed the energy deposit in this gap region between presampler and accordion is more important than the one upstream of

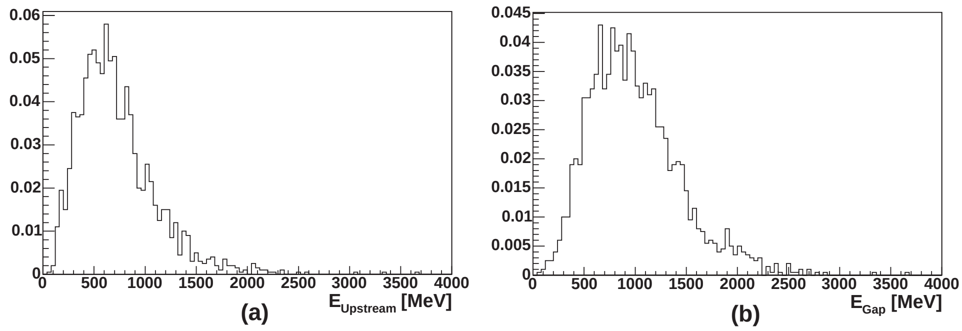

Figure 8.2: (a) Energy deposit upstream of the presampler and (b) energy deposit in the gap between presampler and accordion calorimeter.

the presampler. Figure 8.2 shows the energy deposit in these two regions obtained from the beam test Monte Carlo simulation for 100 GeV electrons at η=0.367 and ϕ=0. In this setup, there are 1.77 X_0 upstream of the active layer of the presampler and 0.46 X_0 between the presampler and the accordion. This plot shows that the energy lost in these two regions is of the order of 2 GeV, 2% of the energy of a 100 GeV electron.

Figure 8.3 summarizes the energy deposit in the various regions for several beam energies and upstream material configurations.

Only the accordion energy deposit is measured directly. The energy lost in the other regions has to be estimated using the energy measurement from the accordion compartments and from the presampler. One can see that the upstream energy loss is dominant. For many points it is about one order of magnitude bigger than the back leakage. In general, lower beam energies are more affected by inactive regions.

Until about two years ago, the ATLAS Liquid Argon collaboration planned to use a simple layer-weighting technique to achieve the required linearity and resolution. The weights were derived from beam test data by minimizing the resolution. Various studies showed that such a method does achieve a good resolution, but cannot give a good linearity and resolution at the same time. Over the last two years, an alternative was developed that is presented in the following sections of this thesis. A dedicated linearity study with a specially instrumented beam line during the 2002 beam test run and a material scan during the 2004 beam test where carried out to validate this method. By changing the material in front of the cyrostat in a controlled way one can mimic the situation in the ATLAS detector where the amount of material changes with η.

8.2 Sampling Fraction

One important quantity that must be obtained from the simulation is the exact sampling fraction. Figure 8.4 shows the sampling fraction for 1000 electrons of 100 GeV at η=0.4

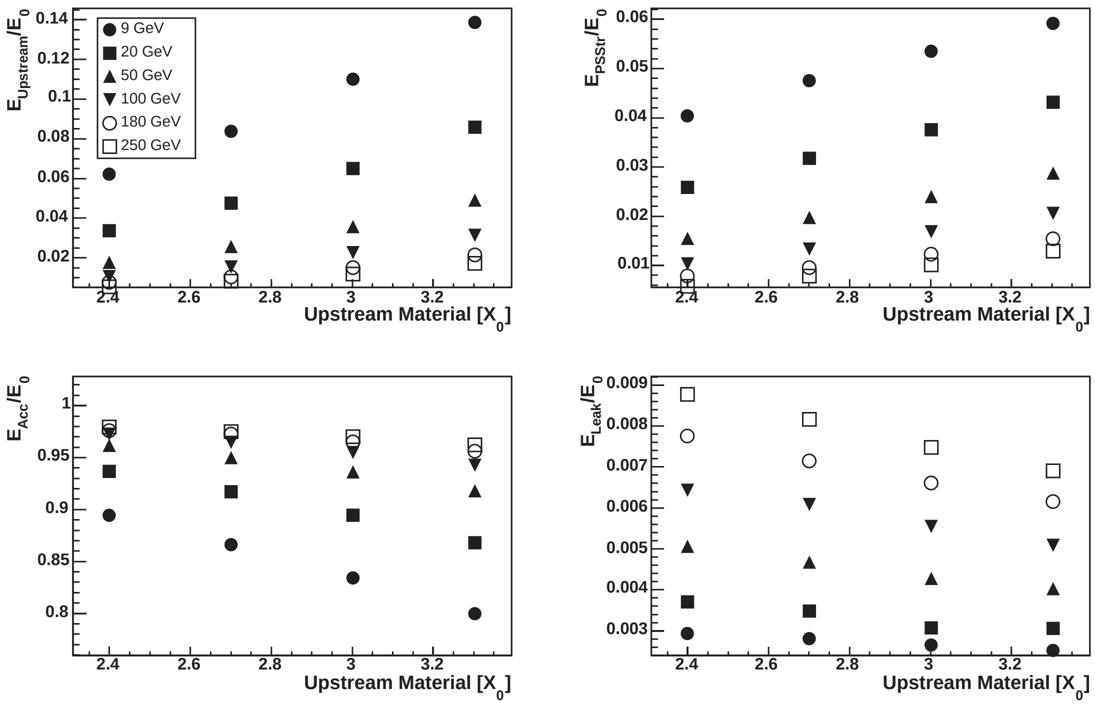

Figure 8.3: Mean fractional energy deposit upstream of the presampler, in the gap between presampler and accordion, the accordion and back leakage for different energies and upstream material thickness.

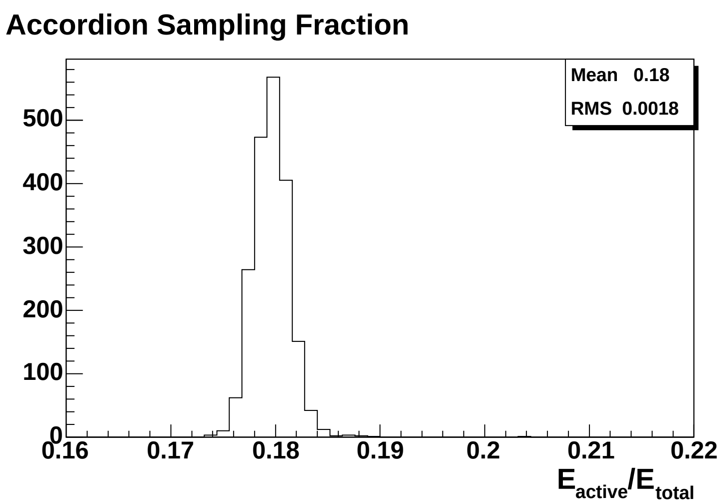

Figure 8.4: Accordion sampling fraction for 1000 electrons of 100 GeV impinging at η=0.4 and ϕ=0.

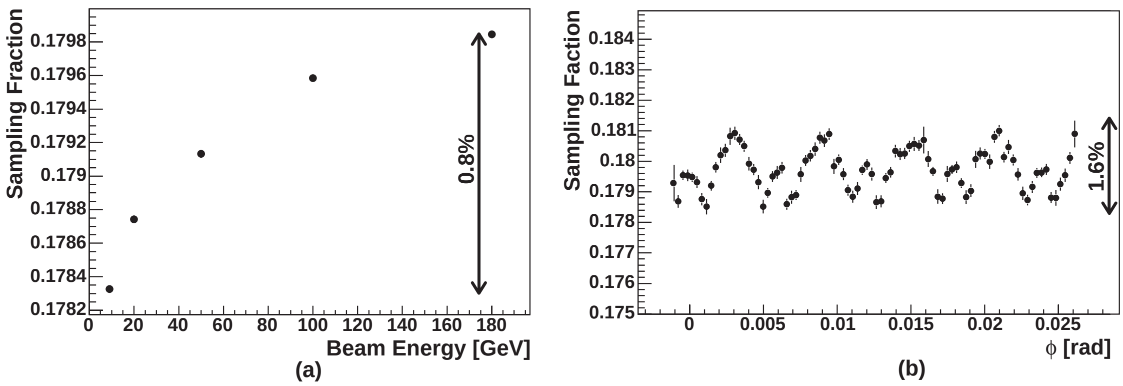

Figure 8.5: (a) Accordion sampling fraction for various beam energies obtained from the beam test simulation with electrons at $\eta = 0.37$ and $\phi = 0$. (b) Sampling fraction versus the ϕ-impact point. This plot was made by varying the direction of the particle at the primary vertex in the beam test simulation. The range corresponds roughly to one middle cell width.

and ϕ=0 obtained from the beam test simulation. The shown quantity is the energy deposit in the active region of the accordion divided by the total energy deposit (active plus passive) in the accordion. A Gaussian fit of the distribution yields a mean value of 0.1796 and a sigma of 0.0017. As already pointed out in section 3.1.2, the sampling fraction is the fraction of the shower that is sampled in the active regions of the calorimeter. Therefore, it fluctuates as the shower fluctuates.

The sampling fraction at η >0.8 is higher because of the lower lead-fraction in this region. A similar simulation yields a mean value of 0.2118.

The dependency of the accordion sampling fraction on the beam energy and on the impact point is plotted in figure 8.5.

In reality, the sampling fraction is not constant within the shower. It is interesting to look at the dependency of the sampling fraction on the position in the shower. Figure 8.6 shows the sampling fraction along the axis of the shower, as well as versus the distance (radius) to the beam axis. For electrons, one can see a clear decrease of the sampling fraction towards bigger radii and depth. Muons in constrast, have a constant sampling fraction since they do not induce a shower. Figure 8.6 (b) features a peak of the sampling fraction at r $\sim$ 12 mm. This does not affect the calibration of the calorimeter, since this is smaller than the middle cell size.

The decrease of the electron sampling fraction can be explained by the fact that the tail of the shower contains many low-energy particles that have a higher probability to get absorbed in the lead than in the argon gap. Nevertheless, the sampling fraction used for the reconstruction must not be compartment dependent. The length of an electromagnetic shower depends on the energy of the impinging particle and is subject to significant statistical fluctuations. So applying a non-uniform sampling fraction would compromise

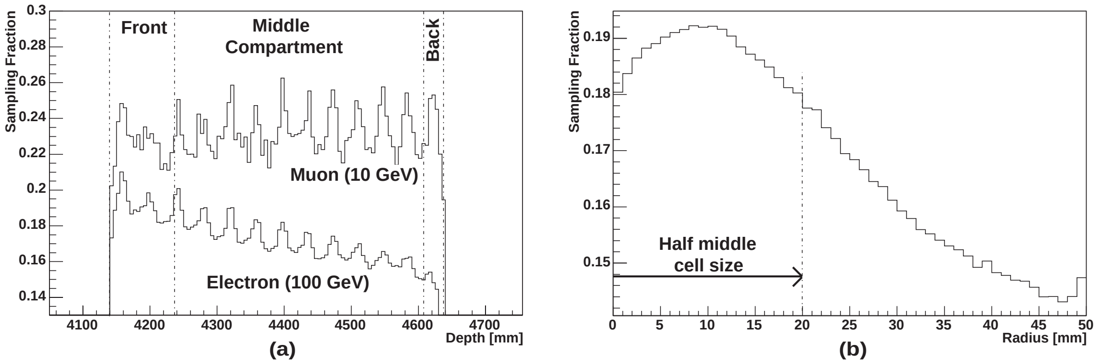

Figure 8.6: (a) Sampling fraction versus depth measured in mm from the origin of the coordinate system for electrons (100 GeV) and muons (10 GeV). One bin corresponds to a plane in the normal to the beam axis. The peaks in the histograms correspond to the accordion folds. (b) Sampling fraction versus radius measured in mm from the beam axis. A bin corresponds to a 'tube' surrounding the beam axis.

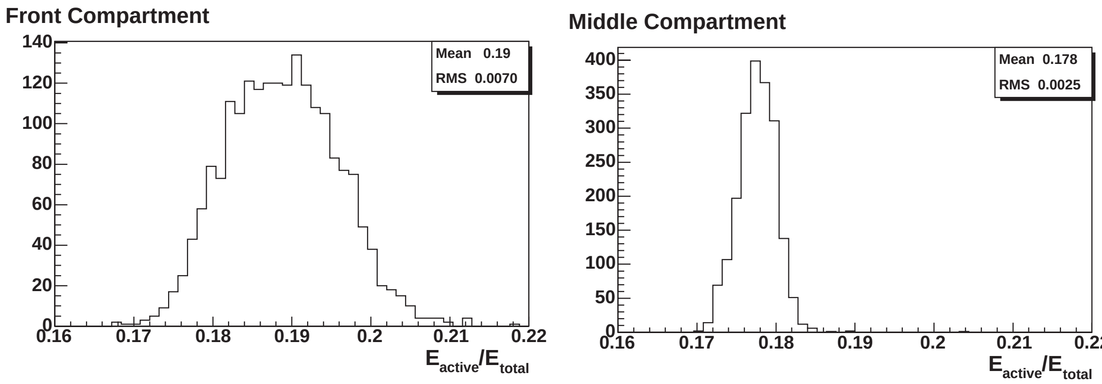

Figure 8.7: Sampling fraction in the front and middle compartment for 100 GeV electrons impinging at η=0.4.

resolution and linearity of the energy measurement since 'early' showers would be treated differently than 'late' ones. Figure 8.7 shows the sampling fraction for the front and the middle compartments separately. Comparing this figure with the plot shown in figure 8.4 one sees also that the distribution of the sampling fraction in each compartment is wider than the total one. The non-uniformity of the sampling fraction in ϕ comes from the absorber/electrode structure of the accordion calorimeter.

The fact that the sampling fraction decreases also with the radius leads to a higher average sampling fraction in small clusters. As shown in figure 8.8, in a 3 $\times$ 3 cluster, the average sampling fraction is about 1% higher than the average over the full beam test module.

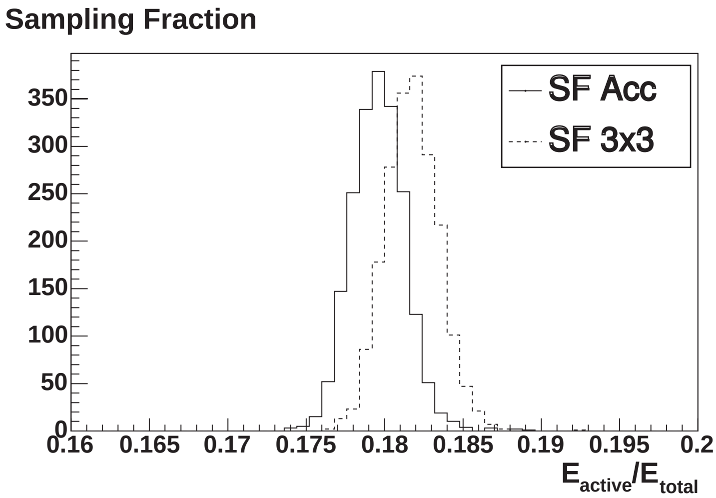

Figure 8.8: Sampling fraction in the full Accordion compared to the sampling fraction in a 3×3 cluster. The average sampling fraction in the cluster is about 1% smaller than in the full accordion.

8.3 Out-of-cluster correction

Another important quantity that can be derived from the Monte Carlo simulation is the correction for energy deposited outside of the cluster. Choosing a bigger cluster size would increase the noise; one achieves better results by keeping the cluster size small and correct for leakage. There is only little fluctuation of width of an electromagnetic cluster. All plots in this section apply for the 3×3 cluster beam test cluster (as described in section 4.2.5).

Figure 8.9 shows the ratio of energy deposit in the full accordion to the energy deposited in the inside of the 3×3 envelope based on a simulation of 1000 electrons of 100 GeV. The impact point (η=0.3625) is the center of a middle cell. This is of course an idealized situation. A Gaussian fit gives a mean value of 1.047 and a sigma of 0.003.

In principle, a similar plot can be obtained from beam test data by comparing the energy in the cluster with the total energy deposit in the accordion. The caveat is that the total accordion energy is biased by noisy cells or cells with problematic calibration. This bias can be evaluated using random trigger events (events without beam particles in the calorimeter). Figure 8.10 shows the out-of-cluster correction obtained by this method from beam test run 1001054 as well as the offset obtained from random events. The factor found is 1.048, slightly bigger than the one found by the idealized Monte Carlo simulation.

In the previous section it was shown that the sampling fraction varies slightly with the distance to the shower axis. Therefore the out-of-cluster correction and the sampling fraction are correlated. As one can see in figure 8.12 more loss outside the cluster (a higher out-of-cluster correction) is correlated with a lower sampling fraction. Both effects

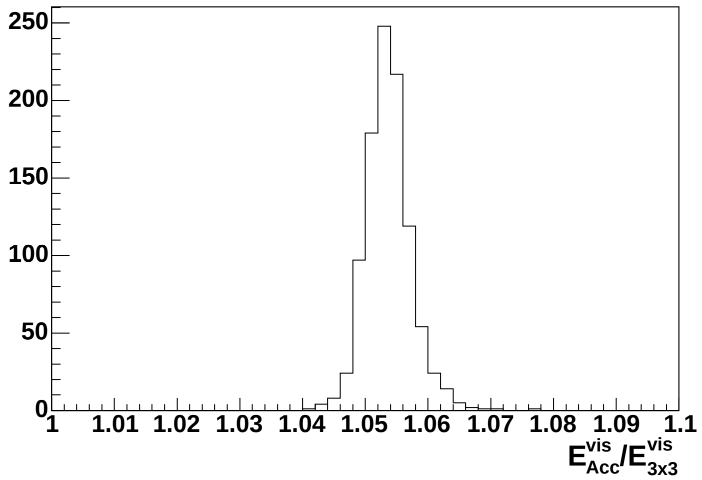

Figure 8.9: Out of cluster correction for 100 GeV electrons in a 3 × 3 cluster. Point-like beam spot impinging at the center of a middle cell.

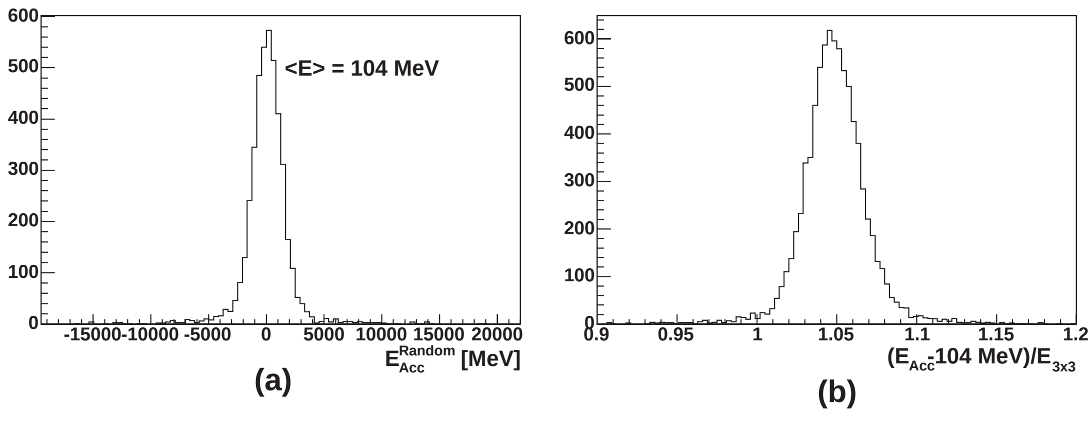

Figure 8.10: (a) The Energy sum of all accordion cells on random events exposes an offset of 104 MeV. (b) Ratio of accordion energy corrected by the offset to 3 × 3 cluster energy. Both plots are made with run 1001054, a 100 GeV electron run.

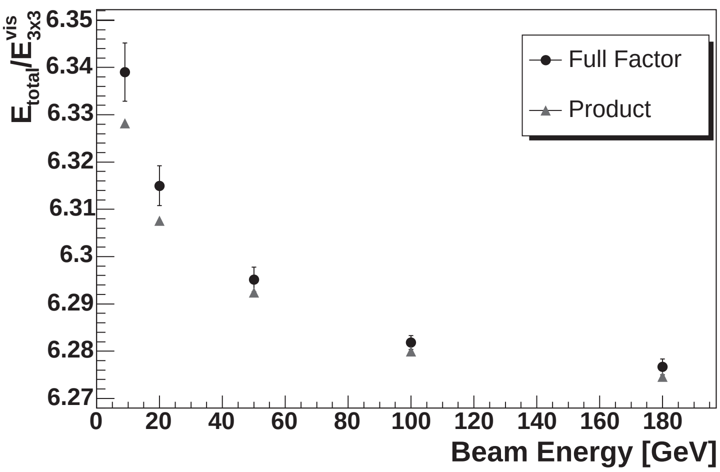

Figure 8.11: Full accordion correction factor and product of out-of-cluster correction and inverse sampling fraction versus beam energy.

go into the same direction: The measured energy fraction is smaller (to get the total energy one has to multiply with the inverse sampling fraction). In particular this means that the product of the average sampling fraction and the average out-of-cluster correction differs from the average of the product: $< 1/f_{SF} > \cdot < f_{OOC} > \neq < 1/f_{SF} \cdot f_{OOC} >$. Figure 8.11 shows the product of these two factors and the total factor depending on the beam energy. The difference is rather small: It is about 0.1% for 9 GeV beam energy and becomes even smaller with increasing energy. Nevertheless, to get an accurate correction factor the out-of-cluster correction and the sampling fraction should be evaluated together as an overall correction factor for the cluster energy in the accordion.

A more important effect is the dependency on the beam energy. Going from 9 to 180 GeV changes the cluster correction factor by about 0.5% (see also figure 8.11). In practice, one average global factor for the sampling fraction is applied at the cell level. Later on, the cells in a cluster are weighted depending on the energy of the impinging particle (that is already roughly known at this point) and on the cluster type. This weight incorporates the out-of-cluster correction as well as the change of the sampling fraction.

It is obvious that the out-of-cluster correction has a significant dependence on the impact point. It becomes minimal, if the impact point is in the middle of the seed-cell and increases towards the cell boundary. As one can see in figure 8.13, the dependence of this correction factor on η and ϕ has a parabolic behaviour. The out-of-cluster correction is the only kind of correction that depends on the η-position, since the calorimeter is perfectly uniform in this direction (except of the crack regions). It can be fitted by the function

$$\frac{E(\Delta\eta)}{E(\Delta\eta = 0)} = 1 + a\Delta\eta^2 \tag{8.1}$$

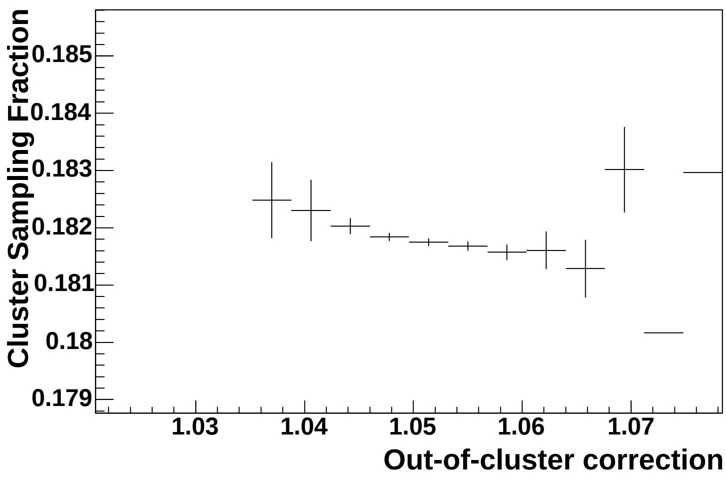

Figure 8.12: Correlation of sampling fraction inside a 3 × 3 cluster and the out-of-cluster correction

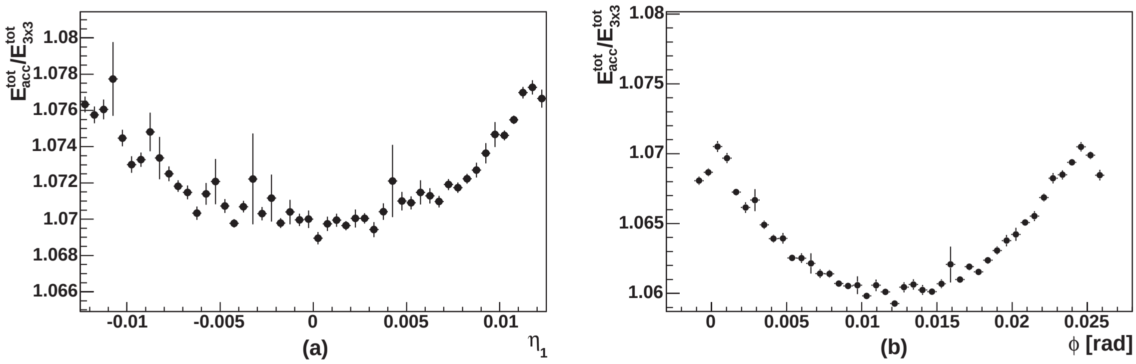

Figure 8.13: Out-of-cluster correction versus the impact point in η (a) and ϕ (b) obtained from the beam test simulation. In the simulation, one coordinate has been fixed and the other varied such that it covers the width of one middle cell. The η value in plot (a) is the energy-weighted average of the front compartment, the ϕ coordinate in plot (b) is the true angle of the beam with respect to the horizontal plane.

where $\Delta\eta$ is the distance of the impact point to the center of the seed cell in the middle compartment. The parameter a is obtained by a fit. The η coordinate can be obtained with good accuracy from the energy bary-center in the strips compartment. In the example show in figure 8.13, the a is equal to 34.

The ϕ-correction depends also on other effects (sampling fraction, charge collection) and is evaluated together with them in section 8.5.

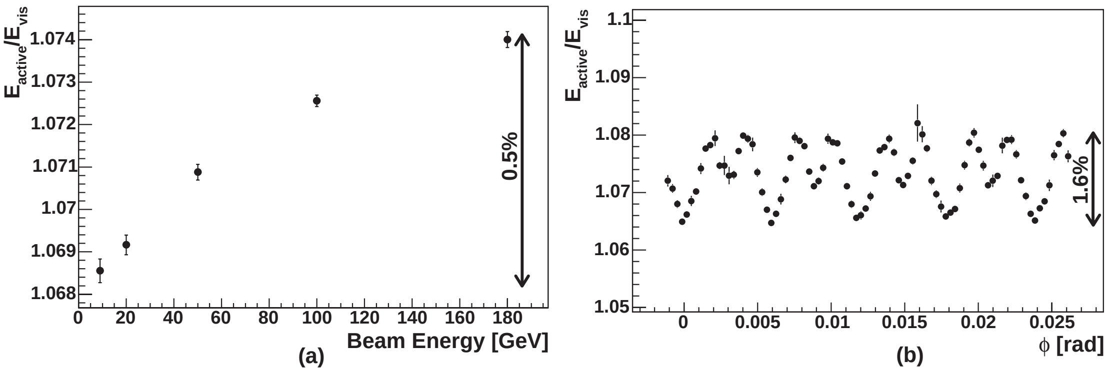

Figure 8.14: Dependece of the ratio of visible energy to the energy deposit in the active region on the beam energy (a) and the ϕ-impact point (b). The second plot was made by varying the direction of the particle at the primary vertex in the beam test simulation. The range corresponds roughly to one middle cell width.

8.4 Charge collection effect

The Monte Carlo simulation used allows to compare the true energy deposit in the active region (labeled 'active calibration hits') with the visible energy. The latter includes the effect of the inhomogeneous electrical field in the folds of the accordion. Since the fraction of the shower that covers straight sections and the bend sections fluctuates, this correction factor fluctuates as well. Similarly to the sampling fraction, this correction depends on the impact point in ϕ and the particle energy. Figure 8.14 shows plots of these dependencies obtained from the beam test simulation.

8.5 Overall accordion correction factor

All the effects mentioned in the previous sections together accumulate to an 'effective sampling fraction', a factor that transforms the measured energy inside a cluster into a total energy deposit in the accordion calorimeter. This factor depends slightly on the energy of the impinging particle as well as on the impact point. From 20 to 180 GeV it changes by about 1%. Figure 8.15 shows this factor versus the beam energy and figure 8.16 versus the ϕ impact point.

In practice, not this 'effective sampling fraction' is applied, but a constant factor at the cell-reconstruction level, and an energy dependent correction factor is later at the cluster level.

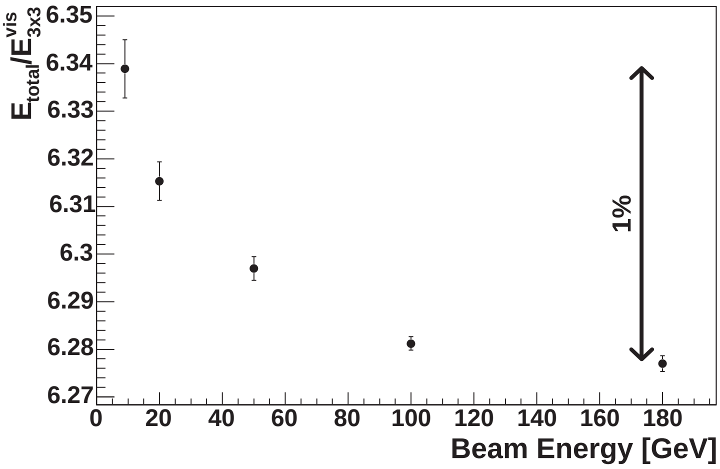

Figure 8.15: Ratio of the total energy deposit in the accordion to visible energy in the cluster versus beam energy. This includes the inverse sampling fraction, the out-of-cluster correction as well as the effect of the accordion folds. Derived from the beam test simulation with a 3x3 cluster at $\eta = 0.4$ and $\phi = 0$.

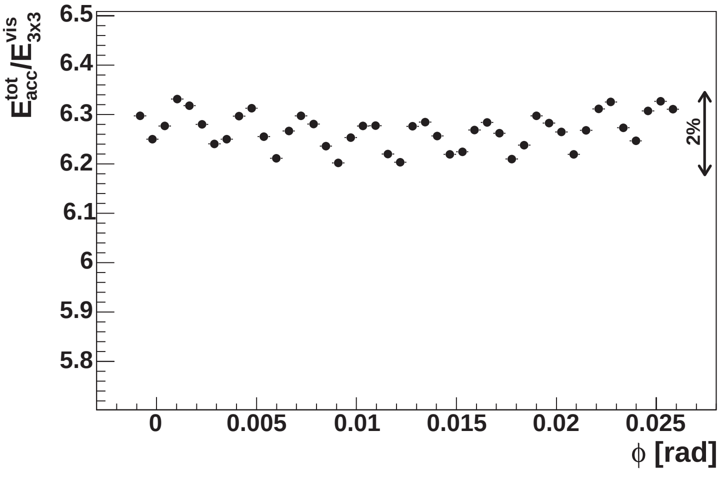

Figure 8.16: Ratio of the total energy deposit in the accordion to measured energy in a 3×3 cluster versus impact point in ϕ for 100 GeV electrons. A middle cell goes from 0 to approximatly 0.025.

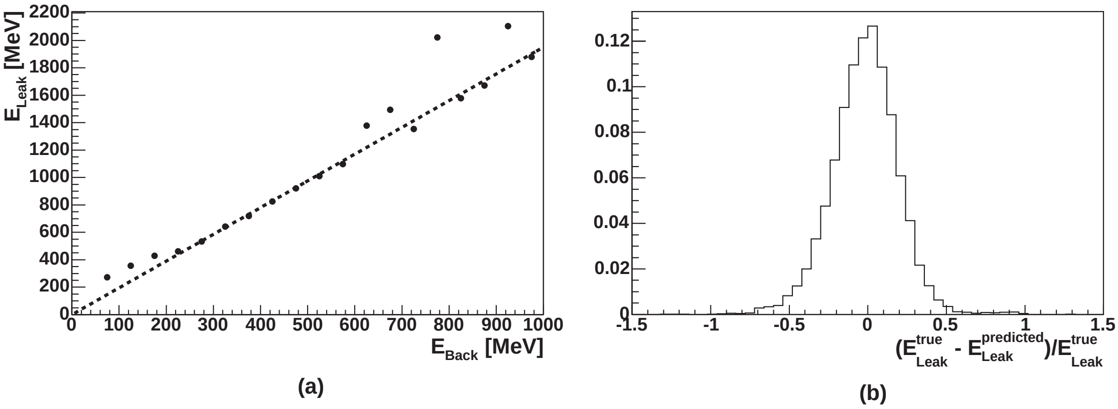

Figure 8.17: (a) Correlation of the energy deposit in the back compartment and the leaking energy 100 GeV electrons at η=0.4. (b) Accuracy of the leakage correction using the back comparment.

8.6 Back leakage

Even though the calorimeter is thick (about 22 X_0 at η=0.4) a fraction of the energy leaks out of the back of the calorimeter. For 20 GeV electrons, about 80 MeV are deposited behind the last sampling of the calorimeter. For 250 GeV, the leakage is about 2.2 GeV. So about 0.4% to 0.9% of the intial electron energy is lost behind the calorimeter.

Especially for lower rapidities where the calorimeter is thinner, significant fluctuations of the leakage are observed. An event-by-event correction is needed. There are two variables sufficiently correlated to the leaking energy to be used: The energy in the back compartment and the mean shower depth. The mean shower depth defined by

$$< l >= \frac{\sum_{i=0}^{3} E_i l_i}{\sum_{i=0}^{3} E_i} \tag{8.2}$$

where E_i is the energy in each compartment and l_i is the position of each compartment in radiation lengths.

Figure 8.17 illustrates the first method. Plot (a) shows the correlation between the energy deposit in the back compartment and leakage energy. The slope obtained by a linear fit is then used to estimate the leakage using the energy in the back. Plot (b) shows the deviation of this prediction from the true value. A relative deviation of about 20% is achieved.

8.7 Upstream energy loss

To first order, upstream material followed by a presampler can be regarded as a simple sampling calorimeter consisting of only one absorber and one active layer and can be

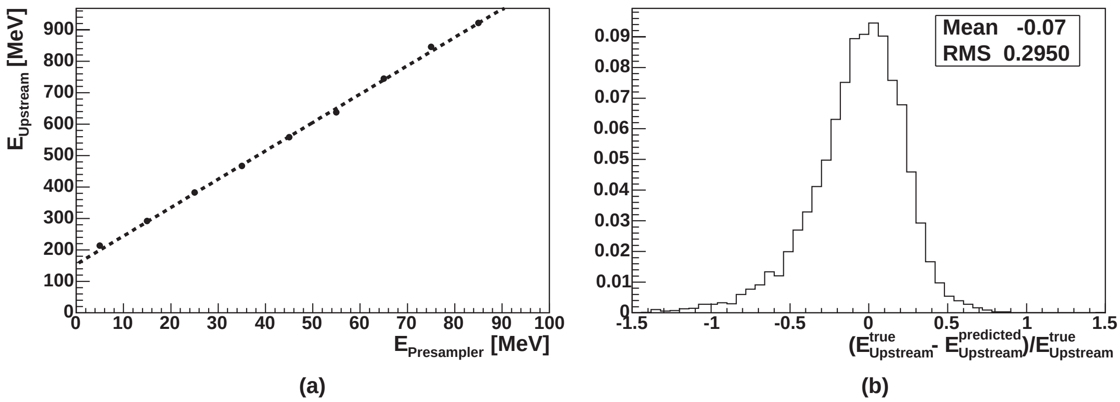

Figure 8.18: (a) Correlation of upstream energy deposit and energy deposit in the presampler for 100 GeV electrons in the beam test setup with 1.8 X_0 upstream of the presampler. (b) Accuracy of the estimation of the energy deposit upstream of the presampler.

calibrated with a 'sampling fraction'. A look at the Monte Carlo simulation reveals that this model is too simple. Figure 8.18 shows the correlation of the energy lost upstream to the energy deposit in the presampler for 100 GeV electrons. A linear fit yields a smaller slope than what one would expect from a first-principle calculation and does not go through the origin, but has a significant intercept.

Discussing the early shower development helps to understand this effect. An electron passing through the inactive material upstream of the presampler does not only loose energy by ionization, but it radiates also photons by bremsstrahlung. These photons do not deposit energy by ionization. Since the amount of upstream material (~ 2 X_0) is of the same order as the mean free path length of a photon ($9/7$ X_0) e^+e^- pairs will be created around the presampler. In case the pair is produced before the presampler three ionizing particles pass the presampler, but most of the material before the presampler has been traversed only by the beam electron. Since the energy deposit in the presampler is roughly proportional to the number of charged particles crossing, one observes a much higher energy deposit than expected by the simple model. In the limit of a hard bremsstrahlung before the presampler, only a high-energy photon crosses the active layer leaving no energy in the presampler even though some energy has been lost by the beam electron before. This is the explanation for the offset.

From figure 8.18 (a) we conclude the following formula to estimate the energy loss upstream of the presampler [24]:

$$E_{upstream} = a + b \cdot E_{PS} \tag{8.3}$$

The parameters a and b have to be derived from a Monte Carlo simulation by fitting a straight line to the correlation of the true upstream energy deposit to the measured presampler energy. The offset a (given in MeV) describes the average energy loss by the incident electron before it reaches the presampler. This includes not only the ionization energy loss but also low-energy bremsstrahlung-photons emitted by the incident electron. If the photon energy is too small, it does not produce an electron pair that reaches the presampler. The slope b accounts for e^+e^- pairs traversing the presampler and a fraction of the inactive material before. Both parameters depend on the beam energy.

Using the same simulation of 100 GeV electrons in the beam test setup as before, one can assess how well equation 8.3 can predict the upstream energy loss. Figure 8.18 (b) shows the relative accuracy. A gaussian fit yields a sigma of 0.23, hence using equation 8.3 one can predict the energy loss upstream with an accuracy of 23%.

In particular for low energies, the distribution of the upstream energy loss shows a non-gaussian tail towards higher energy deposit while the energy deposit in the presampler is closer to a gaussian distribution. The tail is not correlated to the presampler energy and cannnot be recovered by equation 8.3. This introduces a small tail in the total measured energy distribution towards lower energies. If the parameters a and b are derived from the mean energy deposit (including the tail) the mean of the distribution will be corrected. However, it is better to reduce the influence of the tails by fitting a gaussian (with asymetric fit boundaries) on the upstream energy deposit for each bin of the presampler energy.

Thus the tail is excluded and does not bias the result, and most of the events are correctly reconstructed.

8.8 Energy loss in the gap between presampler and strips

The energy deposit in the inactive region between the presampler and the strips compartment of the accordion calorimeter is more complicated, since the shower is more developed. The energy deposit in this region is neither well correlated with the presampler measurement nor with the strips compartment. A suitable correlation was empirically found using a combination of presampler energy and strips energy:

$$E_{Gap} = c \cdot (E_{PS} E_{Strips})^{0.5} \tag{8.4}$$

Figure 8.19 (a) shows the correlation between the result of equation 8.4 and the true energy deposit for 100 GeV electrons. Figure 8.19 (b) shows the difference between predicted and true energy deposit divided by the true energy deposit.

8.9 Longitudinal shower fluctuation

This section is devoted to a more detailed study of the development of the electromagnetic shower. It concludes in an alternative way to compute the energy loss in dead regions, in particular in the region between presampler and accordion using the parametrization of the electromagnetic showers known as Longo-Sestili formula. The square-root parametrization

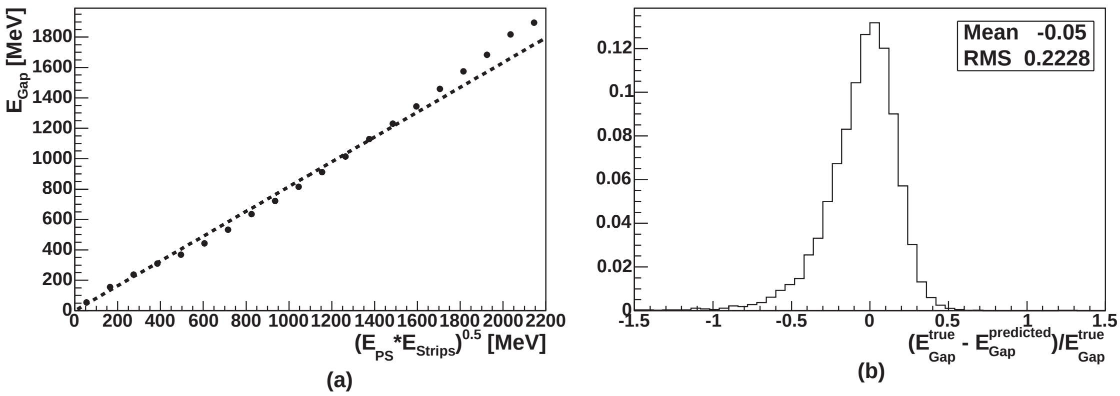

Figure 8.19: (a) Correlation of the energy deposit in the gap between presampler and accordion with the square root of the product of the energy deposit in the presampler and the strips compartment. (b) Accuracy of the estimation using this correlation. The figures where made using a simulation of 100 GeV electrons impinging at η=0.4.

used in equation 8.4 does actually give resonable results but is purely empirical, without any physical justification.

8.9.1 The Longo-Sestili formula

The Longo-Sestili [16] formula

$$N(t) = A \cdot t^{a-1} e^{-bt} \tag{8.5}$$

allows to calculate the average the number of charged particles passing a certain plane perpendicular to the incident particle track. The depth t is given in radiation lengths. The parameters can be found by a fit. The parameter A is the amplitude, a and b are related to the shower depth and the shower length.

The formula is an empirical formula that was found by studying a Monte Carlo Simulation of a photon beam on a Lead Glass target. There are some differences to our situation. First, an electron shower does not necessarily look like a photon shower, especially in the beginning. Second, our setup is not homogeneous. Third, we want to know the event-by-event shower fluctuations not only the average over many showers. Moreover, we are not interested in the number of particles but rather in the energy deposit.

The Particle Data Handbook [8] gives an alternative formulation of the Longo Sestili formula that yields the energy loss per radiation length.

$$\frac{dE}{dt} = E_0 b \frac{(bt)^{a-1} e^{-bt}}{\Gamma(a)} \tag{8.6}$$

Equation 8.6 can be derived from 8.5 by multiplying with the ionization energy loss and the postulation that

$$\int_0^\infty \frac{dE}{dt} dt = E_0 \tag{8.7}$$

This assumes implicitly that the ionization energy per radiation length is constant. This assumption is on average true in the accordion calorimeter but certainly not upstream where the material distribution is very inhomogenous. Experimental observables are only the energy deposits in the different compartments. This corresponds to an integral of the Longo-Sestili formula over the length of the compartment in radiation lengths. So the integral in equation 8.7 has to be broken down into parts according to the longitudinal structure of the calorimeter:

$$\underbrace{\int_0^{t=PS1} \left.\frac{dE}{dt}\right|_{Upstr} dt}_{\text{upstream}} + \underbrace{\int_{t=PS1}^{t=PS2} \left.\frac{dE}{dt}\right|_{PS} dt}_{\text{Presampler}} + \underbrace{\int_{t=PS2}^{t=Front} \left.\frac{dE}{dt}\right|_{Gap} dt}_{\text{Gap}} + \underbrace{\int_{t=Front}^{t=Middle} \left.\frac{dE}{dt}\right|_{Acc} dt}_{\text{Front}} +$$
$$\underbrace{\int_{t=Middle}^{t=Back} \left.\frac{dE}{dt}\right|_{Acc} dt}_{\text{Middle}} + \underbrace{\int_{t=Back}^{t=End} \left.\frac{dE}{dt}\right|_{Acc} dt}_{\text{Back}} + \underbrace{\int_{t=Back}^{\infty} \left.\frac{dE}{dt}\right|_{Acc} dt}_{\text{downstream}} = E_0 \tag{8.8}$$

Where the $\frac{dE}{dt}$ contains the average ionization energy for the respective compartment. In this context it is important to keep in mind that the shower development is governed by radiation length, whereas the energy loss by ionization is given per length (usually cm).

Four of the six terms of equation 8.8 are measured. The back compartment is not very useful for this purpose, since the energy deposit there is very small. This leaves three observable quantities: The energy deposits in the presampler, the front and the middle compartment. This is in principle enough to fit the parameters a and b and use them to predict the energy loss in inactive regions.

To use the mathematical description of the shower shape given by Longo and Sestili, one needs to overcome the following problems:

- Do equation 8.5 or 8.6 also describe the beginning of the shower well enough and is it also a good description for an individual shower?
- How to deal with the different ionization energies in the accordion, the presampler and the gap between presampler and the accordion.
- The geometry in terms of radiation lengths needs to be known.

To answer all these questions detailed Monte Carlo Simulations where carried out and are described in the following sections.

8.9.2 Radiation length scan

One important input parameter for a shower shape fit is the geometry of the detector in terms of radiation lengths, meaning the number of radiation lengths a particle traverses before it reaches a certain compartment of the calorimeter.

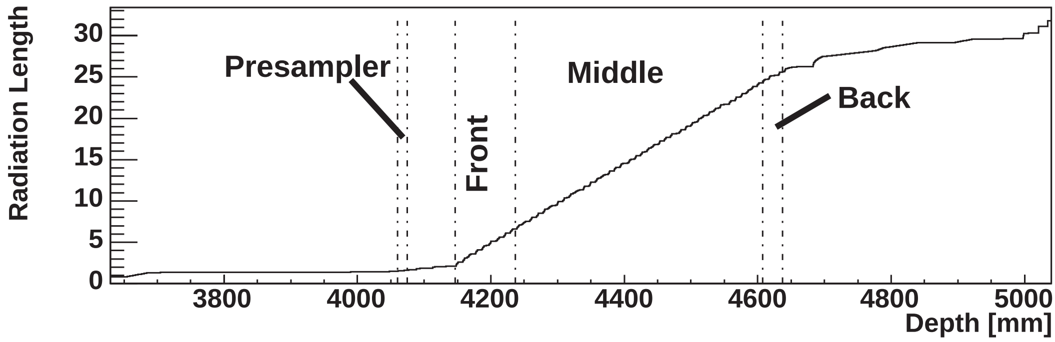

Figure 8.20: Accumulated radiation length versus distance to the origin. The origin of the beam test coordinate system is about 3m upstream of the liquid argon cryostat.

These values depend strongly on η and ϕ. Especially the inactive region between the presampler and the strips depends on ϕ since the presampler is a flat structure that is mounted on the inner bore of the accordion calorimeter that is round.

We extract the radiation lengths also from the Monte Carlo simulation, assuming that the geometry is sufficiently well described. Using geantinos[1], a list containing the distance to the origin, the integrated radiation lengths as well as the current volume is created. This list is read in by a subsequent simulation job in order to create the histograms described above.

Table 8.1 shows the most important lines (the transition points between the compartments) of this list. The complete relation of length versus radiation length at η=0.4 and ϕ slightly above zero is shown in figure 8.20. The impact point at ϕ=0 should be avoided for this purpose since the geantino would pass exactly between the two presampler modules and would not tell us the right geometry.

8.9.3 Monte Carlo simulations to study the shower shape

For this study the standard Geant4 simulation of the 2004 H8 run was used. The impact point was chosen according to the material runs at η=0.376 and ϕ=0. In contrast to the geantino-scan, the ϕ=0 point is acceptable for electrons since they develop a shower with a certain width.

In addition to the standard output of the simulation, the following quantities have been calculated:

- Energy deposit versus depth in bins of 1 mm

[1]Geantinos are a Geant4 construct. These "particles" do not interact with matter, they just carry information about the geometry they traverse. They are very useful for tasks like debugging the Geant4 geometry.

Position	x [mm]	X_0
Presampler begin	4060.1	1.8
Presampler end	4074.9	1.9
Front	4146.2	2.4
Middle	4236.4	6.9
Back	4607.8	24.6
Accordion end	4637.2	25.9

Table 8.1: Compartment boundaries in mm and radiation lengths in the beam test setup. The x position is given with respect to the origin of the beam test setup as described in section 5.2.1, the radiation length are counted from the position of the Geant4 particle gun that 27.5 m upstream of the origin of the coordinate system.

- Number of charged tracks versus length in bins of 1 mm
- Energy versus radiation length in bins of 0.025 X_0
- Number of charged tracks versus radiation length in bins of 0.025 X_0

By 'number of charged tracks' we mean the number of tracks crossing a plain of constant depth. There is one such histogram per event and one histogram of each kind summed up over all events. The histograms of energy and tracks versus number of radiation lengths allows to judge how accurate the Longo-Sestili formula describes the shower shape of an individual event.

Number of charged tracks versus depth

Figure 8.21 shows the number of charged particles in the shower versus the depth in radiation lengths. Using a radiation length scan as described in the previous section, a mapping of depth im mm (x-coordinate in the beam test coordinate system) and depth in radiation lengths was produced. This map has one entry for each material transition. The conversion from mm to X_0 stretches the lead fraction, since it corresponds to many radiation lengths while the argon fraction gets compressed, since it is very thin in terms of radiation lengths (compared to the absorber). This explains the spikes in the histogram. Interesting for our purpose is mainly the average behavior over larger regions, e.g. the samplings of the calorimeter so the spikes can be smeared out.

The Longo-Sestili was fitted by minimizing

$$\sum\left(\frac{L_i^{measured} - L_i^{calculated}}{L_i^{calculated}}\right)^2 \tag{8.9}$$

where $L_i^{measured}$ is the total integrated track lengths per compartment of the calorimeter (in this context, the histogram bin-sum) and $L_i^{calculated}$ the integral of the Longo-Sestili

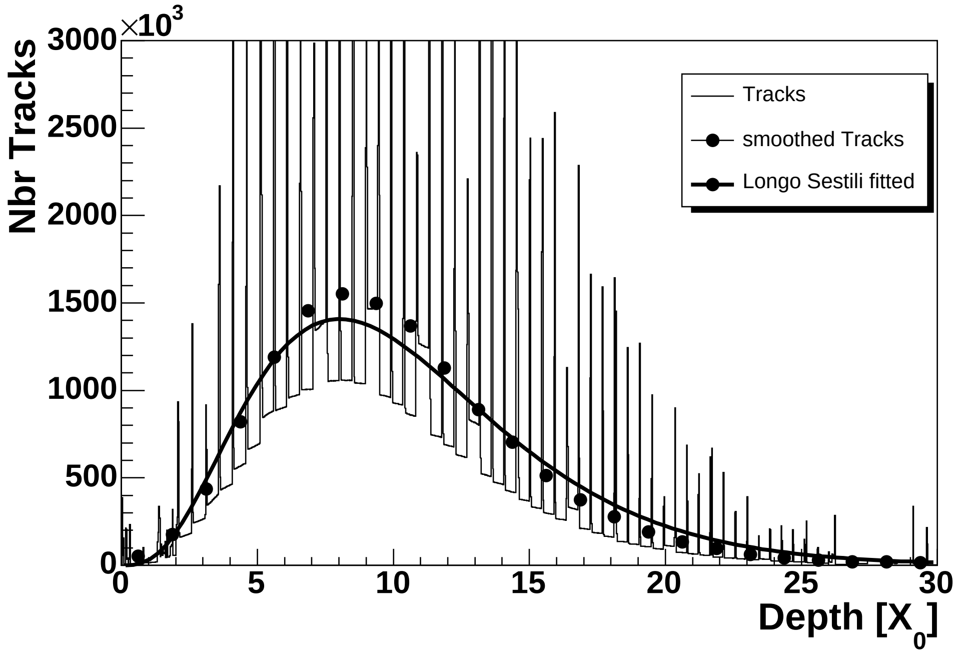

Figure 8.21: Average number of charged particle tracks versus depth in radiation lengths (thin line) and smoothed (dots). The thick line marks the fitted Longo-Sestili formula. Averaged over 1000 events of 100 GeV electrons. The bin width is 0.025 X_0.

formula over each compartment. The sum comprises the presampler, the strips and the middle compartment.

Figure 8.21 shows a satisfying agreement of the fit in particular in the region around 2 X_0 where the gap between presampler and strips lies. It is remarkable that the fit using the integrals over the compartments achieves a better agreement in the early part of the shower than a fit using all bins of the histogram. In constrast, description of the falling edge is worse.

8.9.4 Energy loss by ionization in the beam test setup

In order to connect the number of charged particles (the value given by the Longo-Sestili formula) to the energy deposit one needs to know the average ionization energy loss (per radiation length) of electrons and positrons. This value depends on the material and is therefore different for the various regions of the setup like the presampler, the inactive region between the presampler and the front compartment and the accordion.

Figure 8.22 shows the energy deposit and the number of charged tracks versus the depth in bins of one millimeter as well as the energy deposit per track obtained by dividing the energy deposit by the number of tracks for each bin.

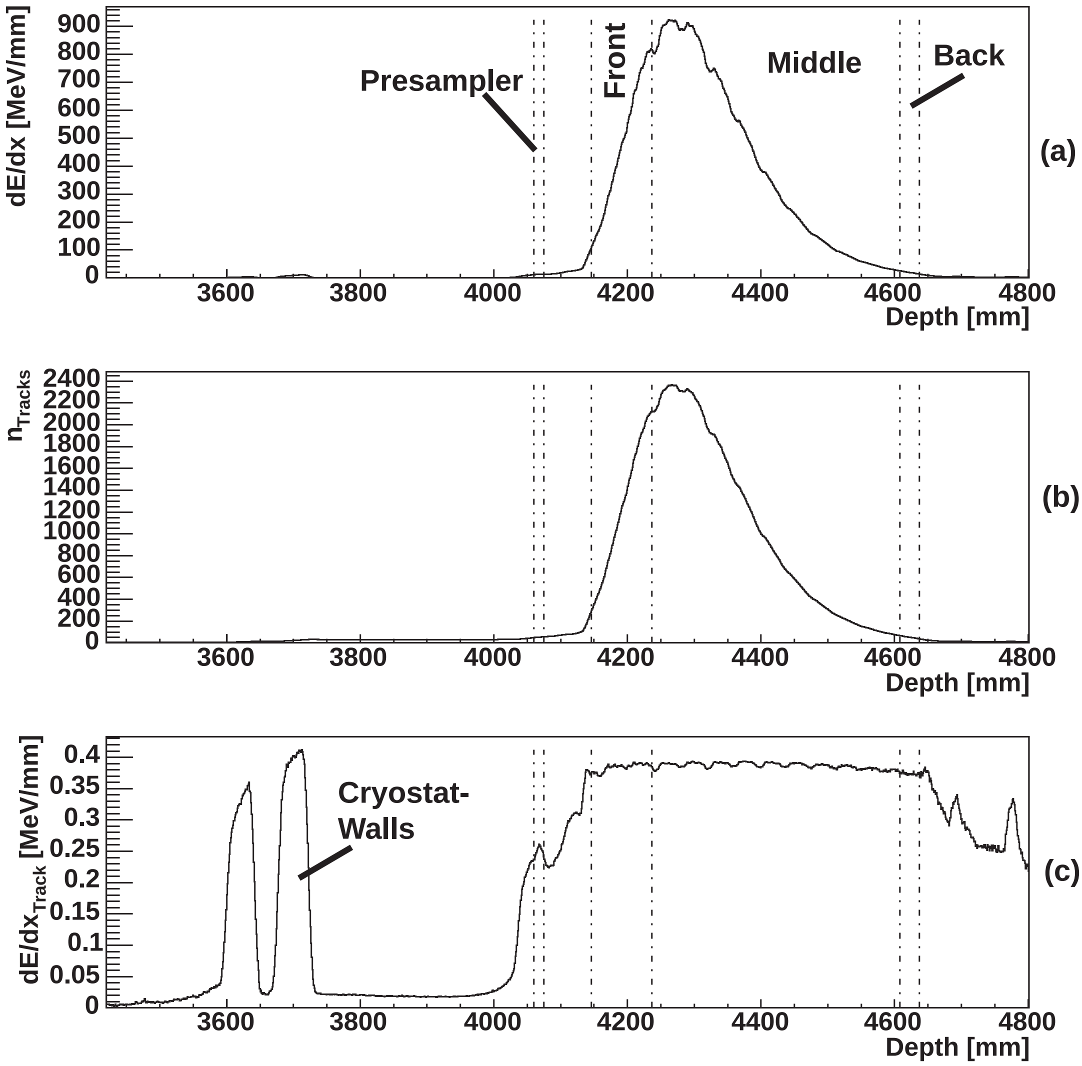

Figure 8.22: Average energy deposit (a) and average number of charged tracks (b) in bins of 1 mm in the beam test setup. Histogram (c) shows the average energy deposit per charged track and mm obtained by dividing (a) by (b). The vertical dashed lines indicate the compartment boundaries. All shown quantities are averaged over 1000 events.

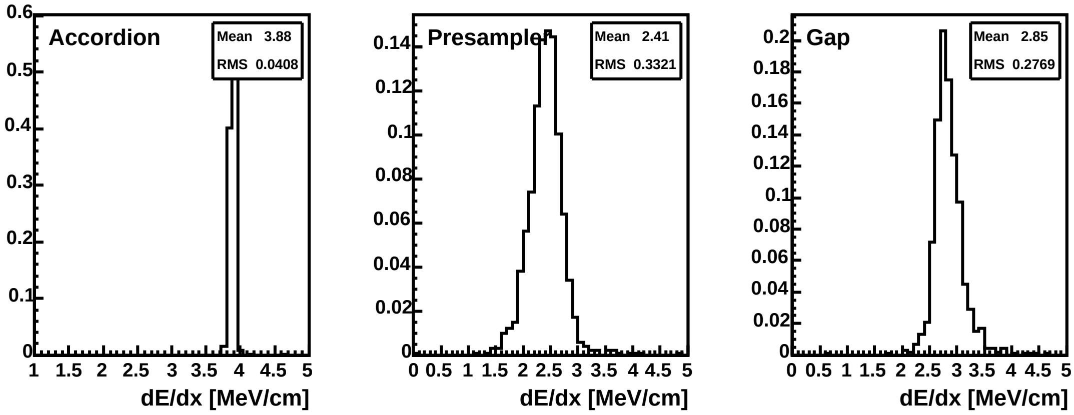

Figure 8.23: Energy deposit per charged track and per radiation lengths for the accordion calorimeter (left), the presampler (middle) and the inactive region between presampler and strips (right). The incident particles are electrons of 100 GeV.

In principle, the energy deposit per track in each region can be read from this figure (and converted from the mm scale to a radiation-length scale), but this method is not very accurate and can cause rounding-errors. Instead, the total track lengths and the total energy deposit in each region (upstream, presampler, accordion, ...) were calculated on an event-by-event basis and their quotient was put into histograms. The result for the accordion, the presampler and the inactive region between presampler and strips is shown in figure 8.23.

For a minimum ionizing particle, one would expect an energy deposit of about 5.3 MeV/cm for the accordion calorimeter and 2.1 MeV/cm for the presampler which consists only of liquid argon (see appendix C). The histograms in figure 8.23 are made with electrons. It shows a sharp peak at 3.88 MeV/cm for the accordion. This corresponds to 7.84 MeV/X_0. For the presampler one gets 2.41 MeV/cm or 33.74 MeV/X_0. This value fluctuates more, since fewer particles go through the presampler than through the accordion. This means that the same integrated track length (measured in radiation length) deposits 33.74/7.84=4.3 times more energy in the presampler than in the accordion calorimeter. This factor has to be applied in order to include the presampler in a fit of the Longo-Sestili formula to the shower shape.

8.9.5 Result of the shower-shape fit

Using the results from the previous section, one can fit the parameters a and b of the Longo-Sestili formula to the energy deposits in the presampler and the first two comparments of the accordion. Figure 8.24 shows the correlation of the true energy deposit to the energy deposit calculated by Longo-Sestili with the fitted parameters. The fit was done by minimizing the relative deviation of the energy $(E^{measured} - E^{predicted})/E^{measured}$ for each compartment. This leads to a high weighting on the strips compartment and the presampler despite the relatively small energy deposit there. This is desireable, since we want to correct for energy deposit before the accordion calorimeter. The calculated energy deposits are almost perfectly correlated to the measured ones, in particular for the presampler and the strips compartment.

Figure 8.25 shows the same plots done on data. Similarly to the simulation, the calculated and the measured values for the presampler and the strips are almost identical, the middle compartment shows a broader distribution.

In the case of simulation, where the energy deposit in the gap between strips and presampler is known, we can also estimate how well the energy lost in this region can be predicted. Figure 8.26 shows the correlation between the true and the predicted energy deposit as well as a histogram of the relative error of the prediction. A gaussian fit yields a sigma of 18%.

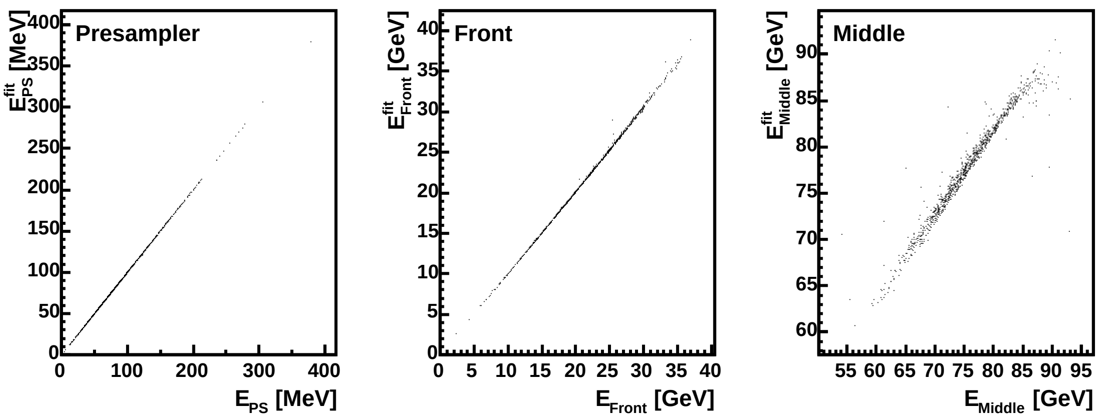

Figure 8.24: Result of a fit of the Longo Sestili formula to the energy deposits in the presampler, front and middle compartment based on the simulation of 100 GeV electrons. The correlation of the true energy deposit to the one obtained by the fit is shown.

Fitting of the Longo-Sestili formula does work in principle and gives slightly better results than the empirical method with the square-root term. But this advantage comes at a high cost: one has to invoke a fitting routine for each event, which is extremly CPU-intensive. Furthermore, for a small fraction of the events ($\sim$2%) the fit does not converge.

The method might be extended in the futur. To really make it applicable, one needs to find a way of getting the parameters of the Longo-Setstil formula without invoking a fit-routine, e.g. by iteration.

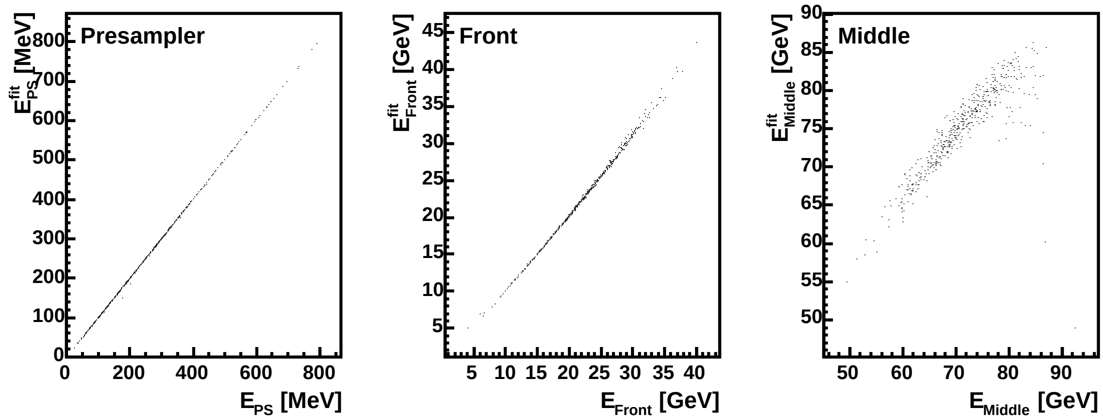

Figure 8.25: Result of a fit of the Longo Sestili formula to the energy deposits in the presampler, front and middle compartment based on the beam test run 1000952 (100 GeV electrons at η=0.37). The correlation of the true energy deposit to the one obtained by the fit is shown.

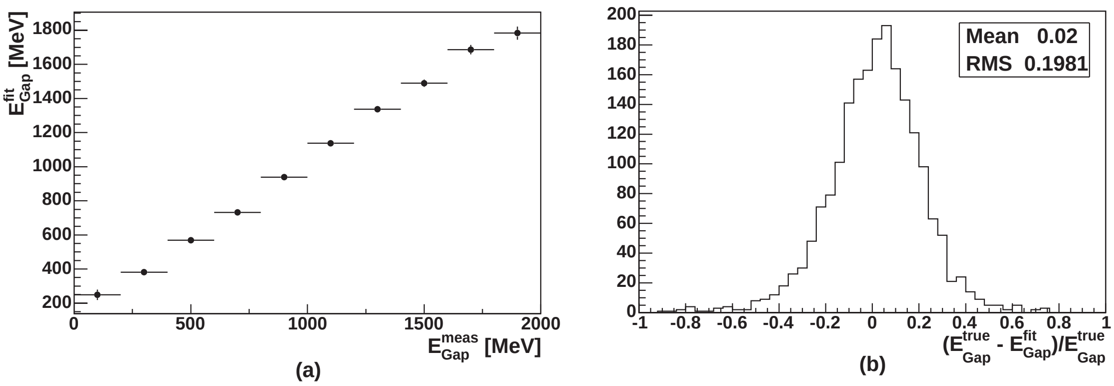

Figure 8.26: (a) Correlation of the true energy deposit in the gap between presampler and strips compartment and the predicted energy deposit achived by a fit of the Longo-Sestili formula. (b) Accuracy of this prediction.

8.10 Summary of calibration scheme

The bulk of the energy of an electromagnetic interacting particle coming from the interaction point (or from the beam line in the beam test case) is absorbed in the calorimeter modules and measured as cluster energy. A certain fraction of the energy is lost in the inactive materials surrounding the calorimeters or leaking outside of the cluster. One can distinguish three inactive regions: upstream, the gap between presampler and strips and downstream leakage. The methods presented in this chapter allow to correct for this loss in these regions.

The calibation can be summarized by the following formula:

$$E = \underbrace{a + b \cdot E_{PS}}_{\text{upstream}} + \underbrace{c \cdot \sqrt{E_{PS} E_1}}_{\text{gap}} + \underbrace{d(E_1 + E_2 + E_3)}_{\text{accordion}} + \underbrace{e \cdot E_3}_{\text{downstream}} \tag{8.10}$$

E_{PS} and E_1 to E_3 are the cluster energies in the presampler and the compartments of the accordion calorimeter respectivly. The calibration constants a to e can be derived from a Monte Carlo simulation. They depend sightly on the beam energy and on the upstream material (thus on η).

Alternatively, the energy deposit in the inactive regions can be predicted by a fit of the Longo-Sestili formula to the measured compartment energies.

Chapter 9

Results

9.1 Results from beam test 2002

In 2002, a beam test with a series module of the Liquid Argon Barrel Calorimeter was carried out including an energy scan from 10 to 180 GeV. The setups of the 2002 and 2004 beam tests show some important differences:

- The 2002 run was a Liquid Argon Calorimeter standalone run using a dedicated test beam data acquisition and analysis software while 2004 was carried out jointly with the other ATLAS subdetectors using the ATLAS data acquisition and analysis software.
- In 2002, the beam energy was controlled up to an uncertainty of $3 \cdot 10^{-4}$ using a precision power supply for the bending magnets of the magnetic spectrometer of the beam line together with a sophisticated calibration of their bending power. Although the 2004 run was carried out in the same beam line, the equipment for the precision current measurement was not in place any more. Therefore the accuracy of the beam energy measurement was only of the order of $5 \cdot 10^{-3}$.
- The 2002 data was taken at an η position where the calorimeter is more than 30 X_0 thick and back leakage was very small. This is not the case for 2004 data.

The simulation of the 2002 beam test showed an exeptionally good agreement with data. The mean reconstructed energy in the PS and in the first and second compartment of the accordion is described by the Monte Carlo simulation for all energies within 2%. In addition, also the shape of the energy distributions within each compartment are well described.

Using the calibration scheme summarized in equation 8.10 a linearity of the energy response of 0.1% has been reached for the energy range from 15 to 180 GeV. The sampling term of the energy resolution is $10\%/\sqrt{\mathrm{GeV}}$. Figure 9.1 summarizes these results [24].

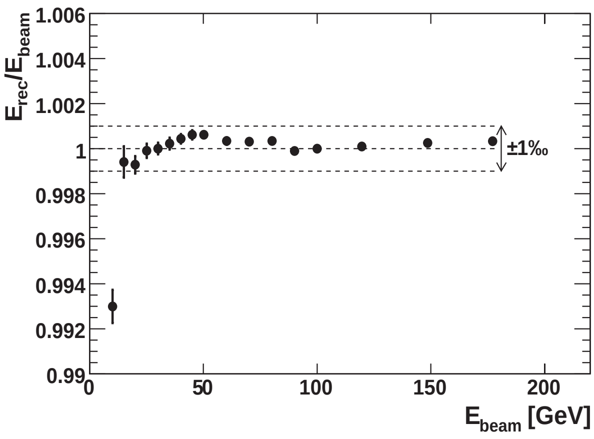

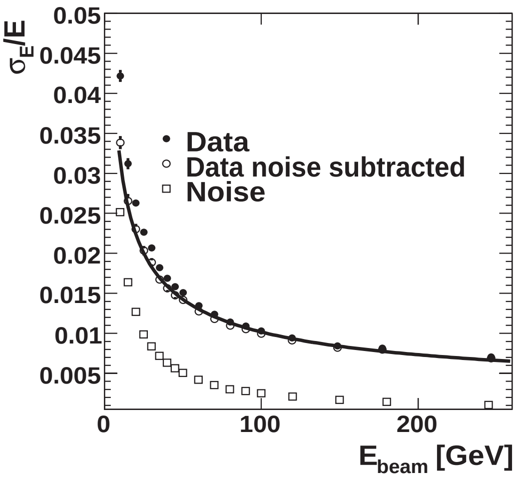

Figure 9.1: Linearity and resolution obtained from 2002 beam test data. The linarity plot is normalized to the 100 GeV point. The fit on the resolution yields a sampling term of $10\%/\sqrt{\mathrm{GeV}}$ and a constant term of 0.2%.

9.2 Material scan in the 2004 beam test

To validate the calibration scheme discussed in chapter 8 and to extend the results obtained in 2002 with different amounts of upstream material a dedicated material scan was carried out during the 2004 combined run.

To realize additional inactive material in front of the cryostat, plates of aluminum have been placed on a support stand about 6 cm upstream of the outer cryostat wall. Up to three plates of 2.5 cm thickness have been used. Since the cryostat was rotated to mimic and impact point at $\eta = 0.367$, particles traversed the plates that were parallel to the cyrostat at an angle

$$\theta = 90^\circ - 2 * \arctan(e^{-\eta}) = 21.05^\circ \tag{9.1}$$

and the effective thickness d_{eff} seen by the particle is given by

$$d_{eff} = \frac{d}{\cos(\theta)} \tag{9.2}$$

The effective thickness in millimeter and radiation length is summarized in table 9.1

9.2.1 Data points and cuts

The material runs carried out during the 2004 combined beam test include six different energies from 9 to 250 GeV and four material configurations. For each data point a Monte-Carlo sample of 10k events has been produced. Table 9.2 summarized the used runs with their beam energy calculated from the magnet currents,[19], the cut on the impact point

Nbr of plates	d_{eff} [mm]	d_{eff} [X_0]	Total upstream [X_0]
0	-	-	2.4
1	26.8	0.301	2.7
2	53.6	0.602	3.0
3	80.4	0.903	3.3

Table 9.1: Effective thickness of the different upstream material configurations in mm and X_0. One radiation length in Aluminum corresponds to 8.9 cm. The last column lists the total number of radiations lengths before the accordion calorimeter.

that has been applied and the estimated number of electrons. The electrons have been selected by a cut on the ratio of energy deposit in the front and the middle compartment. This allows to efficently reject pions and muons in the electron beam and does not bias the electron energy measurement.

The error on the beam energy given in the table is the beam spread due to the opening of the collimatiors. It is problably an overestimation since the collimators have been wide open and did not limit any more the angular distribution of the beam particles. The limit was rather given by the focussing optics of the beam line. Currently, a study based on the simulation of the beam line is beeing carried out to quantify this effect. On top of this, there is an error ΔE on the mean energy E coming from the accuracy of the currents in the bending magnets of the energy-defining spectrometer. This errors can be approximated by the expression

$$\frac{\Delta E}{E} = 1.00209 + 0.233775/E + 9.07407 \cdot 10^{-6} \cdot E \tag{9.3}$$

where E is given in GeV.

9.3 Calibration constants derived from simulation

The Monte Carlo simulation of the beam test has been used to derive the calibration constants used in equation 8.10 for all beam energies and upstream material configurations. This was done by comparing the true energy deposit obtained from the calibration hits to the reconstructed cluster energy. To account for the differences observed between data and simulation the corrections and scaling factors mentioned in section 7.1 have been applied.

The linear fit on the correlation of presampler energy deposit to upstream energy deposit gives an offset that is almost independent from the beam energy (see figure 9.2). Only for the configuration with 75 mm Aluminum upstream, a slight drop with the energy can be observed. Most of the other points are (within errors) constant with the beam energy. Therefore the offset was fixed to one value for each material configuration. Figure 9.3 summarizes the constants that have been found for all beam energies and all material configurations. Figure 9.4 shows how the constants develop if upstream material is added. The back weight is shown in figure 9.5.

Energy [GeV]	Material [mm Al]	Run Nbrs	True Energy [GeV]±[MeV]	ϕ-range	η-range	electrons (estimated)
9	0	4160-4161	9.198 ± 2.55	0 - 0.02	0.375 - 0.4	30k
20	0	952-956	20.195 ± 2.74	0.005 - 0.013	0.355 - 0.37	20k
50	0	947-951	50.327 ± 3.58	0.01 - 0.002	0.36 - 0.38	27k
100	0	942-946	99.834 ± 5.61	0 - 0.17	0.36 - 0.38	25k
180	0	993-999	179.27 ± 9.33	0.003-0.007	0.377 - 0.383	15k
250	0	4089	251.323 ± 12.84	0.001-0.007	0.37 - 0.38	3k
9	25	4165-4167	9.198 ± 2.55	0 - 0.02	0.375 - 0.4	13k
20	25	1038-1039	20.163 ± 2.74	0.005 - 0.013	0.355 - 0.37	23k
50	25	1036-1038	50.30 ± 3.58	0.01 - 0.002	0.36 - 0.38	20k
100	25	1053-1056	99.834 ± 5.61	0 - 0.17	0.36 - 0.38	20k
180	25	1000-1007	179.27 ± 9.33	0.003-0.007	0.377 - 0.383	14k
250	25	4090	251.323 ± 12.84	0.001-0.007	0.37 - 0.38	3k
9	50	4168-4169	9.198 ± 2.55	0 - 0.02	0.375 - 0.4	22k
20	50	1040-1041	20.195 ± 2.74	0.005 - 0.013	0.355 - 0.37	10k
50	50	1032-1033	50.30 ± 3.58	0.01 - 0.002	0.36 - 0.38	17k
100	50	1050-1052	99.834 ± 5.61	0 - 0.17	0.36 - 0.38	10k
180	50	1008-1014	179.27 ± 9.33	0.003-0.007	0.377 - 0.383	10k
250	50	4091	251.323 ± 12.84	0.001-0.007	0.37 - 0.38	3k
9	75	4170-4172	9.198 ± 2.55	0 - 0.02	0.375 - 0.4	16k
20	75	1042-1043	20.163 ± 2.74	0.005 - 0.013	0.355 - 0.37	10k
50	75	1028-1031	50.30 ± 3.58	0.01 - 0.002	0.36 - 0.38	15k
100	75	1046-1048	99.834 ± 5.61	0 - 0.17	0.36 - 0.38	5k
180	75	1015-1023	179.27 ± 9.33	0.003-0.007	0.377 - 0.383	10k
250	75	4095	251.323 ± 12.84	0.001-0.007	0.37 - 0.38	3k

Table 9.2: Summary of data taken during the 2004 material study. The actual run numbers have the form 100xxxx, where xxxx is the number quoted in the table. The error on the beam energy given in the third column is the beam spread.

As expected, the calibration constant to correct for upstream energy loss (the offset, a, the slope, b, and the slope for the square-root term c) rise when more upstream material is added. The behavior of the slope b versus the energy depends on the amount of upstream material: For little upstream matter, it rises with the energy, but for more than $\sim$3 X_0 (in our setup this corresponds to a 50 mm aluminum plate plus the cryostat) this factor decreases with the energy. The two parameters to correct for the energy loss before the presampler (a and b) are of course correlated. If a is underestimated, b will be higher.

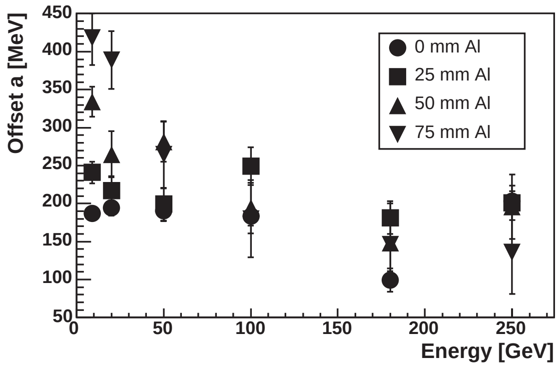

Figure 9.2: Offset obtained by a linear fit of the presampler energy to the upstream energy deposit.

9.3.1 Linearity achieved on simulated data

Figure 9.6 shows a cross-check of the calibration constants shown in figure 9.3. It has been made by applying the constants to the same simulation in order to reconstruct the beam energy. The figure contains the mean values (obtained by an asymetric gauss-fit) of the total reconstructed energy for all beam energies and material configurations.

9.3.2 Robustness of the method

At the beginning of data taking in ATLAS the upstream material will not be known with a precision of much better than 0.2 X_0. It is therefore necessary to check whether the proposed method is robust enough to be used at the very beginning of ATLAS.

Figure 9.7 allows to assess the robustness of the presented method against incorrect amount of upstream matter. It shows the linearity achieved by applying the constants derived from a simulation that assumes a too much or too little upstream material. If the upstream material description is wrong by 0.3 X_0, the measured energy is shifted by about 1% for energies higher than $\sim$30 GeV. The error increases towards smaller electron energy.

9.4 Corrections on data

9.4.1 Pedestal corrections

The data taken during the material studies in August 2004 suffer from instable temperature of the electronics that lead to a drift of the pedestals. The front end electronics were switched off after each run and re-started for the next one. Since the water cooling circuit was kept running, the Front-End boards cooled down quickly in the pause between the runs and heated up again when they were switched on. This problem could be solved by

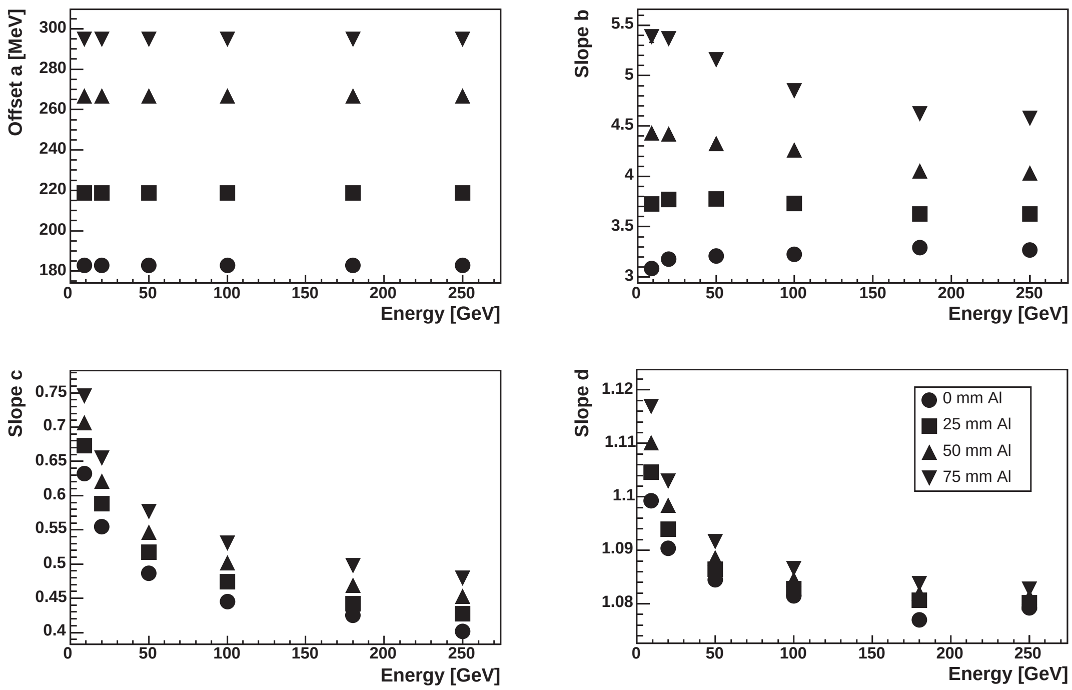

Figure 9.3: Calibration constants as defined in equation 8.10 for all beam energies and material configurations. The offset a has been fixed to one value for each material configuration.

using pedestal values based on random events during each run.

9.4.2 Ramp corrections

It turned out that four signal channels close to the point where the material studies have been carried out are connected to a problematic shaper. These channels are in the middle compartment and cover the upper half of the beam test module (ϕ >0) and the pseudo-rapidity range 0.375< η <0.4. For most of the energy points, the beam hits at slightly lower η. In this case, the two upper right cells of the 3 $\times$ 3 cluster are connected to the problematic shaper. The 180 GeV point hits at higher η: the hottest cell and the one above belong to this shaper.

The symptoms that have been observed are a significant higher ramp intercept than the neighbouring channels and that the slope and the intercept changes with time. It was found that including the ramp intercept for this cell in the reconstruction improves resolution for most of the energy points.

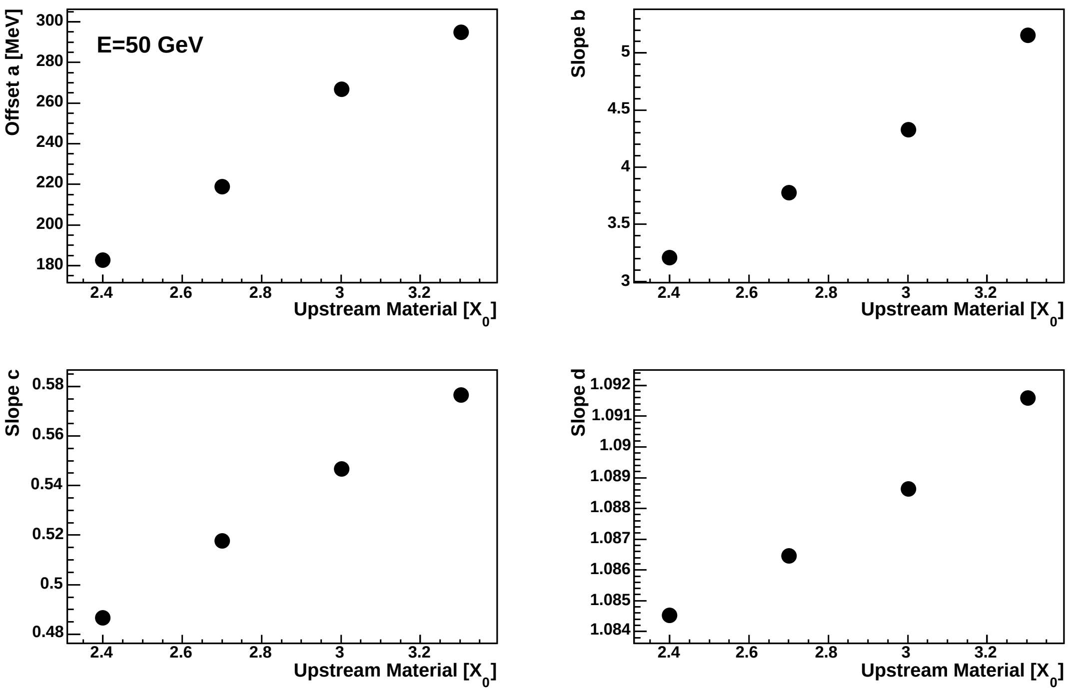

Figure 9.4: Calibration constants as defined in equation 8.10 for 50 GeV electrons and various upstream material thicknesses given in radiation lengths. The constants to correct for upstream energy loss as well as the sampling fraction correction are rising linearly when upstream material is added.

9.4.3 Reweighting of the presampler signal

As already pointed out in section 7.1, the simulated presampler signal deviates significantly from the measured one. Since the calibration parameters where derived from simulation this discrepancy directly influcences the result. To avoid this error, the measured presampler value was re-weighted to match the simulated one.

9.5 Linearity and resolution

The mean value of the measured energy has been determined by a prodecure including two gaussian fits, where the first one is used to determine the fit ranges for the second one. The first fit covers the full histogram, the second one covers only the range of +1/-2 sigma around the mean of the first one, in order to exclude the low-energy tails. The linearity and the resolution values given in this section are the mean and the sigma of the second fit.

Figure 9.8 shows the linearity obtained by applying the calibration constants and the

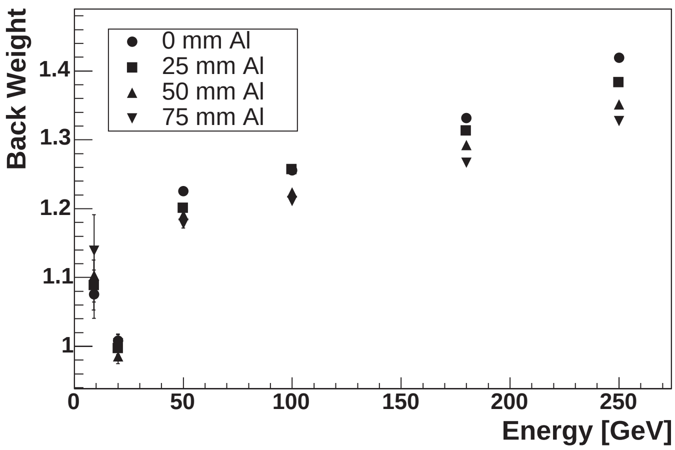

Figure 9.5: Weights on the back compartment to correct for downstream leakage for all beam energies and material configurations.

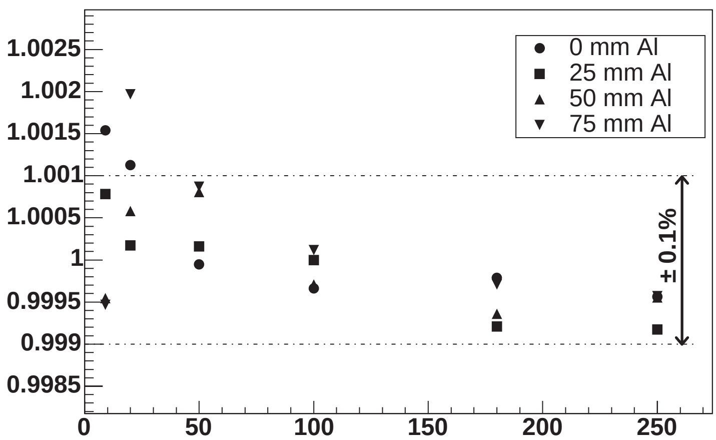

Figure 9.6: Cross-check of the calibration constants by applying them to the simulation. The largest deviation from linearity is observed for the low-energy points with 75 mm Aluminium with 0.25%, but most of the points are within 0.1%. The RMS of all points $7.3 \cdot 10^{-4}$.

corrections mentioned in the previous section to beam test data. All points for 50, 100 and 180 GeV are well within ±0.5%. Keeping the upstream material constant, they are even within ±0.05%.

At a beam energy of 250 GeV, all points are significantly lower. This is not surprising since the same behavior can be observed when comparing data and simulation (see figure

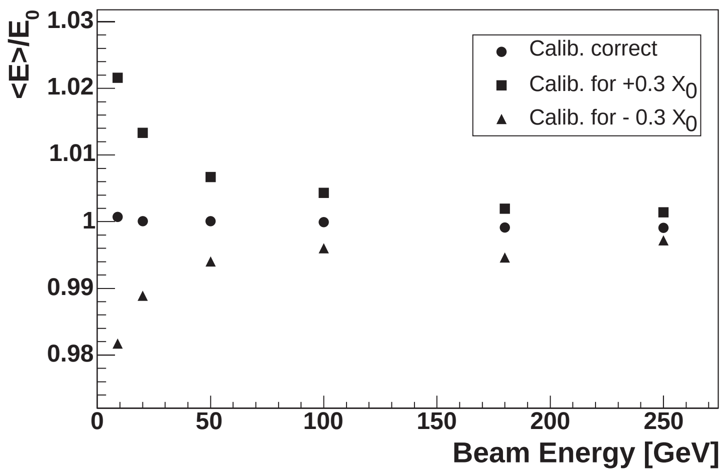

Figure 9.7: Estimate of the robustness of the calibration model using the beam test simulation. The circles give the linearity using the correct set of constants (identical to figure 9.6) while the sqares denote the linearity that would be achieved when the upstream material is overestimated by 0.3 X_0 or 25 mm of Aluminum. The triangles show the linearity if the upstream material is underestimated by the same amout.

7.3). Since we derive the calibration parameters from the simulation the achived linearity cannot be better than the description of the data by simulation. Also at very low energy (9 GeV) and more upstream material the situation gets worse.

In terms of RMS, the linearity changes from 0.68% (no additional upstream material) to 1.4% in case of 75 mm aluminium upstream of the cyrostat.

It has to be pointed out that the beam energy measurement was precise to approximately $5{\cdot}10^{-3}$ (solid lines in figure 9.8). Since basically all points lie within these errorbars it is impossible to judge whether the observed non-linearities stem from energy reconstruction or from the limited precision of the beam energy determination. Summarizing one could say that the calorimeter is perfectly linear within the error bars of the measurement. Event the points at 250 GeV and 9 GeV are mostly within the error bars.

Figure 9.9 shows the energy resolution obtained by the same method. Similar to the linearity, the points at 9 GeV are much worse than the others (scaled by the expected $1/\sqrt{E}$ dependency). As already discussed in chapter 8.1 (figure 8.3), the upstream energy loss for 9 GeV and 75 mm Aluminium upstream is as high as 20%. Correcting for such a high energy loss becomes very difficult. The obtained resolution and linearity are summarized in table 9.3.

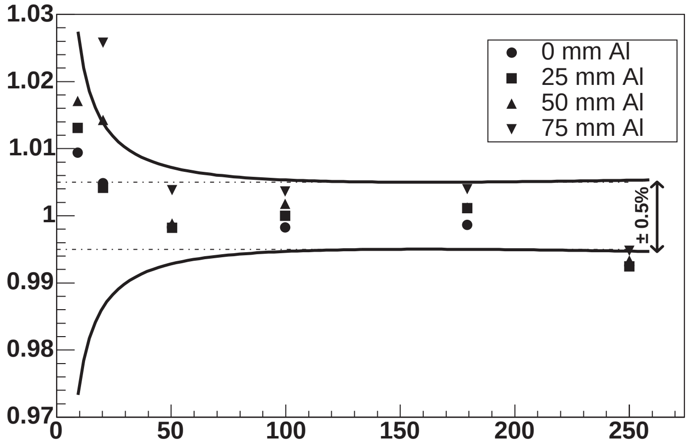

Figure 9.8: Linearity achieved on beam test data. The values are normalized to the 100 GeV/25 mm point. The solid lines indicate the error on the beam energy as given in equation 9.3.

Upstream Matter [X_0]	Resolution $\frac{\sigma_E}{E}$ [GeV]	Linearity (RMS) [%]
2.4	$\frac{11.4\%}{\sqrt{E}} \oplus \frac{0.2}{E} \oplus 0.55\%$	0.38 ± 0.5
2.7	$\frac{11.4\%}{\sqrt{E}} \oplus \frac{0.2}{E} \oplus 0.55\%$	0.39 ± 0.5
3.0	$\frac{11.2\%}{\sqrt{E}} \oplus \frac{0.2}{E} \oplus 0.56\%$	0.68 ± 0.5
3.3	$\frac{11.0\%}{\sqrt{E}} \oplus \frac{0.2}{E} \oplus 0.56\%$	1.0 ± 0.5

Table 9.3: Summary of the resolution and linearity obtained from bem test data between 20 and 250 GeV. The noise term of the resolution has been fixed 200 MeV, the sampling and the consant term where fitted on the points shown in figure 9.9. The error given to the linearity numbers comes from the uncertainty of the beam energy.

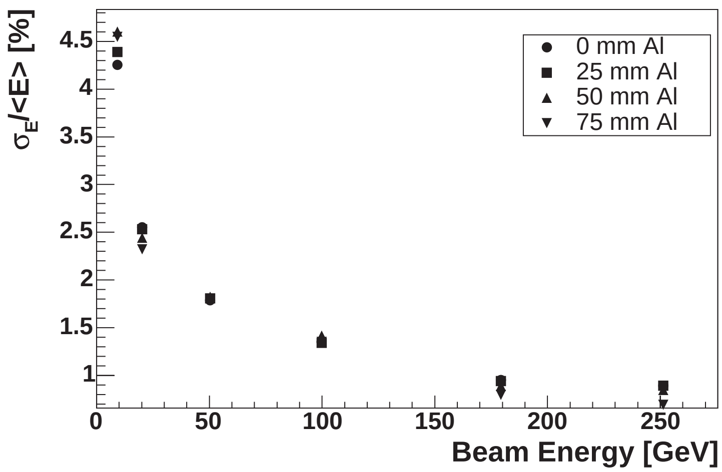

Figure 9.9: Resolution achieved on beam test data.

Chapter 10

Conclusions

The ATLAS Liquid Argon Calorimeter is one of the largest and most sophisticated calorimeters ever built. Its construction is meanwhile completed and the barrel part as well as one of the end-caps are already in place in the experimental hall.

The electronic calibration of the calorimeter (the energy measurement of a single cell) is now well understood and much of the necessary software was developed as part of this thesis work. It was successfully used and tested during the beam test and was constantly improved since then. Thanks to the careful design of the software, it was permanently available for reconstruction of beam test data.

To optimize the electron energy measurement with the calorimeter, the effect of inactive material upstream of the calorimeter as well as energy-dependent and impact-point dependent effects in the accordion itself have been studied in detail. It has been shown that the understanding of the physics of the EM shower development, in particular of the early shower is essential to achieve good energy linearity and resolution at the same time. The usage of a Monte-Carlo simulation of the detector allows to estimate the energy lost in inactive regions and to correct the energy measurement in the calorimeter itself effect by effect.

A energy reconstruction method that includes the following corrections was developed:

- Energy loss upstream of the presampler
- Energy loss in the inactive gap between presampler and strips compartment.
- Energy loss outside of the cluster and leakage behind the calorimeter.
- Energy and impact point dependent corrections to the energy scale of the accordion calorimeter itself.

The data obtained from the beam test that was carried out in summer 2004 at CERN was used to validate the Monte Carlo simulation and to check the proposed energy reconstruction method. It was found that the deviation of simulation and data is less than 1%.

Further improvement is expected with an improved understanding of the properties of the beam line. The high quality of the simulation justifies the strategy of deriving cluster calibration from the simulation.

A self-consistency check of this method on the simulation yields a linearity of better than 0.1%. Applying the method on beam test data yields an excellent linearity of 0.4% between 20 and 250 GeV with upstream material up to 2.7 radiation lengths, an amount of upstream material that is equivalent to the one in the central region of ATLAS. The resolution sampling term is 11.4%.

10.1 Outlook

The electron energy measurement with the ATLAS electromagnetic calorimeter is now well understood. The logical next step is to adapt the method for photons. Although a photon-shower in the calorimeter is very similar to a shower induced by an electron, the upstream energy deposit is different. The proposed calibration method is therefore not directly applicable for photons.

It will be also interesting to look in more detail at the beviour at very low energies. Data taken during the beam test allows to study the calorimeter response for energies as low as 1 GeV.

Appendix A

Liquid Argon Byte Stream Converters

This document aims to describe the Liquid Argon Byte Stream converter package as it was implemented for the 2004 combined beam test. The package is expected to evolve further to adapt to changes in the event format and the DSP code as well as to improve performance.

A.1 General Aspects

The Byte Stream converters for Liquid Argon Calorimeter data are Athena converters. They convert raw data from a persistent representation (the Byte Stream) into a transient one (the raw data objects in the transient event store). For some data objects, it is also possible to write data to a Byte Stream file (converting from a transient to a persistent representation). This allows for example to produce realistic Byte Stream files based on simulated data to test the performance of the trigger code.

Each data object that has to be converted has to have a converter class associated. These classes are relatively small, they just call member functions of other classes that are common for all data objects. Table A.1 lists the currently implemented converter classes and the data objects they produce.

Data object	Converter class	functionality
LArRawChannelContainer	LArRawChannelContByteStreamCnv	read/write
LArDigitContainer	LArDigitContByteStreamCnv	read/write
LArCellIDC	LArCellIDC_ByteStreamCnv	read
LArCalibDigitContainer	LArCalibDigitContByteStreamCnv	read/write
LArFebHeaderContainer	LArFebHeaderContByteStreamCnv	read
LArAccumulatedDigitContainer	LArAccDigitByteStreamCnv	read

A.1.1 ATLAS Byte Stream Format

The Byte Stream format produced by the ATLAS DAQ is described in [10]. One event in this format consists of a hierarchy of fragments that reflect the architecture of the readout chain (see figure A.1). Each fragment consists of a header and several sub-fragments. The top level fragment is the full-event fragment, it contains a fragment for each sub-detector. The sub-detector fragments contain ROS fragments consisting of ROB fragments which in turn are made up of ROD fragments. The ROD fragments are the lowest level in the fragment hierarchy. They consist of a header, a footer and an array of 32bit integers that contain the actual raw data read by the detector.

The event format library provided by the ATLAS TDAQ group is a software representation of the byte stream fragment structure. All the fragments and headers are represented by classes. Each fragment class has access methods for its header and to a vector of sub-fragments. The ROD fragment provides an iterator over the raw data block. Dereferencing this iterator yields a 32 bit unsigned integer.

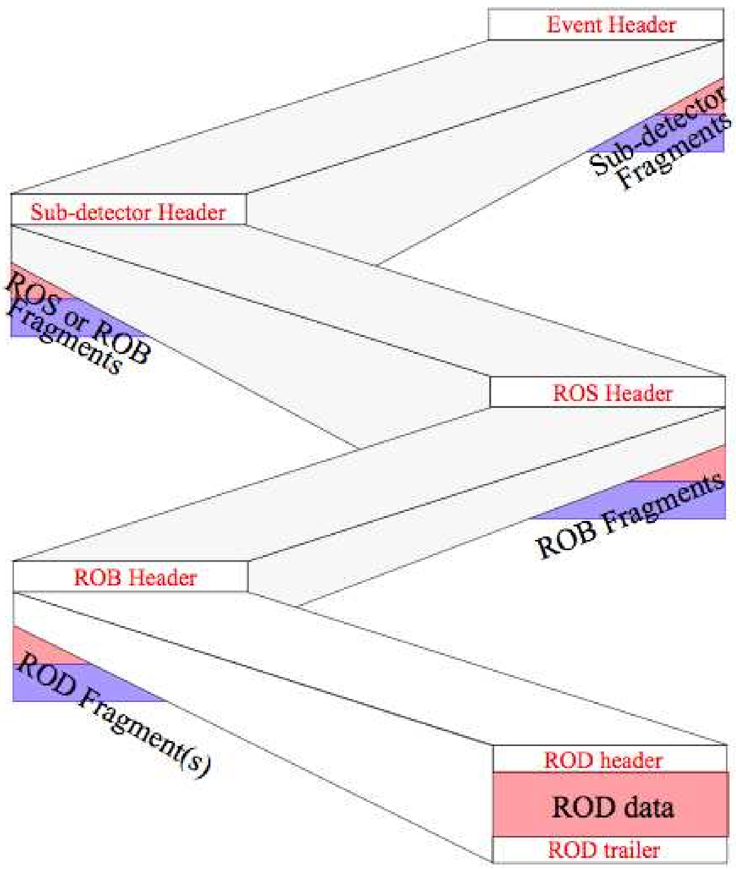

Figure A.1: Structure of the Atlas Byte Stream.

The reading (and writing) of the data file itself is done by the general Byte Stream conversion service that is common to all ATLAS sub-detectors. The input is not necessarily a file on a disk or tape but can also be a stream coming over the network (as for the LVL2 trigger). Reading an event with the Byte Stream Conversion Service results in a full event fragment in memory. The Liquid Argon Byte Stream converter retrieves either a pointer to a full event fragment or to the ROB fragments using the ROB identifier.

A.1.2 Liquid Argon Byte Stream Formats

How the data is encoded inside of the LAr ROD fragments depend on the code running on the DSP. This determines also which kind of data object can be retrieved from the raw data block. The field *Event Type* of the ROD header indicated the mode of the DSP and thus the encoding format, the field *Minor Version Number* indicates the version of the format. The LAr Byte Stream converter package contains one class for each block type and version to accommodate this variety of input format. These classes derive all from LArRodBlockStructure that defines the interface. Similar block types (or evolving versions) can also derive from each other, overloading only the functions that have changed. The functions for reading and writing (if appropriate) are part of the same class. There is no one-to-one correspondence between transient data objects (like LArDigits) and ROD block types. For example LArRawChannels and LArCells are made of the same raw data.

At the time of writing, the following RodBlockStructures have been implemented:

LArRodBlockTransparent decodes (and encodes) data written in transparent mode. In this mode, the DSP simply forwards the data as it comes from the FEB.

LArRodBlockPhysics decodes (and encodes) data written in physics mode. In this mode, the DSP calculates energy, time and a quality factor for each cell. This format can also contain the raw ADC samples for some (or all) channels of a FEB. Up to now, 4 versions (RodBlockPhysicsV0 to RodBlockPhysicsV2) have been implemented.

LArRodBlockCalibration is foreseen for calibration runs. This mode is very similar to the transparent mode. The only difference is that the DAC and delay settings for each FEB as well as a bit pattern that tells which cell has been pulsed is also part of the data. This mode is marked as *Detector Event Type* 7.

LArRodBlockAccumulatedDigits is also foreseen for calibration runs. In this mode the DSP accumulates the ADC samples taken with the same DAC and Delay settings. The data contains the sum and the sum of the squares of the ADC samples.

A.1.3 FEBs, ROD-boards and DSPs

The interconnection of FEBs, RODs and DSPs is schematically shown in figure A.2. Each ROD boards has eight optical inputs (GLINK), each connected to one FEB. The ROD board has four daughter-boards, each carrying two DSPs. In normal mode as it was done in the beam test, each DSP reads the data from one FEB. In staging mode, one DSP serves two FEBs. output of two DSP is concatenated by a Output Controller and set via another optical link (SLINK) to the ROS.

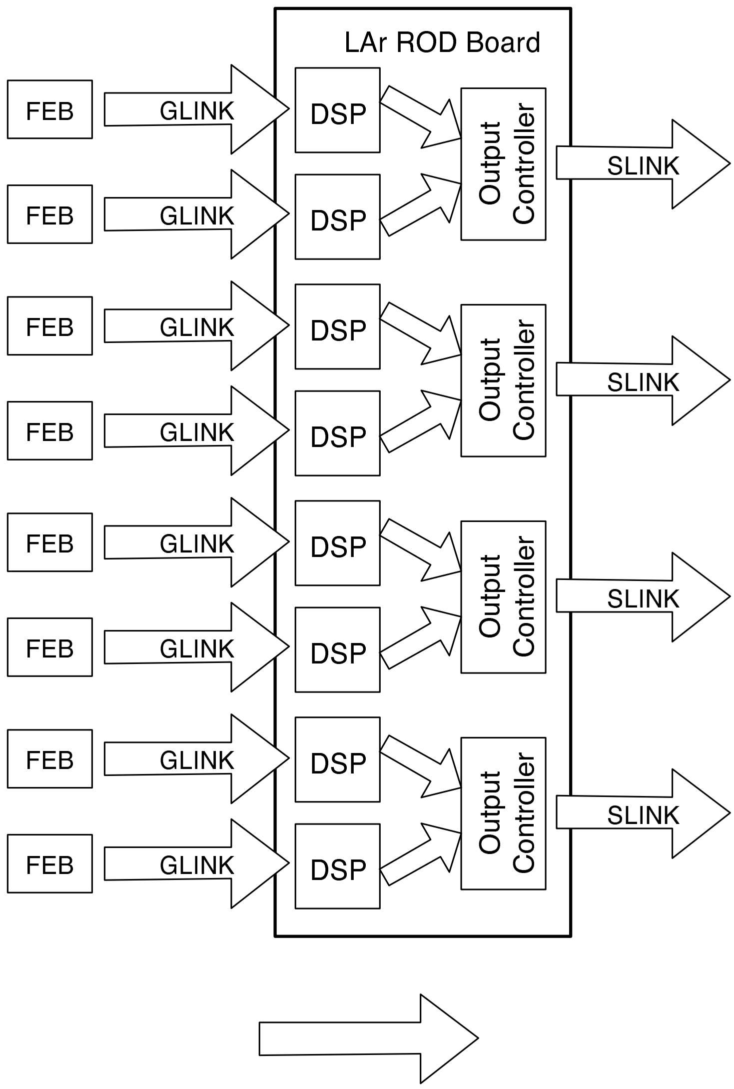

Figure A.2: Connection of FEBs and DSPs in non-staging mode. There is one DSP per FEB, the output of two DSPs is merged and send to one ROS input.

What is called a ROD fragment in the context of the Byte Stream format is actually what comes over the SLINK. So one physical LAr ROD board produces four TDAQ ROD fragments. Each of these fragments contains the data of two FEBs. This has the implication that part of the ROD header shows up twice in the ROD block, because this header is jointly produced by the DSPs and the output controller. In addition to the ROD header, the DSP writes some header words that depend on the block type before the actual data block. Table A.1.3 shows the final composition of the LAr ROD fragment. The event format library interprets the first nine words as ROD header, and the last three words as ROD footer. The remaining words are treated as data words. It is up to the LAr byte stream converter to interpret them correctly.

Start of header marker	
Header size	
Format version number	
Source Identifier	
Run Number	ROD header
Level 1ID	
Bunch Crossing ID	
Level 1 trigger type	
Detector event type	
DSP format dependent header word	
....	
DSP format dependent header word	
Data (first FEB)	
....	
Data (first FEB)	
Format version number	
Source Identifier	
Run Number	
Level 1ID	
Bunch Crossing ID	ROD Data block
Level 1 trigger type	
Detector event type	
DSP format dependent header word	
....	
DSP format dependent header word	
Data (second FEB)	
....	
Data (second FEB)	
Number of status elements	
Number of data word	ROD Footer
Status block position	

Table A.1: Format of the Liquid Argon Calorimeter ROD fragment. Each line corresponds to a 32 bit unsigned integer. The format of the data words and the DSP header words depends on the block type (defined by the *Detector Event type word*) and have in general they own substructure.

A.2 Program flow

A.2.1 Reading of data objects in plain containers

The objects LArDigits are LArCalibDigits are stored in plain containers that derive from DataVector. These containers do not have any sub-structure and do not imply any order of the objects they contain.

If an object of a certain type is requested from StoreGate that has a converter registered and cannot be found in the store, the converter gets triggered. StoreGate calls the function createObj(IOpaqueAddress* pAddr, DataObject*& pObj) of the converter. The IOpaqueAddress contains information like the StoreGate key that has been used to retrieve the object from the store. This is important for objects like LArDigit or LArCalibDigit where the key indicates the gain. The createObj function gets the Full Event Fragment from the Byte Stream Conversion Service and creates the requested data object (the container). To fill the container, it calls the function:
LArRawDataContByteStreamTool::Convert(const RawEvent* re, digitContType* digit_cont, CaloGain::CaloGain gain)
where digitContType is a template variable that can be LArDigitContainer, LArCalibDigitContainer or something similar. If a converter is added for a new data type, an instance of class LArRawDataContByteStreamTool for this type has to be declared in the file LArByteStream_entries.cxx. A peculiarity of the variable gain is that the value CaloGain::LARNGAIN indicates free gain mode. The converter produces the requested container class in any case. If an error occurs during the conversion process (e.g. the data is not present), the container remains empty.

The LArRawDataContByteStreamTool uses the functionality of the event format library to iterate over the fragment structure of the event. Whenever it hits a Liquid Argon Calorimeter ROD fragment (recognizable by its source identifier), it creates a vector of 32 bit unsigned integers and copies the data block of the ROD (as shown in table A.1.3) into this vector. In version 3 of the event format library, the copy step can be omitted, since it provides direct access to the ROD data blocks. The ROD header as well as the obtained data block are now passed to the LArRodDecoder for further processing.

One of the responsibilities of the LArRodDecoder is to determine the block type according to the *Detector Event Type* and call the appropriate version of the LArRodBlockStructure. During initialization, the LArRodDecoder builds a two-dimensional array (vector of vector) of pointers to LArRodBlockStructures. The lines of the matrix correspond to the block type, the columns to the version.

Since this function fillCollection creates the requested data object, there must be a specialized function for each kind of object. Parameters given to this function are the vector containing the ROD data block, the container that is to be filled and the requested gain. The first step these functions do, is to call the private member function prepareBlockStructure that picks the right element of the matrix of RodBlockStructures and sets the requested gain. The RodBlockStructure interface is described in the next section. The main part of the fillCollection function are two nested loops, the outer one runs over FEB blocks inside a ROD block (usually two), the inner one loops over the channels of a FEB (usually 128). The FEB identifier is determined once per FEB in the outer loop, the channel identifier is given by the running index of the inner loop. The full online channel identifier is built using these two numbers with help of the LArOnlineID helper class. In the inner loop, the content of the data object is requested from the RodBlockStructure, the data object is constructed and pushed into the container.

The requested gain and a reference to the container that is to be filled is passed through all levels of the decoding process.

The fillCollection function for the LArFEBHeader object works slightly differently: No loop over channels is required and the necessary data is retrieved either from the ROD header or via special functions of the LArRodBlockStructure.

Reading Calibration Digits

Originally it was foreseen to write the calibration board configuration (DAC, delay, pulse-pattern) into the header of each FEB block. At least for the 2004 beam test this was not done; calibration runs have been taken in transparent mode (yielding LArDigits). The calibration board configuration has to be obtained from the conditions database. There is an algorithm to produce a LArCalibDigitContainer out of an LArDigitContainer but this involves a loop over all channels for each event and is therefore rather slow. To overcome this, this functionality was included in the LArRodDecoder class itself. If calibration digits are requested but the invoked RodBlockStructure is not the one for calibration, the LArRodDecoder obtains the missing information to fill the relevant members of the LArCalibDigit class. This involves using LArCablingService to get the mapping of read-out lines and calibration lines and the LArCalibParams data class that has to be retrieved from the conditions database. Given a calibration line identifier, this class can return the DAC, the delay and the pulse-pattern for each event.

Ad hoc fixes

There are two not-so-nice fixes implemented in the Liquid Argon Byte Stream converter to overcome problems that have been encountered during the beam test.

ADC Sample Rearrangement If a FEB runs in free gain mode, the ADC samples are ordered in a way that the one used for the automatic gain selection comes first. In most cases this is the third sample. So the order of ADC samples would 2 0 1 3 4 instead of 0 1 2 3 4. Unfortunately, this cannot be derived from the data format used in the beam test and has to be put in as job option *FirstSample* to the LArRodDecoder. The number given (the index of the sample that has been put at the first place) is passed to the LArRodBlockStrucutre where the ADC samples get rearranged to match the expected order.

FEB exchange During the 2004 beam test, a couple of runs have been taken with wrong Front End board identifiers in the data (human error). The FEB IDs of a Back FEB and a Front FEB have been exchanged. To work around this problem, the three job options have been added to the LArRodDecoder. If the boolean job option FebExchange is set to true, than the two FEB IDs given as *FebId1* and *FebId2* are exchanged by the LArRodDecoder before the online identifier for the LArDigit or LArCalibDigit is created.

A.2.2 Reading of data objects in identifiable containers

Containers like the LArRawChannelContainer or the LArCell_IDC do not hold data objects directly. They contain a so-called collections which contain the data objects for a certain region of the calorimeter. These collections are themselves registered to StoreGate. Each collection corresponds to one ROB block in the ByteStream fragment hierarchy. The actual decoding of Byte Stream data takes place only if one the collections is retrieved from StoreGate. This means that not necessarily the full event is decoded but only the cells of some ROB blocks. This is crucial for time-critical applications like the high-level trigger.

The converter classes for this kind of container produces only the top level container and its collection-substructure. The converter for the collections is a generic converter (not specific to the Liquid Argon Calorimeter) called CollectionByteStreamCnv that takes a decoding tool as template argument, in our case the LArRawChannelCollByteStreamTool. This tool is itself a template class, with the type of collection (LArCell or LArRawChannel) as template argument. The most important function of this tool is
convert(VROBDATA& vRobData, COLL*& coll, const unsigned long* ipar, MsgStream& log).

Among the parameters are a reference to the ROB block that is to be decoded and a pointer to the collection that is to be filled. The tools does not have to search the whole ByteStream structure as it is done for LArDigits, it decodes only the RODs that are part of the give ROB. Similar to the reading of objects in plain containers, the ROD datablock is copied to a vector of integers and a function of the LArRodDecoder::fillCollection is called that loops over all FEBs in a ROD and all channels in a FEB, creates the requested object and adds them to the collection. The necessary values are obtained using the flavor of RodBlockStructure matching the data block type. To produce a single channel or cell, a specialized function is used. The one for LArRawChannels simply uses the new-operator, the one for LArCells it invokes the same cell making too that is used in the standard offline reconstruction to produce LArCells out of LArRawChannels.

A.2.3 Writing

Writing of data objects to a byte stream file is a considerably more complicated operation than reading. Two or even more different kinds of data objects can end up in the same ROD fragment and it is not known if and in which order the converters for this data objects are called. Furthermore, the transient data objects are in general not sorted, so they need to be sorted according to their Front-end board and channel number.

The start of the program flow is again the converter class. The function
createRep(DataObject* pObj, IOpaqueAddress*& pAddr)
gets triggered at the end of each event if the associated object is to be persistified as Byte Stream. Usually there are many objects written to the Byte Stream (e.g. raw data from different subdetector, or LArRawChannels together with LArDigits). The mentioned function is called for all these objects in an arbitrary order, eventually adding new fragments to the Byte Stream structure. The class that manages this is the FullEventAssember of the ByteStreamCnvSvc. The createRep method of the Liquid Argon Byte Stream Converters obtains the FullEventAssembler and thus any previously build ROD fragments. It retrieves also the data object to be persistified from the store and calls a function of the LArRawDataContByteStreamTool:
WriteLArDigits(const LArDigitContainer digit_cont, FullEventAssembler<Hid2RESrcID> fea)
WriteLArCalibDigits(const LArCalibDigitContainer digit_cont,
FullEventAssembler<Hid2RESrcID> fea)
WriteLArRawChannels(const LArRawChannelContainer CannelCont,
FullEventAssembler<Hid2RESrcID> fea)
There is a dedicated write function for each data object, no templates are used.

The block type that should be emulated is set as a jobOption of this tool. No versioning is foreseen at this point. Depending on the jobOption, one of the LArRodBlockStructue classes is constructed during initialization. The pointer to this class is passed to the LArRodEncoder class which holds it as a static variable. All ROD fragments in one job are encoded with the same block type.

Before writing, the channels need to be sorted according to the ROD and the FEB they belong to. To do so, a class called LArRodEncoder has been introduced. In contrast to the ROD-decoder class, this is not a AlgTool. The write-functions of the LArRawDataContByteStreamTool build a STL map of LArRodEncoder objects, one each ROD. The ROD identifier serves as key for the map. These LArRodEncoder-instances keep internally a STL map to separate channels belonging to different FEBs. The key of this map is the FEB identifier, its payload is the following structure:

```
struct FebData_t {
    std::vector<const LArRawChannel*> vLArRC;
    std::vector<const LArDigit*> vLArDigit;             //Free gain
    std::vector<const LArDigit*> vLArDigitFixed[3];     //3 fixed gains
    std::vector<const LArCalibDigit*> vLArCalibDigit[3];//3 fixed gains
};
```

Each Liquid Argon Calorimeter data type that can be written to Byte Stream has an entry, fixed-gain data objects have an array of three entries. The map is filled by the function LArRodEncoder::add with a pointer to the data objects as parameter (and a gain-parameter in case of fixed-gain data). The data inside the vectors get also sorted (according to their FEB-channel number). Since the order of the channels inside a FEB block depends on the block type the sort-method is part of the LArRodBlockStructure.

After all channels are added to their respective LArRodEncoder instance, the LArRawDataContByteStreamTool iterates over the map of RODs, retrieves a pointer each ROD from the FullEventAssembler and calls the fillROD function of each instance of the LArRodEncoder with the pointer to the ROD data block as paramater. The ROD block is not necessarily empty, it might already contain some data from a different data object (e.g. LArDigits in another gain). The LArRodEncoder tries to add all elements in it internal map to the ROD block, provided the chosen LArRodBlockStructure supports writing of the concerned data type. The writing-functions of the LArRodBlockStructure must be able to deal with a partially filled ROD block.

A.3 Interface of the LArRodBlockStructure base class

The LArRodBlockStructure classes are only loosely coupled to the Athena framework. The reason for this is that they could be used also in another context, e.g. for ROS level monitoring. Though, this was never done and there are some dependencies on Athena services, like the message service.

A.3.1 Treatment of the FEB header

Each FEB block in the ROD header starts with a header that is specific to the data format type. It consists of 32 bit integers or pairs of 16 bit integers. This header contains important information like the FEB identifier and a pointer (offset) to the data block(s). Each LArRodBlockStructure class has internally an enum that lists the elements of the header. Thus, the members of the enum give automatically the index of the header words. Such an enum could look like this:

```
enum {
    NWTot,             // Number of words in this FEB block
    NWTot_h,
    FEBID,             // FEB identifier
    FEBID_h,
    FEB_SN,            // FEB serial number
    FEB_SN_h,
    RawDataBlkOffset, // Offset to the start of the Raw Data block
    RawDataBlkOffset_h,
    NGains,            // Number of gains
    NSamples,          // Number of samples
    endtag
  };
```

Each element of the enum corresponds to a 16 bit integer. If a header word is saved on 32 bits, a second dummy instance is added (indicated by the postfix '_h'). The last element of the enum shall be called endtag, this indicates the size of the header. The LArRodBlockStructure base class provides helper functions to get and set header elements. These functions are declared as *protected*, so they can be used by derived classes.

inline uint16_t getHeader16(const unsigned n) const
inline uint32_t getHeader32(const unsigned n) const
Reads a 16 bit (or 32 bit respectivly) header word. As parameter, one element of the enum shall be used. E.g. getHeader32(FEBID) returns the FEB identifier. These two function must not be used while encoding a fragment!

In case of encoding, the functions
inline void setHeader16(const unsigned n, const uint16_t w)
inline void setHeader32(const unsigned n, const uint32_t w)
set the header word indicated by n to the value w. The functions
inline uint16_t getVectorHeader16(const unsigned n) const
inline uint32_t getVectorHeader32(const unsigned n) const
read them back. These four function must not be used while decoding a fragment!

A.3.2 Functions for decoding

virtual inline void setFragment(const std::vector<uint32_t>& fragment)
This function is implemented in the base class itself. It simply caches a pointer to the first element of the vector *fragment* in the private data member m_Fragment and the size of the vector as m_TotalSize. This function has to be called before any other function.

virtual bool nextFEB(RODHeader* fullHeader=NULL)
Jumps to the next FEB in the current ROD block. It updates the m_Fragment data member so that subsequent calls to the header-reading function return the value of the current FEB. If no more FEB blocks are present, it returns false. If a ROD header is given as parameters, the function checks whether the ROD fraction of the header produced by the second DSP matches the first one.

virtual void resetCounters()
Resets all internal counters (used by the functions to the raw data) to zero. This function is called by the constructor and the nextFEB function.

virtual inline uint32_t getFEB_ID() const
Returns the FEB identifier of the current FEB as stored in the FEB header.

The following functions read the actual data block. They use internal counters and return always the next channel in the block. They return false as soon as they are no more channels available. The implementation of these functions in the base class returns an error message like *"...not implemented in this version of LArRodBlockStructure"*. This occurs for example if one attempts to read LArRawChannels from a byte stream file that contains only calibration data. The parameters of these functions are all references to the variables that are to be filled. If DSP formats with new data types appear, the interface has to be extended.

virtual inline int getNextEnergy(int& channelNumber, int32_t& energy,int32_t& time,int32_t& quality,uint32_t& gain)
Reads the quantities of the LArRawChannel data class.

virtual int getNextRawData(int& channelNumber, std::vector<short>& samples, uint32_t& gain)
Reads raw ADC samples.

virtual inline bool getPulsed(unsigned channelNumber) const
Tells if a channel is pulsed. (Only possible if the calibration board information is stored in the Byte Stream.)

virtual inline uint16_t getDAC() const
Returns the DAC value. (Only possible if the calibration board information is stored in the Byte Stream.)

virtual inline uint16_t getDelay() const
Returns the delay value. (Only possible if the calibration board information is stored in the Byte Stream.)

virtual inline uint16_t getNTrigger() const
Returns the number of triggers. (Only possible if the calibration board information is stored in the Byte Stream.)

virtual uint8_t getTDCPhase() const
This function is only useful for data converted from the 2002 beam test to Byte Stream Format. It returns the particle phase necessary to pick the right set of Optimal Filtering coefficients.

int setGain(const int GainValue) const
In case of raw data written in fixed gain mode, this function sets the requested gain for subsequent calls to GetNextRawData.

The following functions are used to retrieve DSP and FEB header words. They are largely self-explanatory.
virtual uint32_t getNumberOfWords() const
virtual uint32_t getNumberOfSamples() const
virtual uint32_t getNumberOfGains() const
virtual uint32_t getRadd(uint32_t adc, uint32_t sample) const
virtual uint32_t getCtrl1(uint32_t adc) const
virtual uint32_t getCtrl2(uint32_t adc) const
virtual uint32_t getDspCodeVersion() const
virtual int32_t getDspEventCounter() const

A.3.3 Functions for encoding

A FEB data block can contain several sub-blocks of data, e.g. raw data in different gains or raw data and reconstructed data. When writing to a Byte Stream file, the converters for the different data objects are called one after the other. Therefore the LArRodBlockStructure has to be able to extend partially filled ROD fragments. During the encoding process, the various sub-blocks are kept as private vector of integers and merged into FEB and ROD blocks at the end.

void initializeFragment(std::vector<uint32_t,DF_ALLOCATOR<uint32_t> >& fragment)
Caches a pointer to the fragment and breaks it down into FEB blocks in case it is not empty.

virtual void initializeFEB(const uint32_t id)
Fills (or at least reserves) the header of each FEB.

The next three function set header words:
virtual void setNumberOfSamples(const uint8_t n)
virtual void setNumberOfGains(const uint8_t n)
virtual void setTDCPhase(const uint8_t n)

virtual void setNextEnergy(const int channel, const int32_t energy, const int32_t time, const int32_t quality, const uint32_t gain)
Sets the next channel in the raw data block. The channels must come in the right order.

virtual void setRawData(const int channel, const std::vector<short>& samples, const uint32_t gain)
Sets the next channel in the free-gain raw data block. The channels must come in the right order.

virtual void setRawDataFixed(const int channel, const std::vector<short>& samples, const uint32_t gain)
Sets the next channel in the fixed-gain raw data blocks. The channels must come in the right order.

The next four functions set calibration board parameters in the FEB-header:
virtual void setDAC(const uint16_t DACValue)
virtual void setDelay(const uint16_t DelayValue)
virtual void setPulsed (const unsigned channelNumber)
virtual void setNTrigger (const uint16_t NTrigger)

virtual void finalizeFEB()
Writes all filled sub-blocks one after the other into the FEB blocks. The offsets to the starting points of each sub-block is stored in the header.

virtual void concatinateFEBs(RODHeader* fullHeader=NULL)
Concatenates all FEB blocks to one ROD block.

The following functions help the LArRodEncoder class determine the abilities of a particular version of a LArRodBlockStructure.
virtual bool canSetEnergy()
virtual bool canSetRawData()
virtual bool canSetRawDataFixed()
virtual bool canSetCalibration()
virtual bool canSetNTrigger()

A.3.4 Helper functions

virtual void sortDataVector(std::vector<const LArRawChannel*>&)
virtual void sortDataVector(std::vector<const LArDigit*>&)
virtual void sortDataVector(std::vector<const LArCalibDigit*>&)
Sort vectors containing the data objects according to their order in a FEB block.

virtual void dumpFragment()
A debugging tool.

inline uint32_t RawToOfflineGain(const uint32_t gain) const
inline uint32_t OfflineToRawGain(const uint32_t gain) const
Converts the online definition of gain into the offline one and vice-versa.

inline void setFirstSample(const int rearrangeFirstSample)
Used for re-arranging the ADC samples. The function sets the index of the first sample. (See section A.2.1.)

inline void setBit(uint32_t *const p, const unsigned chan)
inline int getBit(const uint32_t *const p, const unsigned chan) const
Get and set single bits in 128 bit mask.

A.4 JobOption syntax

A.4.1 Reading

In order to read a raw data file with Athena, one has to invoke the generic ByteStreamCnvSvc as well as the EventSelector that access the physical file and tell them the location and the name of the file (either on tape or on disk). Secondly, one has to load the library containing the here described Liquid Argon Byte Stream Converter and declare the data types that are to be read from Byte Stream.

A job option fragment to read LArDigits could look as follows:

```
include( "ByteStreamCnvSvc/TBEventSelector_jobOptions.py" )
ByteStreamInputSvc=Service("ByteStreamInputSvc")
ByteStreamInputSvc.InputDirectory +=
```

```
  ["/castor/cern.ch/atlas/testbeam/combined/2004"]
ByteStreamInputSvc.FilePrefix += [daq_SFI-51_combined"]
ByteStreamInputSvc.RunNumber = [123456]

theApp.Dlls += [ "LArByteStream"]
ByteStreamAddressProviderSvc = Service( "ByteStreamAddressProviderSvc" )
ByteStreamAddressProviderSvc.TypeNames += ["LArDigitContainer/HIGH"]
ByteStreamAddressProviderSvc.TypeNames += ["LArDigitContainer/MEDIUM"]
ByteStreamAddressProviderSvc.TypeNames += ["LArDigitContainer/LOW"]
Bytestreamaddressprovidersvc.TypeNames += ["LArDigitContainer/FREE"]

if GainKey=="FREE":
  ToolSvc.LArRodDecoder.FirstSample=2
```

In the beginning, another job option fragment is included that does all the basic steps followed by the location of the raw data file. The actual file name is composed of three elements: a path, a prefix and a run number. All three are in fact vectors, if more than one element is given, the EventSelector iterates over the vector and processes all files. The complete file name and path in the example give above would be

```
/castor/cern.ch/atlas/testbeam/combined/2004/
daq_SFI-51_combined_123456_file01.data
```

where the last two digits of the name are a running number since a run can consist of more the one file. Alternatively, the input file name can be given by the syntax:

```
ByteStreamInputSvc.inputFiles=["FullFileName"]
```

The second part of the job option fragment registers the converters for certain data objects with the syntax:

```
ByteStreamAddressProviderSvc.TypeNames += ["<DataObject>/<SG Key>"]
```

SG key indicates the StoreGate key. An attempt to retrieve a data object with another key as give here will result in an error. The key can be replaced by an asterisk ('*') to indicate that all keys are accepted.

The last line of the example given above tells the converter to re-arrange the ADC samples because the FEB put the third one at the first place.

A.4.2 Writing

Similar to the reading case, one needs to invoke the generic conversion service and output stream as well as the Liquid Argon Calorimeter specific converter. A job option fragment to write LArRawChannels and LArDigits could looks as follows:

```
# ----------- JobOptions to write ByteStream ----------
# --- Necessary services....
theApp.Dlls   += [ "ByteStreamCnvSvc" ]
theApp.ExtSvc += [ "ByteStreamCnvSvc" ]
theApp.ExtSvc += [ "ByteStreamFileOutputSvc" ]
ByteStreamCnvSvc = Service( "ByteStreamCnvSvc" )
ByteStreamCnvSvc.ByteStreamOutputSvc ="ByteStreamFileOutputSvc"
theApp.OutStream =["StreamBS"];
theApp.OutStreamType ="AthenaOutputStream";
StreamBS = Algorithm( "StreamBS" )
StreamBS.EvtConversionSvc="ByteStreamCnvSvc"


# ----------- JobOptions to write LArContainers to ByteStream
ToolSvc.LArRawDataContByteStreamTool.DSPRunMode=4
theApp.Dlls   += [ "LArByteStream", "LArRawUtils"]

StreamBS.ItemList +=["LArRawChannelContainer#LArRawChannel"]
StreamBS.ItemList +=["LArDigitContainer#HIGH"]
StreamBS.ItemList +=["LArDigitContainer#MEDIUM"]

ByteStreamFileOutputSvc.OutputFiles = ["OutputFileName.data"]
```

The block type that is to be generated is given as job option *DSPRunMode* to the LArRawDataContByteStreamTool. The container that is to be persistified is determined by the syntax

```
StreamBS.ItemList +=["<DataObject>#<SG key>"]
```

similar to the reading, the wildcard '*' can be used to replace the StoreGate key.

Appendix B

Longo Sestili Formula

In their original paper [16], Longo and Sestili present the following formula for the number of charged particles crossing a plane t=const. where t is the depth given in Radiation Lengths:

$$N(t) = A \cdot (t)^{a-1} e^{-bt} \tag{B.1}$$

The energy deposit in an infinitisimal volume around this plane is then given by the number of particles $N(t)$ times the energy deposit of a single charged particle dE_e (that is assumed to be the same for all particles)

$$\frac{dE}{dt} = \frac{dE_e}{dt} \cdot N(t) \tag{B.2}$$

and therefore

$$\frac{dE}{dt} = \frac{dE_e}{dt} \cdot A \cdot (t)^{a-1} e^{-bt} \tag{B.3}$$

We request now that the integral of B.3 from 0 to infinity must yield the beam energy E_0:

$$\int_0^\infty \frac{dE}{dt} dt = \int_0^\infty \frac{dE_e}{dt} \cdot A \ (t)^{a-1} e^{-bt} dt = E_0 \tag{B.4}$$

To solve this integral, we substitute $bt = x$ and use the definition of the gamma function

$$\Gamma(a) = \int_0^\infty (x)^{a-1} e^{-x} dx \tag{B.5}$$

With $dt = \frac{dx}{b}$, equation B.4 becomes

$$\int_0^\infty \frac{dE}{dt} dt = \frac{\frac{dE_e}{dt} \cdot A}{b \ b^{a-1}} \cdot \underbrace{\int_0^\infty (x)^{a-1} e^{-x} dx}_{\Gamma(a)} = E_0 \tag{B.6}$$

From this equation one can derive a constraint for A:

$$A = E_0 \frac{b \ b^{a-1}}{\Gamma(a) \ \frac{dE_e}{dt}} \tag{B.7}$$

Substituting A in equation B.3, gives

$$\frac{dE}{dt} = \frac{E_0 b}{\Gamma(a)} (bt)^{a-1} e^{-bt} \tag{B.8}$$

this is the formulation that can be found in the Particle Data Handbook.

Appendix C

Properties of the relevant materials

The following table lists the properties of the important materials used in the construction of the calorimeter. The values have been taken from [8] or calculated using values found therein. The effective values for the accordion calorimeter include all materials used (Kapton, steel-coat, Copper electrode, Prepreg) and the thicknesses mentioned in [2].

Material	Liquid Argon	Lead	Aluminum	Accordion (η <0.8) (effective)
Density [g/cm^3]	1.396	11.35	2.66	4.18
Radiation length [cm]	14	0.56	8.9	2.02
dE/dx [MeV/cm] (MIP)	2.1	12.73	4.36	5.3
dE/dx [MeV/X_0] (MIP)	29.5	7.13	38.8	10.7
Critical Energy (e^-) [MeV]	38.13	7.79	42.55	-
Molière Radius [cm]	7.79	1.53	11.97	3.66

Table C.1: Material properties

Bibliography

[1] Cern Web Site: www.cern.ch

[2] The ATLAS Liquid Argon Collaboration, Liquid Argon Calorimeter Technical Design Report, CERN/LHCC/96-41, 1996

[3] The ATLAS Collaboration, ATLAS Calorimeter Performance Technical Design Report, CERN/LHCC/96-40, 1997

[4] The ATLAS Muon Collaboration, ATLAS Muon Spectrometer Technical Design Report, CERN/LHCC/97-22, 1997

[5] The ATLAS Collaboration, Calorimeter Performance Technichal Design Report, CERN/LHCC/96-10, 1997

[6] The ATLAS Collaboration, ATLAS Detector and Physics Performance Technical Design Report, CERN/LHCC/99-15, May 1999

[7] The ATLAS Collaboration, ATLAS Computing Technical Design Report, CERN/LHCC/, May 2005

[8] Particle Data Group, Review of Particle Physics, Physical Review D, 2002

[9] GEANT4: A Simulation Toolkit, S. Agostinelli et al, Nuclear Instruments and Methods in Physics Research, NIM A 506 (2003), 250-303.

[10] C. Bee, et al., The raw event format in the ATLAS Trigger & DAQ, Atlas internal note ATL-DAQ-98-129, 2004

[11] ATLAS Electromagnetic Calibration Strategy, http://atlas.web.cern.ch/Atlas/GROUPS/LIQARGSOFF/CalibnAlignmnt/EM_calibration.pdf

[12] B. Di Girolamo, ATLAS Barrel Combined Run in 2004 Test Beam Layout, Atlas internal note, ATC-TT-IN-0001, 2004

[13] J. Spanggaard, Delay Wire Chambers, SL-Note-98-023 (BI), 1998

[14] W.E. Cleland, E.G. Stern, Signal Processing considerations for liquid ionization calorimeters in a high rate environment, Nuclear Instruments and Methods in Physics Research A 338 (1994) 467-497

[15] W. Walkowiak, Drift Velocity of Free Electrons in Liquid Argon, Atlas internal note ATL-LARG-99-008, 1999

[16] E. Longo, I. Sestili, Monte Carlo Calculation of Photon-initiated Electromagnetic Showers in Lead Glass, Nuclear Instruments and Methods 128 (1975) 283-307

[17] R. Wigmans, Calorimetry: Energy Measurement in Particle Physics, Clarendon Press, Oxford, 2000

[18] Aubert, B. et. al, Construction, assembly and tests of the ATLAS electromagnetic barrel calorimter, CERN-PH-EP/2005-034, Submitted to NIM, 2005

[19] N. Kerschen, Personal Communication, CEA Saclay, F-91191 Gif-sur-Yvette, France

[20] G. Graziani, Linearity of the response to test beam electrons for EM Barrel module P13, ATL-LARG-2004-001, 2004

[21] M. Delmastro, Energy reconstruction and calibration algorithms for the ATLAS electromagentic calorimeter, PhD-Thesis at the University of Milano, 2002

[22] F. Hubaut, Crosstalk measurements summary in EMB Module 13, LAr internal note, 2001

[23] S. Paganis, Atlas and CTB04 X_0 maps, http://www-wisconsin.cern.ch/~paganis/atlas/X0map/X0map.html

[24] The ATLAS Liquid Argon Collaboration, Linearity and Resolution of a ATLAS Electromegnetic Barrel Calorimeter Module in the CERN Electron Test-beam, in prepration, 2005

[25] M. Gallas, ATLAS CTB04 simulation web-page, http://atlas.web.cern.ch/Atlas/GROUPS/SOFTWARE/OO/simulation/geant4/CTB_G4Sim/doc/CTB.html

Curriculum Vitae

I was born June 2nd, 1975, in Vienna, Austria. My parents are Dr. Horst Lampl and Dr. Edith Lampl, both employed at the Institute of Slavic Languages at the University of Vienna. In 1976 my family moved to Korneuburg, a small town in Lower Austria. In Korneuburg I attended the Primary School (1981-1985) and the Secondary Modern School (1985-1989). From 1989 to 1994 I attended the "HTL-Wien XX, Technologisches Gewerbemuseum", department for communication engineering. This is a special type of school, where secondary school is combined with technical education. During this time, I also completed two traineeships, the first in summer 1991 at a small electrical workshop in Korneuburg, the second in summer 1992 at Alcatel Austria in Vienna. In June 1994 I passed the Austrian school leaving exam with honor.

In October 1994 I began my studies in Technical Physics at the Vienna University of Technology. From February 1995 until December 1995 I interrupted my study to complete the "alternative service" (alternative to the military service) as an ambulance driver and first aid attendant at the Red Cross station in Korneuburg. In January 1996 I resumed my studies. In May 1999 I finished the first part of my studies. During my university education I worked on three scientific projects, the first in the field of ultrasonic measurements, the second in the CERN ATM group and the third in the field of reactor safety.

From July 2001 until July 2002 I worked on my diploma thesis in the CERN ATM group. My task was the automation of the "Atlas Muon X-Ray Tomograph", used for quality control for the precision chambers used in the Atlas muon sprectrometer. In October 2002 I passed the diploma examination in Technical Physics at the Vienna University of Technology. From December 2002 until February 2003, I continued working in the CERN ATM group.

In autumn 2002 I was accepted as a Student in the CERN Austrian Doctoral Student Program. I started working on my PhD thesis in March 2003 in the CERN ATA Group on the Electromagnetic Calorimeter of the Atlas Experiment. In 2004, I participated in preparing and operating the calorimeter part of the Atlas combined beam test.